Interaction of locomotion and intraspinal lumbosacral organ in birds

Dissertation
der Mathematisch-Naturwissenschaftlichen Fakultät
der Eberhard Karls Universität Tübingen
zur Erlangung des Grades eines
Doktors der Naturwissenschaften

(Dr. rer. nat.)

vorgelegt von

M.Sc. Viktoriia Kamska
aus Odessa/Ukraine

Tübingen
2022

Gedruckt mit Genehmigung der Mathematisch-Naturwissenschaftlichen Fakultät der Eberhard Karls Universität Tübingen

Tag der mündlichen Qualifikation:	24.02.2023
Dekan:	Prof. Dr. Thilo Stehle
1. Berichterstatter:	Dr. Alexander Badri-Spröwitz
2. Berichterstatter:	Prof. Dr. Jan Benda
3. Berichterstatter:	Prof. Dr. Hanspeter Mallot

Abstract

Avian ability to agile and precise locomotion in every livable habitat has fascinated researchers for over a century. One explanation for birds' agility is a mechanosensory organ directly integrated into the lower spine in the lumbosacral region. The proximity of the potential mechanosensory organ to the sciatic nerve and its associated motor circuits could explain how birds circumvent the limits of nerve conduction velocity associated with proprioception by shortening neural circuits, thereby contributing to the agility of avian locomotion. Avian lumbosacral region's specializations are unique among vertebrates. The lumbosacral region, recently referred to as the lumbosacral organ (LSO), consists of a high-density glycogen body wedged between the spinal cord hemispheres, supported by a pronounced network of denticulate ligaments. From the lateral sides of the spinal cord, accessory lobes with potential mechanosensory function protrude into a fluid-filled expanded spinal canal with transverse semicircular grooves on the dorsal side. Although the LSO specializations were discovered more than a century ago, their functional features remain unknown. The topographic anatomy of the accessory lobes suggests two excitation mechanisms that are not necessarily mutually exclusive. Firstly, the intimal connection of the accessory lobes to the denticulate ligament network supporting the spinal cord offers a strain-based mechanism of accessory lobe excitation. Secondly, the accessory lobes' alignment with the opening of transverse grooves, which resemble the semicircular canals of the mammalian inner ear, indicates that the excitation mechanism could be associated with a fluid flow.

In this thesis, by applying modern techniques to earlier hypotheses about the LSO's perception of fluid flow, pressure, and strain - we developed a new mechanosensing hypothesis, which in contrast to previous theories, considers the interaction of the lumbosacral specializations. 3D morphometric analysis of data produced by digital dissection allows us to evaluate the fluid space around the neural soft tissue. Additionally, classical dissection shows fine details of the hammock-like network of denticulate ligaments not visible in our 3D map. We estimate potential soft tissue displacement and deformation capacity inside the enlarged and fluid-filled lumbosacral spinal canal by combining the digital and classical dissection results. Establishing morphological and biomechanical properties allows us to hypothesize a sensing mechanism based on lumbosacral soft tissue oscillation caused by external acceleration, with a motion similar to a fluid-filled spring-mass-damper system. Potentially the mechanosensitive accessory lobes encode signals about the internal state of the neural soft tissue, entrained by external physical forces. Hence, the LSO may sense acceleration forces independently from the vestibular apparatus localized in the head. A relatively dense glycogen body potentially loads the viscoelastic spinal cord,

causing it to deform. However, no study has tested whether the soft tissues inside the lumbosacral canal of birds are movable. The state-of-the-art techniques show limits in identifying soft tissue movements *in vivo* inside highly pneumatized bones of a fused synsacrum covered with multilayered soft tissue. Therefore, we combined *in situ* digital dissection and biophysical simulation. 3D scanning of cadaver LSO samples in different orientations enabled us to reveal that the LSO soft tissues exhibit minor position displacement in a static state. Our modification of the traditional diceCT protocol allowed us to visualize previously undocumented details on the denticulate ligament topology, which potentially affects soft tissue mobility. Inspired by LSO morphometrics, we developed a reconfigurable biophysical LSO model to study the impact of individual lumbosacral anatomical structures. The biophysical simulation confirmed our assumption that the denticulate ligament network and the magnitude of acceleration affect soft tissue mobility. By altering the LSO model parameters, we also revealed the fluid dynamics effects of the lumbosacral spinal canal morphology on the soft tissues' time and frequency response. Our hypothesis that the LSO resembles a spring-damper system is supported by the glycogen body model acting as a mechanical amplifier for spinal cord oscillations.

Zusammenfassung

Die Fähigkeit von Vögeln sich wendig und präzise in jedem bewohnbaren Lebensraum fortzubewegen, fasziniert Forscher seit über einem Jahrhundert. Es wird vermutet, dass die Beweglichkeit der Vögel durch ein mechanosensorisches Organ ermöglicht wird, welches direkt in die untere Wirbelsäule, im sog. Lumbosakralbereich, integriert ist. Diese Spezialisierung der Vögel im Lumbosakralbereich ist dabei einzigartig unter den Wirbeltieren. Obwohl die morphologischen Spezialisierungen bereits vor mehr als einem Jahrhundert entdeckt wurden, sind ihre funktionellen Merkmale nach wie vor unbekannt. Die unmittelbare Nähe dieses mechanosensorischen Organs zum Ischiasnerv und den damit verbundenen motorischen Schaltkreisen könnte erklären, wie Vögel die Grenzen der Nervenleitgeschwindigkeit umgehen, die neuronalen Schaltkreise verkürzen und so die Agilität und Tiefensensibilität (Propriozeption) auch bei hohen Geschwindigkeiten ermöglichen. Die lumbosakrale Region bzw. das "lumbosakrale Organ" (LSO) besteht aus einem sehr dichten Glykogenkörper, der zwischen den Ruckenmarkshälften eingekeilt ist und von einem Geflecht aus zahnförmigen Bändern gestützt wird. Aus den lateralen Seiten des Ruckenmarks ragen akzessorische Lappen in einen mit Flüssigkeit gefüllten, erweiterten Ruckenmarkskanal mit halbkreisförmigen, querverlaufenden Rillen auf der Dorsalseite. Diese akzessorischen Lappen könnten möglicherweise eine mechanosensorischer Funktion aufweisen. Die topographische Analyse der Anatomie dieser Lappen lässt auf zwei Anregungsmechanismen schließen, welche sich nicht zwangsläufig gegenseitig ausschließen. Zum einen könnte die enge Verbindung der akzessorischen Lappen mit dem das Rückenmark stützenden *Ligamentum denticulare*, einen dehnungsbasierten Mechanismus darstellen. Zum anderen deutet die Ausrichtung der Lappen hin zu den öffnungen der querliegenden Rillen, welche den Bogengängen eines Säugetierinnenohrs ähneln, auf einen Mechanismus hin, welcher über die Bewegung der Flüssigkeit induziert wird.

In dieser Arbeit wurden existierende Hypothesen zur Funktionsweise des LSO und dessen Wahrnehmung von Strömungen, Druck oder Dehnung durch die Anwendung moderner Techniken erweitert. Im Gegensatz zu früheren Theorien wurden hier die Interaktion der lumbosakralen Spezialisierungen berücksichtigt. Die morphometrische 3D-Analyse von Daten, die per digitaler Dissektion erzeugt wurden, ermöglichen es den Flussigkeitsraum um das neurale Weichgewebe zu analysieren. Zusätzlich zeigt die klassische Dissektion zeigt feine Details des hängemattenartigen Netzwerks der dentikulären Bänder, die in unserer 3D-Karte nicht sichtbar sind. Durch die Kombination der Ergebnisse der digitalen und der klassischen Dissektion können wir die Verschiebung- und Verformungskapazität des Weichgewebes im vergrößerten und mit Flüssigkeit gefüllten

lumbosakralen Wirbelsäulenkanal abschätzen. Die Ermittlung der morpholo-
gischen und biomechanischen Eigenschaften erlaubt uns die Hypothese eines
sensorischen Mechanismus aufzustellen, der auf der Oszillation des lumbosakralen
Weichgewebes durch externe Beschleunigung beruht und dessen Bewegung einem
flussigkeitsgefullten Feder-Masse-Dämpfer-System ähnelt. Möglicherweise kön-
nten Auslenkungen des neuralen Weichgewebes durch äußere physikalische Kräfte,
über die mechanosensiblen, akzessorischen Lappen erfasst werden. Auf diese
Weise könnte der LSO Beschleunigungskräfte unabhängig von dem im Kopf
lokalisierten vestibulären Apparat wahrnehmen. Eventuell wird das viskoe-
lastische Rückenmark durch den dichten Glykogenkörper belastet und dadurch
verformt. Allerdings wurde bisher in keiner Studie untersucht, ob die Weichteile
im Lumbosakralkanal von Vögeln beweglich sind. Die Identifizierung der We-
ichteilbewegungen *in vivo* innerhalb der stark pneumatisierten Knochen des
fusionierten Synsakrums, die ebenfalls mit mehrschichtigem Weichgewebe be-
deckt sind, ist mit den derzeit verfügbaren Techniken nur sehr schwierig zu
analysieren. Aus diesem Grund haben wir eine Kombination aus digitaler *in
situ* Dissektion und biophysikalischer Simulation zur Analyse herangezogen.
Durch 3D-Scans von Kadaver-LSO-Proben in verschiedenen Orientierungen
konnten wir zeigen, dass die LSO-Weichgewebe im statischen Zustand eine
geringe Positionsverschiebung aufweisen. Durch eine Abwandlung des tradi-
tionellen diceCT (Iod-kontrastverstärkende Computertomographie)-Protokolls
konnten wir außerdem weitere Details der Topologie der *Ligamenta denticularis*
sichtbar machen, welche sich auf die Mobilität des Weichgewebes auswirken
könnten. Inspiriert von der LSO-Morphometrie entwickelten wir so ein kon-
figurierbares, biophysikalisches LSO-Modell, um die Auswirkungen einzelner
Strukturen zu untersuchen. Die biophysikalische Simulation bestätigte unsere
Annahme, dass das Netzwerk der dentikulären Bänder, sowie das Ausmaß der
Beschleunigung, die Beweglichkeit der Weichteile beeinflussen. Durch Verän-
derung der Parameter des LSO-Modells konnten wir zeigen, dass fluiddynamische
Effekte des lumbosakralen Wirbelkanals ebenfalls einen Einfluss auf die Zeit-
und Frequenzantwort der Weichteile haben. Unsere Hypothese, dass das LSO
einem Feder-Dämpfer-System ähnelt, wird durch das Glykogenkörper-Modell
gestützt, welches als mechanischer Verstärker für Ruckenmarksschwingungen
fungiert.

Acknowledgements

"When I want to read a novel, I write one." - Benjamin Disraeli

Contents

List of Figures

xvi

List of Tables

List of Abbreviations

Abbreviation	Name
a.isc.	ala ischii
a.p.i.	ala postacetabularis ilii
a.pr.i.	ala preacetabularis ilii
ac.l.	accessory lobe
an.	antitrochanter
b.	bone
bif.t.p.	bifurcated transverse processes
c.i.d.	crista iliaca dorsalis
c.o.m.	center of mass
c.s.c.	cross-section through the spinal canal
c.s.s.	crista spinosa synsacri
ep.	ependyma
ex.c.sy.	extremitas cranialis synsacri
f.ac.	foramen acetabuli
f.h.	femural head
f.n.sp.	fused neural spines
f.s.n.	foramina spinal nerve
fl.s.	fluid space
g.b.	glycogen body
gr.	groove
h.	hole
i.	ilium
is.	ischium
lam.	lamina
l.l.l.	lateral longitudinal ligament
l.p.	lateral process
m.d.l	medial denticulate ligaments
p.	pubis
pe.	pedicle
p.il.	postacetabular ilium
p.m.	pia mater
pr.tr.s.	processus transversus sacralis
pre.il.	preacetabular ilium
r.s.r.	rootlets of sensory root
s.an.	sulcus antitrochantericus
s.i.	sync. ilioischiadica
s.p.	sciatic plexus
s.r.	sensory root

s.r.g.	sensory root ganglion
s.v.sy.	sulcusvent. synsacri
sp.c.	spinal cord
v.b.	vertebral body
v.l.l.	ventral longitudinal ligament
v.p.	ventral process
v.t.l.	ventral transverse ligament

*Dedicated to the most important people in my life -
my parents!*

Chapter 1

Introduction

Birds belong to a diverse class of vertebrates showing shared exceptional ability to finesse locomotion in various habitats (Daley, 2018). The mechanism that controls precise movements in birds remains unclear. But recently, it has been suggested that avians possess an additional intraspinal mechanosensing organ in the lumbosacral region at the lower spinal cord. The structures are referred to as the lumbosacral organ (LSO), possibly contributing to birds' locomotor agility and evolutionary success (Necker, 1999, 2005, 2006). While interest in a potential LSO mechanosensing functionality has long arisen, nevertheless, the mechanism remains unclear. There currently exist fluid-flow and strain-based mechanosensing hypotheses that possibly do not mutually exclude each other. One of the most prevailing hypotheses relevant to a fluid-flow excitation mechanism was suggested by Necker, 1999 that the LSO is the second center of equilibrium that acts similarly to the vestibular organ of the inner ear. We suggested an alternative hypothesis on a strain-based mechanosensing mechanism suggested by Schroeder and Murray, 1987. So far, only a few cases of strain-based intraspinal mechanosensing systems have been discovered in vertebrates: a lamprey (Grillner, Williams, et al., 1984) and a zebrafish (Picton et al., 2021). Nevertheless, these rare examples can shed some light on the possible intraspinal mechanosensing mechanism for the LSO.

The thesis focuses on a putative intraspinal mechanosensitive lumbosacral organ potentially contributing to birds' agile and robust locomotion. We hypothesize that the nerve soft tissue inside the lumbosacral spinal canal oscillates in response to acceleration caused by birds' locomotion, which indicates the LSO similarity to a mass-spring-damper accelerometer. The currently available imaging technologies are limited and cannot directly visualize the behavior of nerve soft tissue within a synsacrum formed by the fusion of pelvic and highly pneumatized spines. In addition, the synsacrum is covered with the multi-layered soft tissue of varying density. Therefore, the methodology combines classical and digital dissections with a biophysical simulation approach to study the impact of LSO morphological features on the system response shaping. I worked in collaboration on three individual projects to accomplish the thesis objectives. Each project is presented as a separate chapter.

In Chapter 2, I introduce the lumbosacral organ as an additional potential mechanosensory organ in an avian trunk uncoupled from the vestibular inner ear organ in the head. The unique avian lumbosacral morphology of the anatomical features suggests their interaction results in intraspinal mechanosensation. Direct

integration into the lower part of the spinal canal and its proximity to the hind legs indicates the LSO informs the central nervous system about unpredictably changed terrain and coordinates limbs with minimal neural delay. Morphological features of the lumbosacral spine are introduced, accompanied by information on already established physiological properties and functional hypotheses.

In Chapter 3 I present the first project focused on the 3D anatomy of the lumbosacral spinal canal in quail. The project aimed to quantify the geometric and biomechanical properties of the lower spine anatomical structures relevant to the hypothesis on the mechanosensing function of the LSO. We hypothesize that the anatomical structures' unique morphology collectively results in them acting as a mass-spring-based accelerometer. To quantify the morphological parameters of the LSO anatomical structures, we combined classical dissection using a stereomicroscope and digital dissection based on contrast-enhanced μCT data.

The second project described in Chapter 4 focused on studying the soft tissue's capacity to motion inside the lumbosacral canal. We altered the applied gravity orientation to the dissected lumbosacral sample at its static state and extracted data by approaching a digital dissection. The qualitative biophysical LSO model allowed us to test our hypothesis on the influence of the anatomic interactions on soft tissue mobility at static and dynamic states.

The third project described in Chapter 5 aimed to study the lumbosacral soft tissue response to external movements and accelerations by approaching the biophysical stimulation. With a configurable modular biophysical model inspired by the 3D morphometrics of the avian LSO, we tested the impact of each relevant anatomical structure individually on the soft tissue response to the external oscillations.

Motivation and Objectives

- Creating a 3D map of anatomical specializations inside the lumbosacral region in birds.

- Quantifying the geometric and biomechanical properties of the lumbosacral region relevant to its potential mechanosensing function.

- Quantifying whether the neural soft tissues deflect at a quasi-static and dynamic state of the expanded lumbosacral canal under interacting and counteracting physical forces produced by unique lumbosacral anatomic specializations.

- Establishing a function for each anatomical structure, exhibiting the LSO as a mechanosensitive organ acting similarly to a mass-spring-damper system.

Contributions

I developed the main concept of the thesis project under the supervision of Dr. Alexander Badri-Spröwitz. I have reviewed the literature related to avian anatomy, neurobiology, neuromechanics, and physiology, focusing on the avian lumbosacral region. Also, the literature concerns the broad spectrum of hypotheses on the functional relevance of avian lumbosacral spine anatomical features, both individually and in combination.

The first project described in Chapter 3 I formulated, implemented, and published (Kamska, Daley, et al., 2020) under the mentorship of Dr. Alexander Badri-Spröwitz and Prof. Dr. Monica Daley.

- Based on classical and digital dissection data, I conducted a morphometric analysis of the lumbosacral organ's components.

- For the digital-based morphometry, using 3D segmentation, I created a new 3D map of the bone, soft and connective tissue constituting the lumbosacral organ housed inside the synsacrum of a common quail (*Coturnix coturnix*). The quail sample was processed and μCT scanned by Dr. Michael Doube of the Royal Veterinary College of London.

- I have developed a new 3D segmentation approach for poorly visible fine structures to accurately segment the denticulate ligament network as a separate 3D model and align it with the entire LSO 3D models at the final step.

- I have evaluated a denticulate ligament network topology approaching a classical dissection of the quail cadaver under the assistance of Dr. Karin Elflein.

- By combining the data I have extracted using the digital and the classical dissection of quail specimens - I evaluated the potential for a maximum extension of the denticulate ligaments under the hypothesized soft-tissue deformation.

The second project described in Chapter 4 I formulated, implemented, and prepared for the publication submission under the supervision of Dr. Alexander Badri-Spröwitz. The project aimed to evaluate the soft tissue capacity to deflect inside a lumbosacral canal. The limitation in visualization technology forced us to look for alternative approaches. In collaboration, I worked on developing methods for assessing the soft tissue capacity to deflect inside a lumbosacral canal. In this project, we use a combination of an in situ and a biomechanical simulation.

- With Dr. Rolf Pohmann of the Max Planck Institute for Biological Cybernetics, we modified a protocol for imaging small animals using MRI. We visualized fine structures without chemical treatment through

preliminary tests, a prompt dissection of the fresh domestic chicken cadaver by me, and an MRI by Dr. Pohmann.

- Together with Dr. Karin Elflein, I chose a fixative solution that causes less of a shrinking effect on the neural soft tissues by testing the speed and intensity of the soft tissue response.

- I modified the traditional diceCT sample processing technique by opening an additional inlet and gentle manual infusing chemicals inside the spinal canal. I used micro-surgical instruments for fine dissection to open the inlet for the fixative and staining solution to the soft tissues housed inside the spinal canal.

- With Dr. Alexandros Karakostis and his assistant Alessio Maiello we conducted several experimental micro-CT scans of the iodine-stained sample of the lumbosacral region of a chicken. As a result, we developed a successful diceCT scanning protocol.

- I developed an approach of semi-automatic segmentation in 3D of the soft and solid tissue that minimizes deviations in size and shape of the same sample scanned in different orientations.

- I developed approaches for measuring the soft tissue deflection and evaluating the errors caused by the scanning, 3D segmentation, and the final step of the 3D models' alignment.

- An Mo helped me with the final run of the iterative closest point (ICP) algorithm to align the 3D models of the sample scanned in its different orientations.

- I created 3D maps of anatomical structures housed inside chicken lumbosacral samples based on data produced with different imaging protocols.

- In collaboration with An Mo, I modified the LSO biophysical model by fabricating the denticulate ligament network to test their effect on soft tissue mobility.

- In collaboration with An Mo, we tested the LSO biophysical model response on static and dynamic acceleration. At the analysis step, I evaluated data on the model response to the static acceleration.

The third project described in Chapter 5 I conducted as the second author where we applied mechanical simulation to test our hypotheses about the function of individual anatomical features of the LSO. The project was formulated, implemented, and prepared for publication submission under the supervision of Dr. Alexander Badri-Spröwitz.

- In collaboration with An Mo, I equally contributed to the simplification of the morphometric parameters of the quail lumbosacral region I extracted in the first project described in Chapter 3.

- In collaboration with An Mo, I equally contributed to developing hypotheses for each anatomical structure we assume impacts the LSO response under external acceleration.

- In collaboration with An Mo, I have contributed to developing a reconfigurable design for the modular LSO biophysical model to test our hypotheses.

- In collaboration with An Mo, I have equally contributed to evaluation materials and methods for the qualitative replication of the LSO soft and connective tissue.

- At the step of data analysis, which centrally was conducted by An Mo and Dr. Fernanda Bribiesca-Contrera, I contributed to the results interpretation step.

Chapter 2

Background

2.1 Diversity of Avian Locomotion Modes

Birds are one of the most diverse groups of vertebrates in the modern world, with around 10,000 extant species habitat in almost every environment on earth (Abourachid and Höfling, 2012; Brusatte et al., 2015) and capable with exceptional agility of aerial, terrestrial, aquatic, and arboreal locomotion (Daley, 2018). Birds are characterized by three distinct locomotor modules: forelimbs, hindlimbs, and tail (Dial, 2003; Gatesy and Dial, 1996). The mechanical properties of hindlimbs provide birds with a multi-purpose tool engaged in walking, running, hopping, flying, and swimming (Abourachid and Höfling, 2012). Locomotor adaptation to habitat is facilitated by body size and mass varying from ∼2 grams (hummingbirds) (Brusatte et al., 2015) to 150 kg (ostrich) (Abourachid and Höfling, 2012), bone density, limbs length, neck, and trunk posture (Abourachid and Höfling, 2012; Dumont, 2010; Gatesy and Middleton, 1997; Heers and Dial, 2015; Zeffer et al., 2003). However, despite variations in the size and proportions of the trunk and limbs, as well as the morphological specialization of the locomotor apparatus (Gatesy and Middleton, 1997; Heers and Dial, 2015), the birds share approximately the same body design (Abourachid and Höfling, 2012). That can indicate that body morphology and proportion variations are not the only reason birds achieve locomotor agility (Kamska, Daley, et al., 2020).

2.2 Sensorimotor Factor in Agile Locomotion

The ability of birds to respond to substrate changes during locomotion is supported by sensorimotor control (Daley, 2018; More, O'Connor, et al., 2013). Sensorimotor delays constrain the accuracy and responsiveness of the sensorimotor system (Churan et al., 2017; Daley, 2018; More and Donelan, 2018; More, O'Connor, et al., 2013). The transmission efficiency of sensory input and motor commands are linked to the source, distance, and speed at which the information travels through different sensorimotor pathways (Abraira and Ginty, 2013; Dusenbery, 1992; Martin, 2012). One of the primary keys to the fast reaction speed that leads to the immediate recovery after the unexpected perturbation is minimal signal transmission delay (Daley, 2018; Daley, Usherwood, et al., 2006) (see Figure 2.1). The time required for the potential action transmission with minimal conduction delay becomes more acute as the sensory and motor nerve
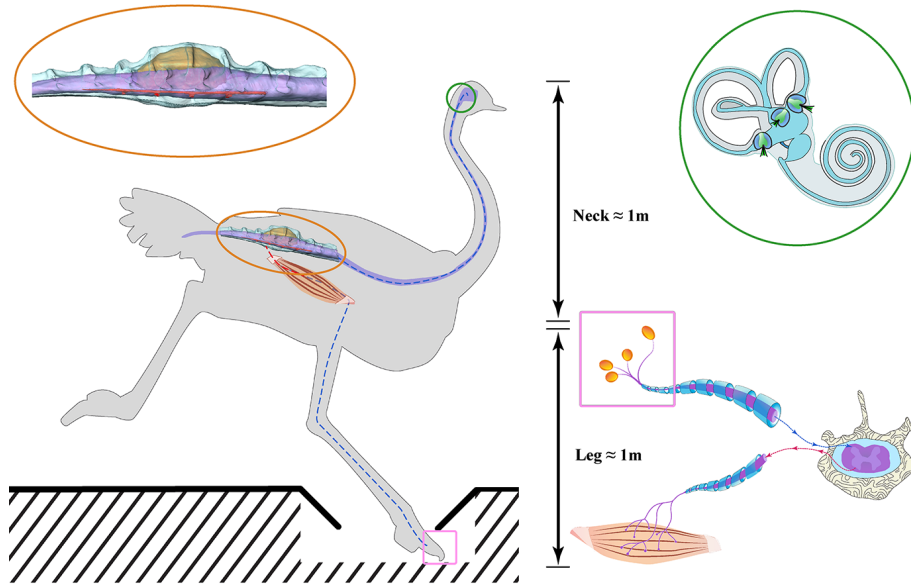
Figure 2.1: Sensorimotor delays of different categories of sensory inputs.
The length of the sensorimotor pathways from the potential sensor to the hind limb muscles affects the nerve conduction delay. The example of the largest bird of our time schematically shows the moment that follows the unexpected perturbation experienced by an ostrich running through terrain with a changing surface. The orange ellipse highlights the putative intraspinal mechanosensing lumbosacral organ (LSO); the green circle indicates the peripheral vestibular organ begins in the inner ear; the pink square shows the peripheral cutaneous end-organ sensitive to the ground impact that begins from the sensory corpuscles in toes. The blue dash line illustrates the sensor signal path that starts from peripheral sensors to the central neural system (CNS); the red dash line is the motor signal path from the CNS to the muscles. Inner ear was modified from Obrist et al., 2010, ostrich outline was modified from Chan DMD, 2007

fibers' length increases (More and Donelan, 2018; More, O'Connor, et al., 2013). The anatomical specializations in the lumbosacral region, collectively known as the lumbosacral organ (LSO), hypothetically contribute to bird's locomotion agility (Giffin, 1990; Kamska, Daley, et al., 2020; Necker, 1999; Stanchak, French, et al., 2020). Its unique morphology, direct integration into the central neural system in the lower part of the spine, and proximity to the hindlimbs indicate the LSO potentially acts as an intraspinal mechanosensing organ, independent of the vestibular organ (Kamska, Daley, et al., 2020; Necker, 1999, 2006; Stanchak, French, et al., 2020; Urbina-Meléndez et al., 2018). The LSO is intimately close to the lumbosacral plexus that communicate motor commands for locomotion (Bekoff et al., 1975). This plexus innervates the skin and muscles of the lower limb through the sciatic nerves and the thigh muscles through the crural nerves (Bentley and Poole, 2009; Giuffre and Jeanmonod, 2020; Haimson et al., 2021; Kardon, 1998; Lance-Jones and Landmesser, 1981). The advantage of the LSO comes from reducing input and output pathways, contributing to a faster sensorimotor response by minimizing the signal transmission delays (Côté et al., 2018). Direct integration with the pelvic-localized spinal motor circuits and proximity to the feet provides the LSO a functional advantage over the head-localized
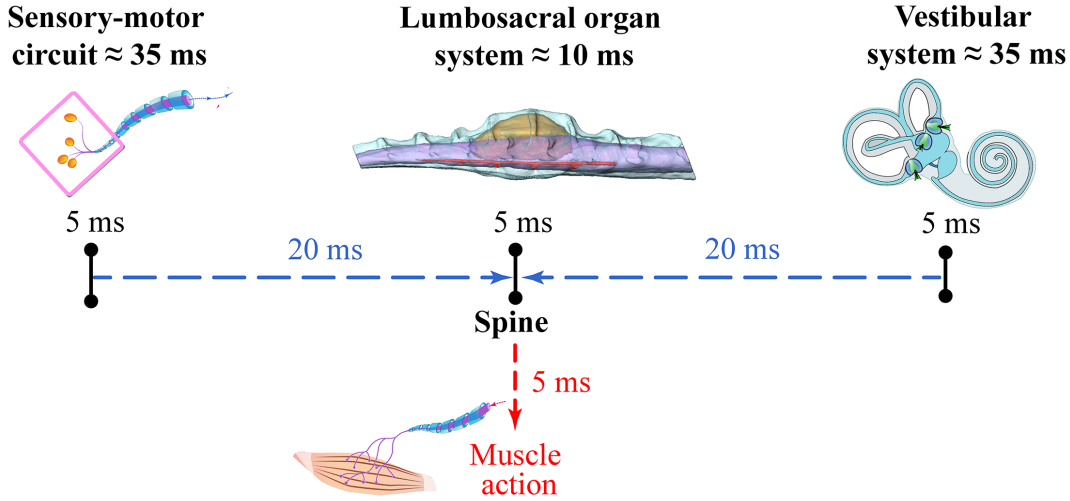
Figure 2.2: Efficiency evaluation of sensory input by sensory-motor delays.
Simplified estimation (see Equation (2.1)) of the sensorimotor pathways shows the dependency of the neural signal transmission delay on the distance between the considered sensory inputs and the actuated legged muscles. The blue dash line illustrates the sensor signal path from the peripheral sensors to the central nervous system (CNS). The leg length ($\approx 1\,\mathrm{m}$) corresponds to the sensor path of the sensory-motor circuit, and the neck length ($\approx 1\,\mathrm{m}$) to the path for the vestibular system. The red dash line is the motor signal path from the CNS to the muscles. The inner ear was modified from Obrist et al., 2010

.

vestibular sensory organs (Urbina-Meléndez et al., 2018) and sensory-motor circuit or a monosynaptic reflex arc (More, O'Connor, et al., 2013) to which input starts from cutaneous end-organs at the tips of hindlimb toes (Suazo et al., 2022; Zimmerman et al., 2014). Therefore, it provides an evolutionary advantage for birds. Ostrich is a vivid example demonstrating how the neural signal transmission delay depends on the path length the sensory-motor signal travel. To quantify the advantage of the potential intraspinal mechanosensory lumbosacral organ over the peripheral sensory-motor circuit (H. H. Chen et al., 2003) and vestibular organ (T. L. Thompson and Amedee, 2009), we conducted simplified calculations (see Equation (2.1)) of the neural signal transmission delay based on the distance between the considering sensory inputs and the actuated hind limb muscles (see Figure 2.2). The approximate value of the nerve conduction velocity ($50\,\mathrm{m/s}$) we took from (Stetson et al., 1992; Whalen et al., 1988). For simplification of calculations, the time for the signal generation is identical for all comparing sensory organs ($5\,\mathrm{ms}$). Determination of the approximate length of the nerve paths distance from the vestibular organ and sensory-motor circuit to the lower part of the spine was based on the length of the neck ($\approx 1\,\mathrm{m}$) and the length of the leg ($\approx 1\,\mathrm{m}$), respectively (see Figure 2.1). In contrast, the intraspinal mechanosensor LSO is directly integrated into the lower part of the spine.

$$\left\{ \mathrm{NCD} = \mathrm{SSG} + \mathrm{SR} + \mathrm{Sp} + \mathrm{MR} \right. \tag{2.1}$$

the NCD is a nerve conduction delay, SSG is a time for the signal generated by a sensor, SR is a sensor root through which the signal travels from the sensory input to the CNS, Sp is the time for converting sensory signals to motor signals in a spine, MR is a motor root through which the signal travels from the CNS to the actuated legged muscles. Simplified calculations and comparative analysis demonstrate the effectiveness of the putative intraspinal lumbosacral mechanosensory organ, which costs the ostrich about 10 ms of the delay over the peripheral vestibular and cutaneous end-organs cost about 35 ms of the delay each (see Figure 2.2). Considering that range of an ostrich's running speeds varies around 11 m/s to 17 m/s (Alexander et al., 1979; Daley, Channon, et al., 2016), the nerve fiber distances between the peripheral sensor system inputs are too long to provide prompt sensorimotor signals for efficient control of the body position during the legged locomotion (Abourachid, Hackert, et al., 2011; More, O'Connor, et al., 2013; Stetson et al., 1992; Urbina-Meléndez et al., 2018; Wedel, 2011).
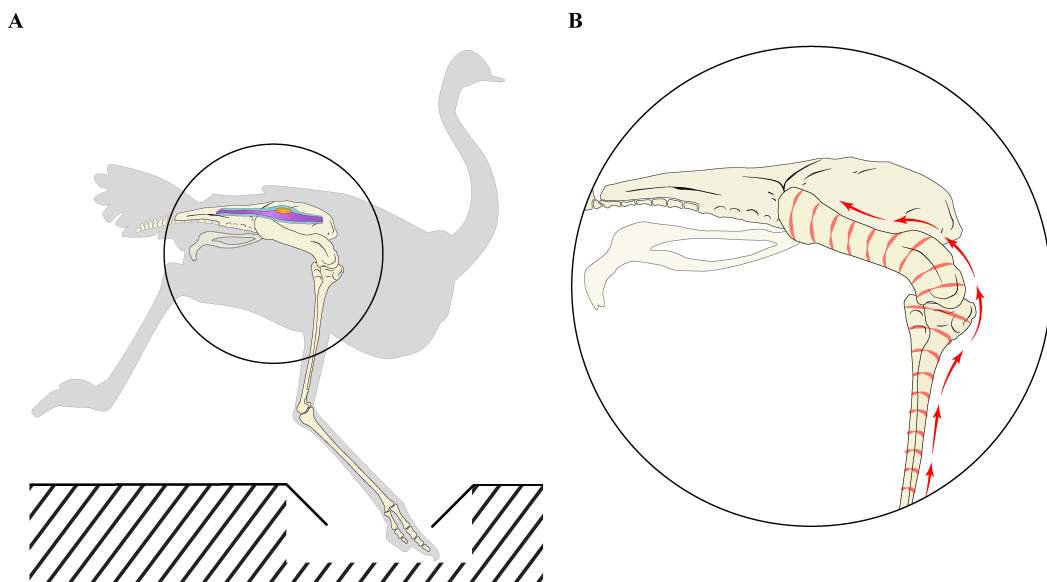
Figure 2.3: LSO stimulation through mechanical shock wave propagation.
(A) The schematic illustration shows the moment immediately after the ostriches' foot broke through the tissue paper, masking the difference in substrate height. As a result of the unexpected disturbance, it hit the ground with its toe. (B) The mechanical shock caused waves to propagate directly through the bone tissue of the hind limb to the synsacrum housing the LSO. Ostrich outline was modified from Chan DMD, 2007, skeleton was modified from (Coutureau, 2014)

The lumbosacral organ sensory perception mechanism is currently not fully understood. We assume that bone's capacity to convert external mechanical stimuli into biochemical reactions (Stewart et al., 2020) may contribute to a hypothetical proprioceptive system. The speed at which sound waves propagate through hindlimbs depends on the density of constituent tissue (Otani, 2005) and varies from 400 m/s to 1500 m/s (Dobrev et al., 2017; Kaczmarek et al., 2002; Otani and Hosokawa, 1998). For comparison, the speed of the nerve-tissue-based information travel varies around 30 m/s to 65 m/s for bird-sized animals (More

and Donelan, 2018; More, Hutchinson, et al., 2010; Whalen et al., 1988). This simplified comparison shows that the mechanical shock wave signal speed is about 6 to 50 times faster than the speed of nerve impulses. Therefore, we can also assume that the intraspinal mechanosensory system minimizes sensorimotor delay by spreading the signal with sound waves initiated by the toe striking the ground during locomotor movements, passing through the hindlimb bones directly into the synsacrum (see Figure 2.3).

2.3 Unique Anatomy of the Lumbosacral Region
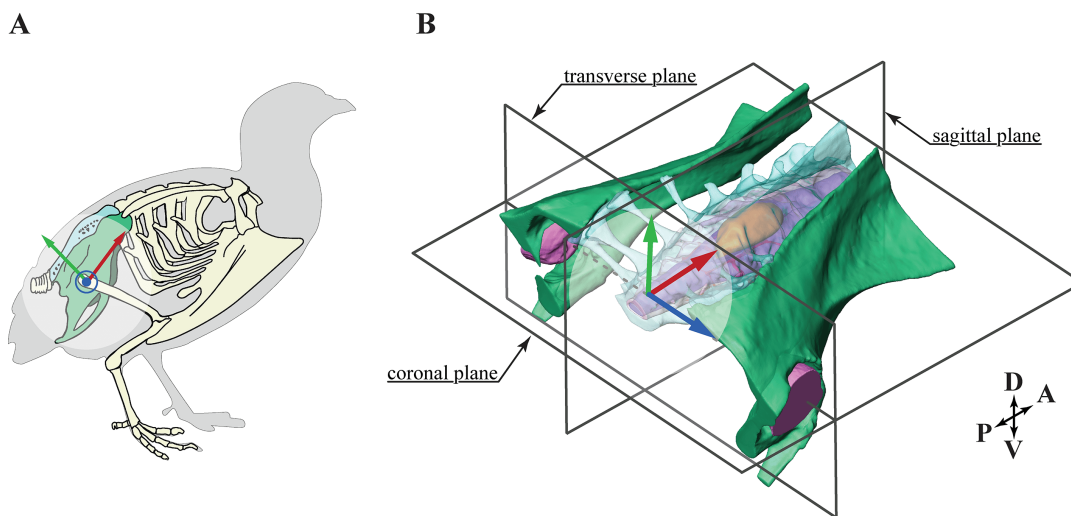
Figure 2.4: The anatomy of the synsacrum of the quail (modified from Kamska, Daley, et al., 2020). (A) Schematic skeletal outline of a quail synsacrum, emphasized in green and turquoise. The schematic was modified from (Commons, 2009). (B) A 3D view of the synsacrum, also showing a local coordinate system (x-red, y-green, z-blue), and three planes of reference. The coordinate origin is centered between the left and right acetabular sockets surrounding the femoral heads, and the coronal plane is adjusted to the segmental narrow regions of the lumbosacral canal formed at the vertebral fusion, which serve as attachment sites for the dentate ligaments network.

Avian lumbosacral spinal canal exhibits unique enlargement compared to other vertebrates (Badawi et al., 1994; Giffin, 1990, 1995; Haziroglu et al., 2001). In many tetrapods, the lower part of a spine enlargement is caused by a plexus increase to innervate hindlimbs (Giffin, 1990, 1995). Birds demonstrate that the fluid space in the extended lumbosacral spinal canal exceeds the volume occupied by the neural soft tissue (Giffin, 1990). The enlargement of the spinal canal in the lumbosacral region is housed within the synsacrum (see Figure 2.4), the holistic structure formed by the fusion of lumbar and sacral vertebrae and a pelvic girdle (J. J. Baumel, 1993; Giffin, 1990). The soft tissue (see Figure 2.5) includes the spinal cord and glycogen body supported and stabilized (J. Baumel, 1985; Polak-Kraśna et al., 2019; Ranger et al., 2008) within the enclosed and extended spinal canal by the connective tissue consisting of the cerebrospinal fluid (CSF) and the denticulate ligaments (Necker, 2005, 2006; Rosenberg and Necker, 2002; Schroeder and Murray, 1987; Streeter, 1904; Urbina-Meléndez

et al., 2018; Yamanaka, Kitamura, and Shibuya, 2008).   The glycogen body is
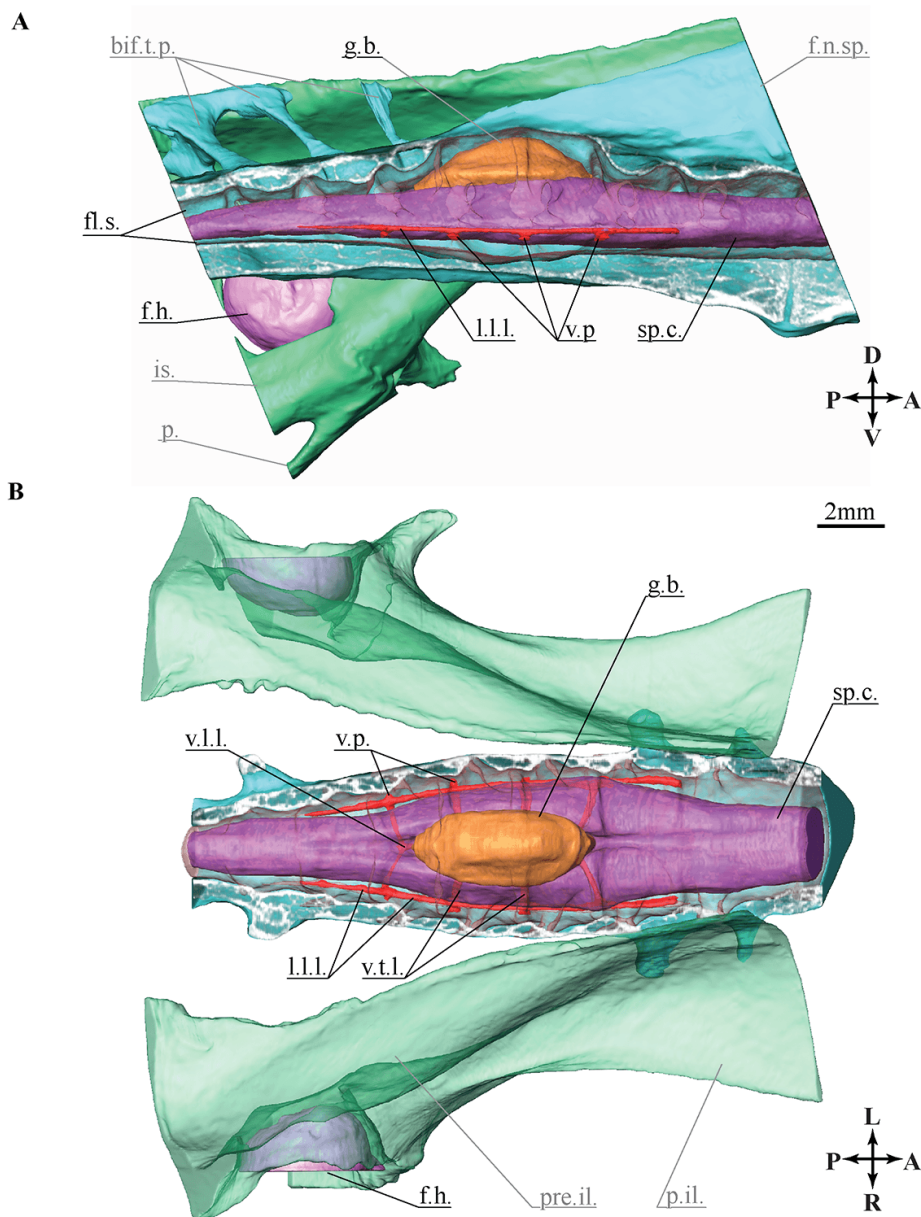
Figure 2.5: 3D anatomy of the lumbosacral region of the common quail
(from Kamska, Daley, et al., 2020). 3D model created with digital dissection on μCT
data showing: (A) right lateral view at the sagittal section of the lumbosacral spinal
canal; (B) coronal view at the spinal canal truncated at half height, soft tissues are
not cut. See abbreviations in Table 1.

settled in between two hemispheres of the spinal cord at the level of sciatic plexus
(Imhof, 1904; Lyser, 1973; Ollé, 2006; Terni, 1924). The segmentally arranged
accessory lobes protrude bilaterally from the ventrolateral surface of the spinal
cord (see Figure 4.19 A) into the vertebral canal (L. D. De Gennaro and C. A.
Benzo, 1976, 1978; Eide, 1996; Rosenberg and Necker, 2002; Vuković, Lucić, and
Ćurković, 1999). The lobes are adjacent to the region of the intimal connection
of the spinal cord with a network of supporting dentate ligaments (Eide, 1996;
Necker, 2005, 2006; Schroeder and Murray, 1987; Streeter, 1904; Yamanaka,

Kitamura, and Shibuya, 2008). The CSF is the multifunctional connective tissue that, in addition to passively protecting the soft tissue as a cushion, also acts as a nourishing, homeostasis, excretory, and lymphatic system that contributes ontogenesis of the entire organism (Johanson et al., 2008; Kaneko et al., 2008; Orts-Del'Immagine et al., 2020).

2.3.1   Spinal Canal

The unique morphology of the lumbosacral canal is formed by modified lumbar and sacral vertebrae, which invariably consist of a neural arch on the dorsal side and a vertebral body on the ventral side (Bui and Larsson, 2021; Christ et al., 2000). The neural arc is composed of the junction of the pedicle and lamina (Bui and Larsson, 2021; Mellado et al., 2011). On the dorsal side of the lumbosacral spinal canal are transverse grooves that Necker, 1999 has compared with the semicircular canals of the vestibular organ. They are formed by the fusion of modified laminas of two adjacent vertebrae along the median longitudinal sulcus (Jadwiszczak, 2014).

2.3.2   Glycogen Body

The glycogen body is a glycogen-rich cell anatomical structure distinguishing birds from other vertebrates (L. De Gennaro, 1982). Indirect measurements of the glycogen density in rat liver and human leukocytes (Scott and Still, 1970) indicate that the glycogen body is a high-density anatomical structure, denser than the spinal cord and surrounding cerebral fluid flow. The glycogen body as an avian unique anatomical structure wedged between the spinal cord hemispheres (see Figure 2.6 A) was described in adult avian species by Emmert, 1811 and one-year after in embryo by Nicolai, 1812. The subsequent studies found glycogen in vertebrates' nervous systems (Gage, 1917) and, a bit later, Terni, 1924 documented the presence of glycogen cells in a bird's unique glycogen body. The term glycogen body itself was introduced later by Watterson, 1949.
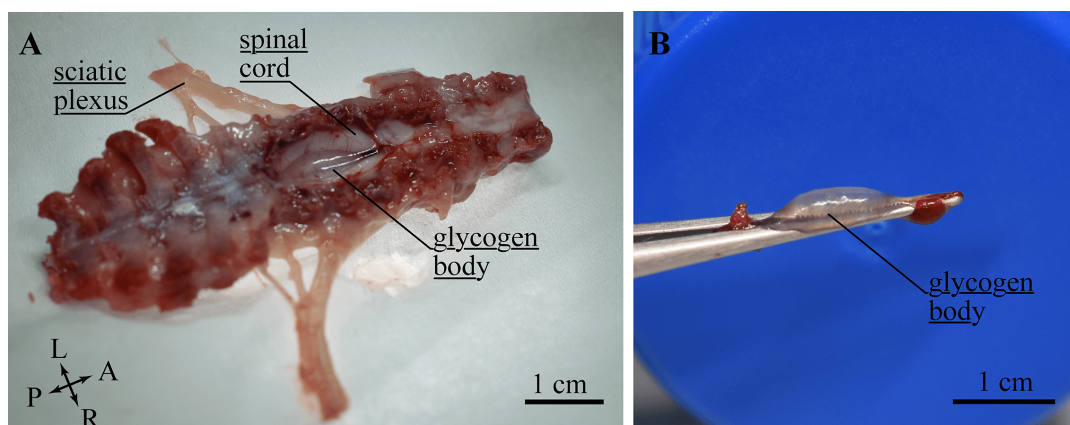
Figure 2.6: The glycogen body visible on a classically dissected young chicken. (A) The spinal canal of the cooled chicken carcass opened from the dorsal side. (B) The glycogen body pulled with tweezers out of the groove formed between the spinal cord hemispheres.

The glycogen body is richly vascularized (Vuković and Lucić, 2005) oval-shaped translucent gelatinous Figure 2.6 B) composed of glial origin (L. D. De Gennaro, 1993) cells that are potentially astrocytes (Lee et al., 2001; Lyser, 1973; Sansone, 1980; Uehara and Ueshima, 1984) and highly branched glucose polymers (C. Benzo and L. De Gennaro, 1983; L. De Gennaro, 1982; Imagawa et al., 2006; Koizumi, 1974; Necker, 2005; Ollé, 2006; Streeter, 1904). At the glycogen body location, the spinal cord hemispheres are connected only by the ventral commissure (Uehara and Ueshima, 1982; Watterson, 1949) and form intense intumescence (J. J. Baumel, 1993). But the distinctive lumbosacral enlargement is not a result of the spinal cord shape modification but because of embedded avian unique glycogen body from the dorsal side (Necker, 2005).

2.3.3   Denticulate Ligament Network

The meningeal connective tissue includes three separate mater, different by physical properties: dura, arachnoid, and pia (Streeter, 1904). The dura mater is the strongest one, lining the spinal canal (Streeter, 1904); the delicate arachnoid mater forms a mesh between the vertebral inner wall and the neural soft tissue and separates the grooves from the spinal canal, turning them into separate transverse canals (Necker, 1999; Stanchak, French, et al., 2020; Streeter, 1904); the pia mater covers the neural soft tissue (McCormick and Stein, 1990; Streeter, 1904; Watterson, 1949). The denticulate ligaments, also known as meningovertebral ligaments, emerged from the condensation of the pia membrane on the ventral side of the spinal cord (McCormick and Stein, 1990; Shi et al., 2014). The denticulate ligaments are fibrous, dense connective tissue, which, in accompaniment of vessels, extends through the arachnoid membrane, attaching between adjacent nerve roots to the dura mater (J. Baumel, 1985) with the ventral and lateral processes (R. Chen et al., 2015; Schroeder and Murray, 1987; Sillevis and Hogg, 2020). The presence of denticulate ligaments in the spinal canal is not a unique avian feature, but the topology formed by additional ventral longitudinal and transverse ligaments (Angevine et al., 2011; Schroeder and Murray, 1987). Avian denticulate ligament network consists of lateral and ventral longitudinal ligaments intersected by ventral transverse ligaments at segments' junction along the lumbosacral canal (Schroeder and Murray, 1987). The network is not homogeneous; the most prominent ligaments are longitudinally oriented strips that compose elastin and collagen fibrils (Ceylan et al., 2012; Polak et al., 2014; Schroeder and Egar, 1990; Schroeder and Murray, 1987; Tunturi, 1978). The less prominent part of the network is ventral transverse ligaments in contrast to the ventral longitudinal ligament present only within the lumbosacral segments of the avian spine (Schroeder and Murray, 1987).

2.3.4   Accessory Lobes

Longitudinally oriented ovoid shape accessory lobes (Huber, 1936; Lachi, 1889), also known as Hofmann nuclei major, are clusters containing the marginal neurons embedded in somata and glia-derived glycogen cells (Eide, 1996; Milinski and Necker, 2001; Rosenberg and Necker, 2002). Kölliker, 1902 labeled the

nuclei of Hofmann at the lumbosacral spine as major to distinguish them from less prominent structures protruding from the spinal cord hemispheres in the other regions of the avians spine (Milinski and Necker, 2001; Rosenberg and Necker, 2002). The first who described the protrusions from the spinal cord into the vertebral canal as accessory lobes ("lobi accessorii") was Lachi, 1889. The accessory lobes are located between the nerve roots (see Figure 2.7) in the spinal canal at the intersection of the lateral longitudinal ligaments and the transverse ligaments (Eide, 1996; Huber, 1936; Necker, 1997; Schroeder and Murray, 1987). The pia membrane (Rosenberg and Necker, 2002) covering each accessory lobe merges into the dorsal aspect of the lateral longitudinal ligament (Eide, 1996; Kölliker, 1902). Avian accessory lobes are identified with intraspinal mechanoreceptive neurons (Eide, 1996; Eide and Glover, 1996; Necker, 2006; Rosenberg and Necker, 2002; Schroeder and Murray, 1987; Yamanaka, Kitamura, Shinohara, et al., 2012, 2013) earlier characterized in many vertebrates (Dale et al., 1987; Henderson et al., 2019; Hubbard et al., 2016; Milinski and Necker, 2001; Wyart et al., 2009) including lampreys (Di Prisco et al., 1990a; Grillner, 1986; Hsu et al., 2013; Rovainen, 1979), turtles (Fernández et al., 1998), and zebrafish (Picton et al., 2021). The glycinergic neurons in avian accessory lobes make them comparable with stretch-sensitive mechanoreceptive domes (Stanchak, Miller, et al., 2022) described in the spinal proprioceptive organ in zebrafish (Picton et al., 2021). Moreover, immune reactive glycinergic neurons' presence in the accessory lobes potentially indicates their similar sensor function to the hair cells in the inner ear (Stanchak, Miller, et al., 2022).
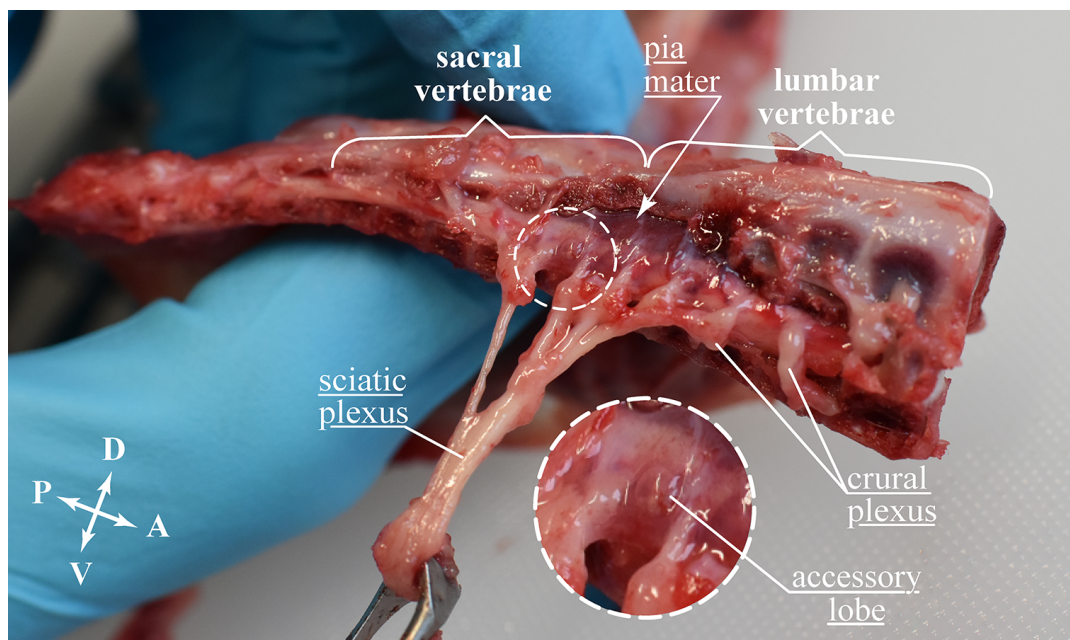
Figure 2.7: LSO soft tissue encapsulated with the pia mater filled with CSF. Right lateral view at the sagittal plane section of the classically dissected young chicken lumbosacral spine.

2.4   Functional Hypotheses about the Lumbosacral Anatomical Features

The unique morphology of the avian lumbosacral region has raised questions for decades, but the function for the morphological modifications of the anatomical structures remains controversial and unclear (J. J. Baumel, 1993; L. De Gennaro, 1982; Lachi, 1889; Rosenberg and Necker, 2002; Schroeder and Murray, 1987; Streeter, 1904). Along the way, researchers have put forward a wide range of functional hypotheses about the role of the LSO, considering the anatomical structures both as individuals and in combination. Among the hypotheses, we can distinguish the most prominent ones. Streeter, 1904 studied the lumbosacral region of the ostrich and described it as a locomotor brain interacting closely with the leg muscles. A metabolic function has been proposed for the glycogen body, according to which it acts as nutrient storage (Azcoitia et al., 1985; L. De Gennaro, 1961; Terni, 1924; Watterson, 1949). A metabolic function has been proposed for the glycogen body, according to which it acts as nutrient storage (Azcoitia et al., 1985; L. De Gennaro, 1961; Terni, 1924; Watterson, 1949). The mechanosensory hypotheses on the lumbosacral region termed the lumbosacral organ, are currently the most prevailing in the scientific environment. Putative mechanosensing function of the accessory lobes suggests the LSO perceives body movements independent of the vestibular organ in the head (Eide, 1996; Grillner, A. McClellan, and Perret, 1981; Necker, 2006; Schroeder and Murray, 1987; Yamanaka, Kitamura, Shinohara, et al., 2012, 2013). Hypothetically, the lumbosacral organ is directly involved in sensorimotor control of body position in space through direct sensory feedback to the hindlimbs (Eide, 1996; Eide and Glover, 1996; Rosenberg and Necker, 2002; Schroeder and Murray, 1987).

2.4.1   Metabolic Function

The function of the glycogen body, as a prominent avian unique anatomical structure with a high and constant glycogen content (Fink et al., 1975), has raised many questions and resulted in different hypotheses that considered its metabolic function. The glycogen stored in the glycogen body has been considered an energy source that supports a glucose level in the central nervous system during physical-induced stress (Azcoitia et al., 1985; C. Benzo and L. De Gennaro, 1983; H. Smith and Geiger, 1961) and as an osmoregulator (Azcoitia et al., 1985). However, starvation and high-intensity physical exercise experiments showed that while the liver glycogen level was already almost depleted, the glycogen level in the glycogen body remained unchanged (C. Benzo and L. De Gennaro, 1983; H. Smith and Geiger, 1961; Szepsenwol and Michalski, 1951). Studying the enzyme-specific activity explained the glycogen body's failure to free glucose by the absence of glucose-6-phosphatase involved in the synthesis and degradation of glycogen (C. A. Benzo et al., 1975; Fink et al., 1975). Revealing the oxidative pathway indicated on the potential glycogen body relation to lipids synthesis (C. A. Benzo et al., 1975), which led to the alternative idea on the glycogen body supports myelin synthesis for the avian nervous system similar to the glycogen stored in the liver and skeletal muscles (C. Benzo and L. De Gennaro, 1981,

1983; L. D. De Gennaro and C. A. Benzo, 1976, 1978). Tracing ontogenesis of the glycogen body (Watterson, 1949) and the vascular pattern within the spinal cord (Feeney Jr and Watterson, 1946) during the early embryonic life of birds allowed to hypothesize the glycogen body influence on nervous tissue development (L. De Gennaro and C. Benzo, 1987; Watterson, 1949, 1954). But despite the number of studies dedicated to the glycogen body function in avian body metabolism, none of the suggested hypotheses yielded conclusive evidence (Kamska, Daley, et al., 2020; Stanchak, French, et al., 2020).

2.4.2 Mechanosensory Function

Many studies focus on intraspinal mechanosensory inputs that probably contribute to the effective coordination of vertebrate locomotion (Henderson et al., 2019; Picton et al., 2021). Although the LSO contribution to agile locomotor remains indirect, the neurophysiological evidence suggests that balance sensing in birds is independent of the head-localized vestibular organ (Abourachid, Hackert, et al., 2011). Labyrinthectomy and transection of the spinal cord, aimed at eliminating the influence of inputs from the visual and somatosensory systems, showed that birds retain the ability to compensate for body reflexively turns, indicating the existence of an additional sensing system (Abourachid, Hackert, et al., 2011; Biederman-Thorson and Thorson, 1973). Mechanosensory neurons have already been described in many vertebrates (Dale et al., 1987; Henderson et al., 2019; Hubbard et al., 2016; Wyart et al., 2009), allowing us to identify a wide range of possible mechanisms of mechanosensory neuron activation associated with CSF flow alteration (Böhm et al., 2016; Jalalvand et al., 2016; Orts-Del'Immagine et al., 2020; Sternberg et al., 2018) and stretching neural tissue (Grillner, Williams, et al., 1984; Harrison et al., 1999; A. D. McClellan and K. A. Sigvardt, 1988; Picton et al., 2021).

Well-known candidates for sensing alterations in cerebrospinal fluid flow within the spinal canal are CSF-contacting neurons (CSF-cNs) sensitive to spinal cord curvature (Böhm et al., 2016; Jalalvand et al., 2016; Orts-Del'Immagine et al., 2020; Sternberg et al., 2018). Kolmer, 1921 and Agduhr, 1922 were the first who assumed the CSF-cNs function is similar to hair cells in the inner ear. It was recently established that the CSF-cNs bore a kinocilium which potentially can contribute to amplifying mechanosensory response (Orts-Del'Immagine et al., 2020). The establishment that spinal cord shape continuously changes under vertebrate locomotor movements (Harrison et al., 1999; Rossitti, 1993) allows assuming an intraspinal proprioceptive organ for integrated motor action feedback to guide behavior (Grillner, 1986; Grillner, A. McClellan, and K. Sigvardt, 1982; Picton et al., 2021). The classic example of stretch edge cells acting as an intraspinal proprioceptor by detecting local bandings of the spinal cord during locomotion first has been described in the lamprey (Di Prisco et al., 1990b; Grillner, Williams, et al., 1984; Hsu et al., 2013). Recently Picton et al., 2021 described an intraspinal segmental proprioceptive organ in zebrafish that detects lateral body movements through the stretching lateral neurons protruding from the ventrolateral edge of the spinal cord.

Previous studies described a unique set of morphological adaptations of the bone, soft, and connective tissue forming the avian lumbosacral region that collectively constitutes the putative intraspinal mechanosensitive lumbosacral organ (LSO). Hypothetically the LSO collects proprioceptive information through the accessory lobes excitation (Eide, 1996), but a mechanism remains unclear. Schroeder and Murray, 1987 proposed several potential mechanisms for the excitation of the accessory lobes. Each of these mechanisms was further investigated individually, although today, there is an opinion that these putative mechanisms are not necessarily mutually exclusive (Kamska, Daley, et al., 2020; Stanchak, French, et al., 2020). One of the most widespread assumptions is that the accessory lobes excitation mechanism is associated with the cerebrospinal fluid flow (Schroeder and Murray, 1987). A stretch-sensitive mechanism suggests stimulation of the accessory lobes through tension in the intimately adjacent lateral longitudinal dentate ligaments. In addition, the mechanism of stretch sensitivity suggests the possibility that the accessory lobes may also be excited through the distortion of the covering pia membrane (Rosenberg and Necker, 2002) merged with the dorsal aspects of the stretching lateral longitudinal ligaments (Eide, 1996; Schroeder and Richardson, 1985a).

LSO Sense Organ of Balance

The potential mechanoreceptive function of the accessory lobes (Eide, 1996; Necker, 1997) and their topographic anatomy relative to the transverse grooves (Necker, 1997) formed by the bony lamellae on the dorsal side of the lumbosacral canal (J. J. Baumel, 1993; Necker, 1999) allowed Necker, 1999 to hypothesize that the LSO senses body movement similar to the vestibular system of a mammalian inner ear (see Figure 2.8 A). The vestibular system is a multicomponent mechanosensing organ consisting of three orthogonally oriented semicircular canals that detect angular accelerations in three directions individually and two otolith organs in the utricle and the saccule that detect linear accelerations and gravity (Hudspeth, 1989; Obrist, 2011; Selva et al., 2009). The fluid-filled semicircular canals activate mechanoreceptive hair cells under inertial forces induced by head accelerations (Hudspeth, 1989; Selva et al., 2009). According to Necker's hypothesis, the segmentally arranged transverse grooves separated from the longitudinal lumbosacral spinal canal by arachnoid mater function as semicircular canals in the inner ear (Necker, 1999, 2005, 2006). Necker has assumed the cerebrospinal fluid flow through the grooves induced by angular acceleration experienced by birds during roll movements causes stimulation of the potentially mechanosensitive accessory lobes that are roughly aligned with the opening of the grooves (see Figure 2.8 B). The dendritic projections of the accessory lobe neurons extending into the fluid-filled lacunae have allowed Rosenberg and Necker, 2002 to assume their functional similarity with the inner ear hair cells' stereocilia. The recent discovery of glycinergic processes within the accessory lobes, which exhibit immunoreactivity for espin and myosin7 proteins, enabled Stanchak, Miller, et al., 2022 to assume that the LSO has critical evidence of a mechanosensing potential similar to that expressed by mammalian inner ear hair cells and domes in recently-described proprioceptive organ in zebrafish described by Picton et al., 2021. However, the hypothesis
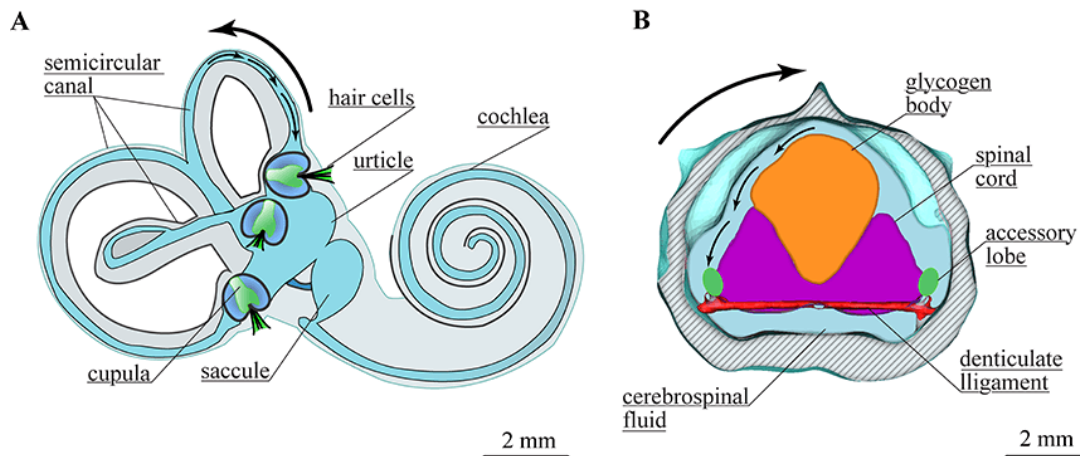
Figure 2.8: Schematics of LSO stimulation as an equilibrium organ. Necker, 1999 hypothesized the LSO stimulation consistent with the mechanism described for the vestibular organ inside the mammalian inner ear. (A) Result of the head rotation, inertial forces create a fluid flow in the semicircular canal, which by deflecting the cupula leads to mechanical stimulation of the hair cells located inside. The schematic was modified from Obrist et al., 2010. (B) Similarly, under inertia forces induced by the bird's body rolling, the CSF flows through the grooves of the lumbosacral and mechanically stimulates the accessory lobes by the transient pressure change. The schematic was modified from Kamska, Daley, et al., 2020.

that the LSO acts as the balance sensing organ does not explain the function of the topological modification of the denticulate ligament network and birds' unique glycogen body.

LSO Sense Organ of Acceleration

We suggest a new mechanosensing hypothesis, which assumes interaction between the lumbosacral specializations in contrast to the earlier ones. Relying on the hypothesis developed by Schroeder and Murray, 1987 about the ligament-strain-based mechanism of the LSO perception, we hypothesized that the lumbosacral region is encoded by signals from mechanosensory accessory lobes about the internal condition of the neural soft tissue entrained by external acceleration caused by legged locomotion. The fused lumbosacral vertebrae housed within the synsacrum prevent the bending of the spinal cord (Stanchak, French, et al., 2020) that would occur in response to locomotor movements. However, the overly developed cerebrospinal fluid-filled space surrounding the distinct spinal cord shape, loaded with a high-density glycogen body, suggests that the spinal cord is experiencing deformation inside the lumbosacral spinal canal. We assume that the glycogen body tunes and amplifies localized spinal cord oscillations resulting in the denticulate ligaments strain (see Figure 2.9 A), which according to Schroeder's (Schroeder and Murray, 1987) assumption, stimulates the adjacent accessory lobes at the stretching. Additional recent evidence supporting the putative LSO mechanosensing function associated with the ligament strain through the spinal cord deformation is discovering neurons in the accessory lobes reminiscent of the spinal-bend-sensitive glycinergic neurons (Stanchak, Miller,
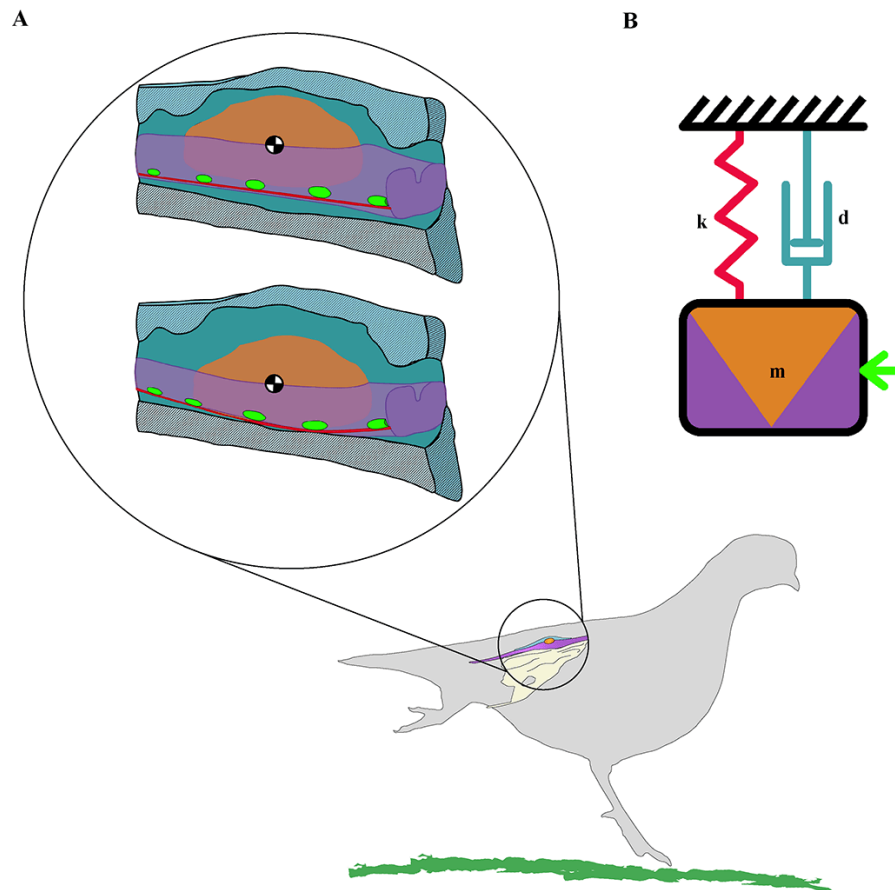
Figure 2.9: Schematics of LSO stimulation as a mass-spring accelerometer.
(A) The Schematic illustrates the hypothetical spinal cord movements inside the lumbosacral spinal canal in response to external accelerations caused by avian locomotion. Hypothetically the high-density glycogen body may act to tune and amplify localized oscillations of the spinal cord, which causes stimulation of the accessory lobes through the ligaments stretching. (B) The hypothetical response of the LSO anatomical structures to the external acceleration is reminiscent of a fluid-filled mass-spring-based accelerometer. Bird's outline was modified from Jerry Ting, 2013, and synsacrum was modified from (Commons, 2009).

et al., 2022) recently described in zebrafish spinal proprioceptive organ (Picton et al., 2021). We hypothesize that collectively the fluid-filled spinal canal housing the hammock-like network of denticulate ligaments supporting the lumbosacral spinal cord loaded with the glycogen body and the close connection between the accessory lobes and lateral ligaments make the LSO reminiscent of a fluid-filled mass-spring-damper (see Figure 2.9 B) system susceptible to acceleration caused by vertical oscillations during locomotion (Kamska, Daley, et al., 2020).

Chapter 3

3D Anatomy of the Quail Lumbosacral Spinal Canal

Topic

This project develops a 3D anatomy of the LSO based on digital and classical dissection approaches. The goal was to establish whether anatomical and biomechanical features indicate similarity to a fluid-filled mass-spring-damper system.

Motivation

As was introduced in Chapter 2, the unique anatomical features of the avian lumbosacral region have already been known for over 100 years, but their function remains unclear. Earlier suggested Necker, 1999 hypothesis on a mechanosensory function explored the possibility of the LSO acting similarly to the inner ear. However, the assumption that only the transverse grooves, reminiscent of the inner ear semicircular canals, generate the mechanosensory response in the accessory lobes does not explain the presence and function of other unique anatomical adaptations of the lumbosacral region that distinguish birds from all other vertebrates. Schroeder and Murray, 1987 and Eide, 1996 hypothesized a mechanism of mechanosensor excitation within the accessory lobes based on ligament tension. To establish whether the mechanism of mechanosensory excitation is more consistent with excitation of the accessory lobes through ligament tension or cerebrospinal fluid flow, we aim to characterize the geometrical and biomechanical properties of unique anatomical adaptations relevant to potential mechanosensory functions. In this project, we investigate the lumbosacral region using a combination of digital and classical dissections. We attempt to quantify the possibility of the spinal cord and the denticulate ligament network deformation under the loading of a high-density glycogen body.

Synopsis

Birds belong to one of the most diverse classes of vertebrates that share the ability to move with exceptional agility in almost any environment on Earth. The unique morphology of birds' lumbosacral region, located at the sciatic and

crural plexuses, indicates a potential intraspinal mechanosensory function. The intraspinal anatomical adaptations are known collectively as the lumbosacral organ (LSO), distinguishing birds from other vertebrates. The LSO consists of a glycogen body unique to birds, wedged between the hemispheres of the spinal cord, supported by a highly structured network of denticulate ligaments. In each segment, along the lateral edges of the spinal cord, accessory lobes protrude inside the spinal canal roughly near the opening of transverse grooves formed on the dorsal side of the lumbosacral canal. The LSO function was raised a long time ago but remains unclear. Combining the μCT and stereomicroscope of quail LSO allowed us to consider the anatomical features together and hypothesize that the LSO reminiscent of a mass-spring-based accelerometer. We suggest the acceleration force sensation function for the LSO. The quantification of the geometric and biomechanics properties of the LSO established an oscillation possibility for the neural soft tissue inside the expanded fluid-filled spinal canal.

3.1 Materials and Methods

One of the main contributions of this project was to establish an adequate 3D model of the lumbosacral organ that includes key anatomical structures related to the hypothesized mechanosensing function. We approached a combination of digital and classical dissections of a common quail (*Coturnix coturnix*) samples. The 3D model of the quail lumbosacral organ was used for developing its biophysical model (see Chapter 5). The digital dissection aimed to create a new 3-D map of the soft tissue embedded inside the lumbosacral canal. We approached a digital dissection by μCT scanning and segmented in 3D using diffusible iodine-based contrast-enhanced computed tomography (diceCT) (Gignac and Kley, 2014; Metscher, 2009a). We complemented our study with a classical stereomicroscope dissection to obtain additional details about fine denticulate ligaments' structure.

3.1.1 Digital *in situ* Dissection

Sample Processing for Scanning

A quail carcass was obtained from a commercial breeder (Fayre Game farm, UK) and processed following the diceCT protocol (Metscher, 2009a). The lab of Royal Veterinary College has processed the sample for the μCT scanning step. At the first processing step, the synsacrum was isolated from the rest of the quail carcass. The isolated sample was immersed in 10% neutral-buffered formalin (NBF) for three days and then transferred to 1% commercially-available Lugol's iodine solution for 49 days (Sigma, Life science, L6146).

Micro-computed Tomography

μCT scans were performed at the Royal Veterinary College Imaging suite by Dr. Michael Doube. The scanning was done with a micro-computer tomography machine (Skyscan 1172), operated at $80\,kV$ and $124\,\mu A$. 1030 raw images (dark objects against a bright background) were taken within one 360° rotation, with an increment of 0.35° and an integration time of $500\,ms$ per image. The three images at each angular position were averaged, and we received raw images of 1000 by 668 pixels. After calculating the back projection, the isotropic voxel size of the resulting image stack of 634 images (TIFF format, bright signal on a black background) was $27\,\mu m$.

3D Segmentation of a Quail LSO

Three-dimensional segmentation, 3D surface model generation, morphometric analysis, and biomechanical properties estimation have been done using Amira software (version 6.5.0 Visage Imaging, Berlin, Germany). Depending on the shape and orientation of the anatomical structures, we switched between different orientation working planes. For the segmentation of the relatively large structures: a synsacrum, a cerebrospinal fluid (CSF) space, a spinal cord, and a glycogen body, we approached a combination of semi-automatic labeling using

the threshold function and manual labeling; we interpolated labeled region between 2 to 7 slices. The denticulate ligaments' segmentation was manual on each related slide, constantly switching working planes. Each anatomical structure was extracted from the segmentation project as a single "Label Field" file in Amira Mesh [AM] format (Ruthensteiner and Heß, 2008). Using the "Surface Gen" module, each anatomical structure of the lumbosacral organ was generated as a separate 3D model. The meshes of the generated 3D models had a large number of polygons, overlapping in some spots and forming a non-manifold. For facilitating morphometric analysis with the lowest possible computational cos, the surface of each 3D model was closed, and the number of triangles was reduced using Autodesk Maya (version 2019) (Molnar et al., 2012). The 3D models were exported from Amira to Maya in [STL] format. All non-manifolds were removed, the remaining holes were closed manually, and the edges of the polygonal meshes were smoothed by applying the "Sculpt Geometry" tool (Buchanan et al., 2014) (see Figure 3.1). After cleaning up the polygonal meshes, we exported 3D models as [STL] files and re-imported them into the Amira for further geometric morphometric analysis.
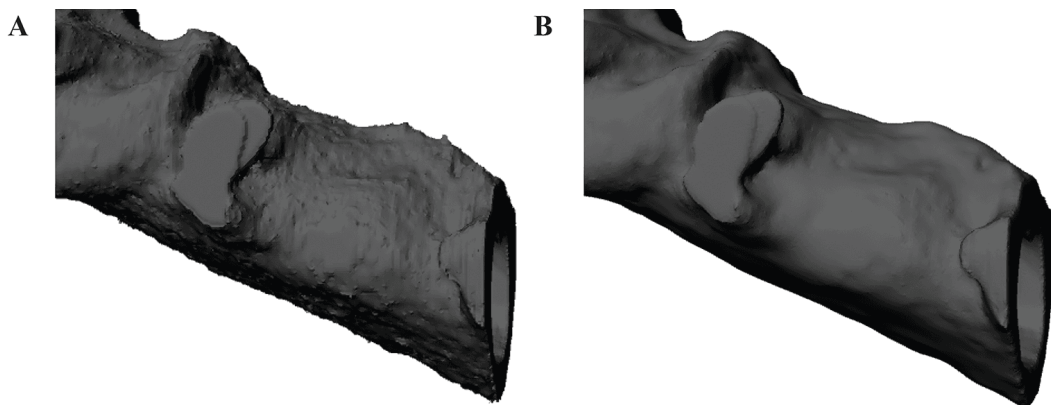
Figure 3.1: Clean up the mesh and reduce polygon count. A 3D cerebrospinal fluid space model illustrates an example of model processing using Autodesk Maya. An anterior part of the surface (A) before and (B) after cleaning.

3D Segmentation of Denticulate Ligament Network

The denticulate ligaments are the finest structures we could determine on μCT data. The general thickness of the identified parts of the ligaments varies within a few voxels (voxel equals 27 µm). The default orientation of the coronal virtual slices of the μCT data did not allow observing an entire network's topology but only a few separated recognizable pieces of ligaments. Since the thickness of the denticulate ligaments is close to the image resolution and the shape of the network is irregular, a dedicated approach had to be developed to achieve the highest possible accuracy in the segmentation. We segmented the denticulate ligament network in an individual segmentation project from the CSF space, the glycogen body, the spinal cord, and the bony parts of the synsacrum. In the first step, we rotated the default orientation of the coronal virtual slices along the spinal canal direction up to the moment when the outline of the

entire network had become visible on a single coronal slice. Then, all related isotropic slices with the new coronal orientation were exported from Amira individually and imported into the new Amira project as a single image stack. Based on re-sliced μCT data, the denticulate ligament network was segmented in 3D using the manual tool "paintbrush" (see Figure 3.2 B). For the final step, we needed benchmarks for merging the 3D model of the denticulate ligament network with the rest of the lumbosacral organ models. As the benchmarks, we segmented the denticulate ligaments' pieces visible along with the rest of the lumbosacral anatomical structures on the μCT data in its default orientation (see Figure 3.2 A). In the last step, we added the network 3D model to the general lumbosacral organ by overlaying the common parts of the denticulate ligaments (see Figure 3.2 C).
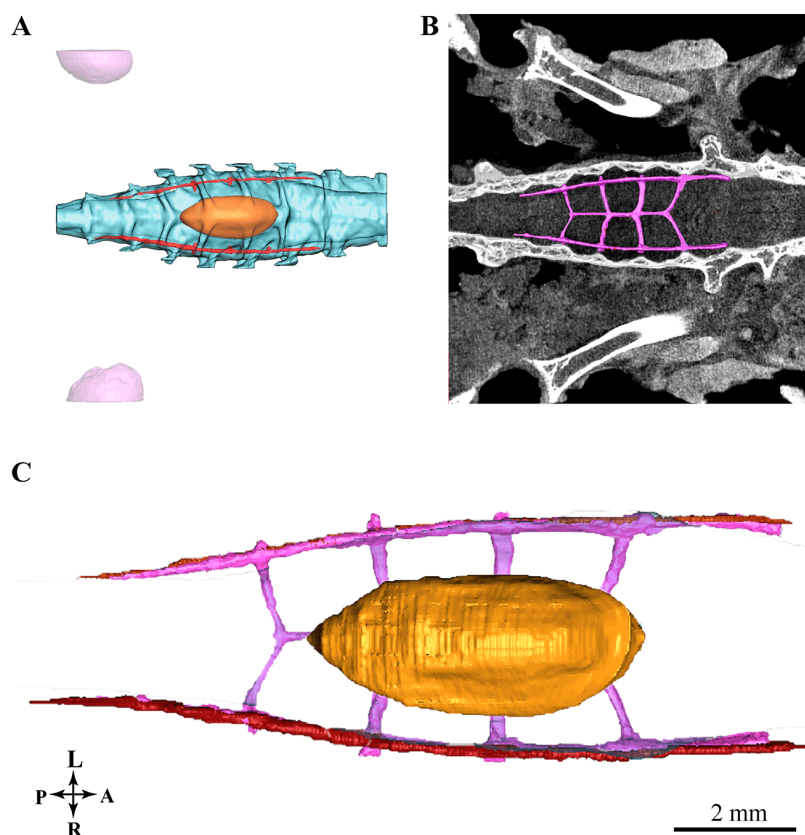
Figure 3.2: Merging a 3D model of the denticulate ligament network with a 3D model of the lumbosacral organ. (A) Particles of denticulate ligaments segmented on the μCT data in its default orientation were used as benchmarks for merging the (B) 3D model of the denticulate ligaments network separately segmented on the re-sliced the μCT data in parallel to the network orientation. (C) The dorsal view on the denticulate ligaments network merged with the general lumbosacral organ model on the ligaments' benchmarks.

3.1.2 Classical Dissection

Three frozen carcasses of adult female common quail (*Coturnix coturnix*) (E. P. Reese and T. W. Reese, 1962) we obtained from a commercial breeder (Kitzingen,

Germany). The birds' average weight was $(170 \pm 5)\,$g and the body size varied between 10 cm to 12 cm. Since thawing causes heat stress to the soft tissues (Müller-Schweinitzer, 2009; Zhang et al., 2005), to minimize the damaging effect caused by thawing, we did not accelerate the process by increasing the temperature but left the carcasses to thaw at room temperature of about 19 °C to 20 °C. At the initial processing step, we dissected all carcasses following the practice described by Gurtovoy et al., 1992. After slow thawing, we cleaned the skeletal area of the synsacrum out of flesh and severed the thoracic and caudal vertebrae from its anterior and posterior sides. Immediately after the isolation step, we stored the synsacrum in a closed vessel at 4 °C temperature to minimize dehydration and autolysis of the soft tissue embedded inside the lumbosacral spinal canal. The synsacrum's surfaces we photographed using Nikon D5500, lens Nikon AF-S Nikkor 35 mm f/1.8G ED in three anatomical positions (see Figure 3.3 A, B, C). We cut the pelvic girdle bones off the lumbosacral canal to simplify the manipulations with the sample in the limited space between the microscope's stage and the objective. The subsequent step of a fine dissection we conducted under a fluorescent stereomicroscope Leica DFC digital 7000-T, 2.8 megapixel sensor, pixel size 4.54 µm. The vertebral canal was opened from the dorsal side along the coronal plane, following the intervertebral foramen (see Figure 3.3 D). A spinal cord and a glycogen body were neatly removed from the dorsal side of the canal using absorption spears with a cotton sponges tip to preserve the topology of the supported denticulate ligament network.

3.1.3 Measurements and Data Analysis

The morphology of the avian lumbosacral region is unique and complex in its composition. To understand an interdependence of morphology and function, we characterized geometric and volumetric properties of hard, soft, and connective tissues and explored the biomechanics potential of ligaments for stretching. The classical dissection complemented the information on the anatomical structures missed in 3D lumbosacral organ models due to insufficient contrast of μCT data.

Determining the Coordinate Origin

Before extracting and analyzing the morphometric data, we needed to develop an approach to quantify the biological shapes of the lumbosacral tissue. The approach should apply to any great variety of birds' lumbosacral region shapes. We chose criteria for establishing a local coordinate system for rigid bone morphological features of the synsacrum that are phenotypically different in shape but inherent in all birds. The coronal plane was aligned along the narrowest region in each segment formed by the fusion of adjacent vertebrae. The classical dissection confirmed our assumption that these narrowest regions of the spinal canal are ligament attachment spots. Transverse and sagittal planes are the coronal plane turned 90 degrees. The transverse plane is adjacent to the heads of the left and right femurs. The sagittal plane is adjacent to the segmentally highest points of the lumbosacral canal formed by vertebral fusion.
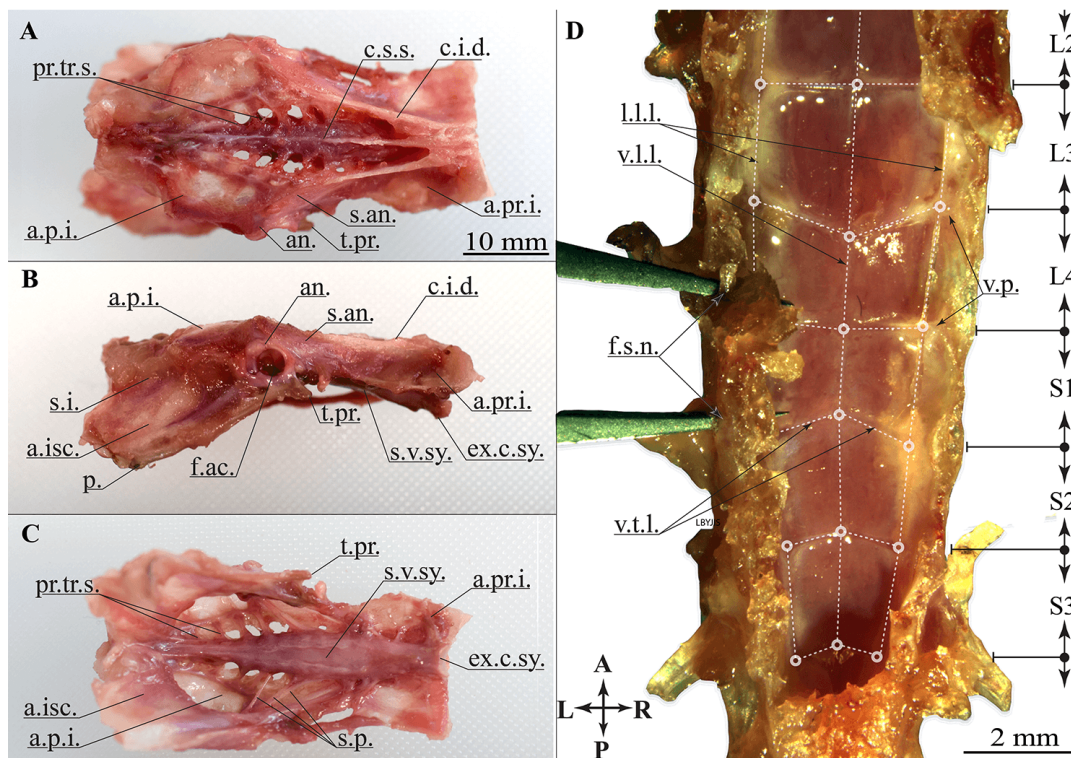
Figure 3.3: Anatomy of the synsacrum, classical dissection (from Kamska, Daley, et al., 2020). (A) dorsal, (B) right lateral, and (C) ventral view. A-C shows the intact synsacrum with a closed lumbosacral canal. Posterior left and anterior right. (D) shows the spinal canal opened from the dorsal side. The glycogen body and spinal cord are removed to reveal the denticulate ligaments in the region of the glycogen body (S2 to L4). The dentate ligaments are highlighted with dashed white lines, and the network intersection nodes are shown with circles. The tips of the forceps are inserted through the foramen of the S1 and L4 vertebrae. See abbreviations in Table 1.

Morphometrics

The lumbosacral anatomical structures' geometric morphometry was measured using Amira applying landmarks to the 3D models. We settled transverse cut planes segmentally at the vertebral fusions (continuous lines) and mid-vertebral regions (dashed lines) (see Figure 3.4 A). Because the lumbosacral canal shape is irregular, the transverse cut planes are not parallel but follow anatomical features of the spinal canal. The mid-vertebral regions' cut planes were established using a sagittal plane of the lumbosacral canal. Dorsally and ventrally, each plane was set at the midpoint between the adjacent slice planes of the vertebral fusion regions. Besides, based on the glycogen body prominence, we distinguished two regions of the lumbosacral canal: vertebrae with the glycogen body (see Figure 3.4 B) - from the fourth lumbar to the second sacral; vertebrae without the glycogen body (see Figure 3.4 C).

Volume Measurements

We extracted volumetric measurements of the spinal cord, glycogen body, and CSF using Autodesk 3ds Max (version 2018). Measurements were limited to the
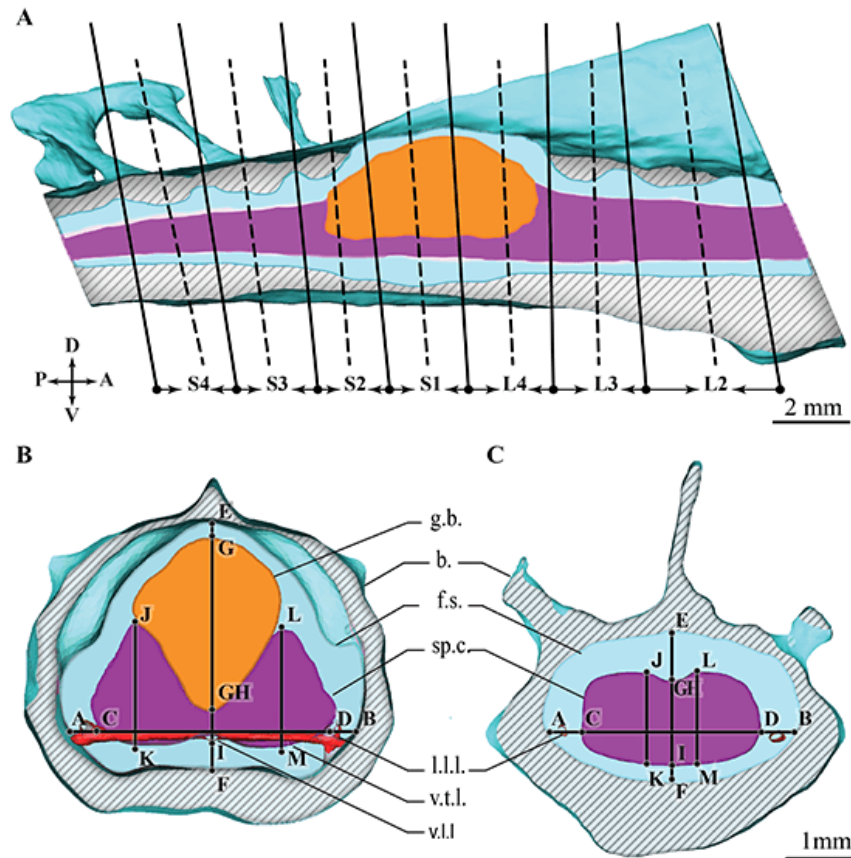
Figure 3.4: Schematic sections through the quail lumbosacral organ (modified from Kamska, Daley, et al., 2020). (A) Sagittal section through the spinal canal, right lateral view. Solid black lines present the cut planes at the vertebral fusion regions. Dashed black lines are the cut planes at the vertebral middle regions. (B) Transverse section through the lumbosacral region at S1 and L4 vertebrae fusion. (C) Transverse lumbosacral section cutting at the L3 and L2 vertebrae fusion area. See abbreviations in Table 1.

lumbosacral region. Hence, to avoid errors in addition to the full sample volume evaluation, we also estimated the volume ratio of soft and connective tissue in each segment separately. We separated segments on the transverse cut planes set at the vertebral fusion regions (see Figure 3.4 A). This approach allowed us to study the dependence of the soft tissue volume variations and the space available for their potential movement within the spinal canal on the region of the lumbosacral canal.

Calculation of Ligaments' Tensile Potential

We examined the soft tissue potential for oscillation within the lumbosacral canal. According to the available space filled with cerebrospinal fluid, we evaluated its maximum possible displacement. We suggest the hypothetical displacement results in the deformation of the spinal cord and denticulate ligaments at the lumbosacral region. Stiffness and recovery after deformities of the spinal cord
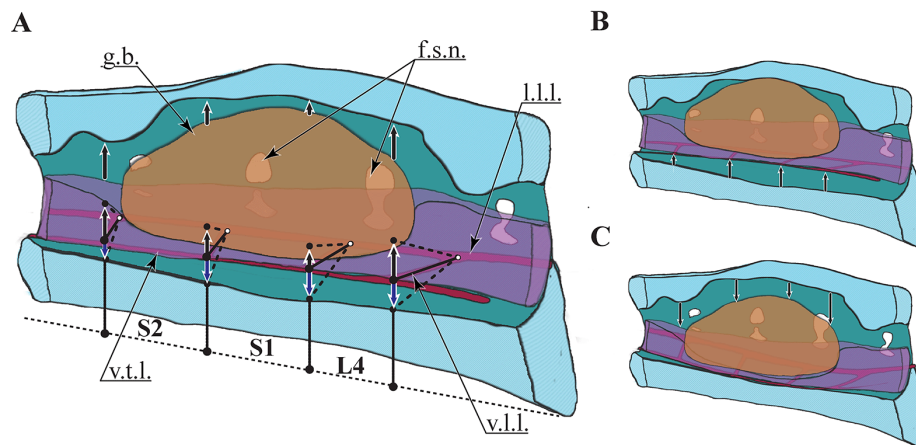
Figure 3.5: Potential for soft tissue movements and ligaments deformation
(from Kamska, Daley, et al., 2020). The soft tissue in the (A) resting, (B) upper, and
(C) lower positions. Ligaments are indicated in red. Black arrows indicate up-and-down
movements of the neural soft tissue. The nodes are defined as the intersection of
the ventral transverse and ventral longitudinal ligaments. The dashed lines show
the ventral transverse ligaments when deformed. White range symbols indicate the
estimated angular deflection of the transverse ligaments. See abbreviations in Table 1.

are provided by the surrounding pia-arachnoid complex (Ramo et al., 2018).
Birds' unique pia-arachnoid complex includes the denticulate ligament network,
presumably producing countering forces, similar to a hammock under loading
(see Figure 3.5). For simplicity, we evaluated the deformation of the transverse
ligaments using its simplified model and assumed that the spinal cord-pia-
arachnoid construct deforms along the sagittal plane. The fluid space available
for the potential movements we extracted from the digital dissection of the quail
lumbosacral region. Along the sagittal plane, we measured the vertical distance
range between the glycogen body top and the spinal canal dorsal and between
the spinal cord ventral surface and the spinal canal ventral. To simulate soft
tissue movement to the dorsal side, we averaged the ventral distance measured
in the middle region of the adjacent vertebrae (for example, the average of M-S3
and M-S2 for S3-S2). This simplification of the dorsal side canal morphology
was essential for avoiding over-estimation of the soft tissue movement toward
the dorsal side by including additional height of transverse semi-circular grooves
at the vertebral fusion. Moving toward the ventral side of the canal, we did not
measure the ventral vertical distances below the spinal cord. We measured the
denticulate ligaments' length along the coronal plane at a static state. For this
aim, we used data extracted by μCT and stereomicroscope. The measurement
results of the left and right transverse ligament lengths (L) in three classically
dissected specimens and one digitally dissected specimen were averaged. We
calculated the potential maximum length (l) for stretching transverse ligaments
toward the dorsal and ventral sides of the lumbosacral canal by using the

Table 3.1: Densities ρ of soft tissue inside the lumbosacral spinal canal. The soft tissue density values we took from the cited reference sources. In our calculations, we apply the glycogen density's lower bound.

	Density [g/cm³]	Reference
CSF	1.00	Higuchi et al., 2004; Lui et al., 1998
Spinal cord	1.04	Siegal et al., 1988 (rat spinal cord)
Glycogen	1.40 - 1.48	Scott and Still, 1970 (rat liver, human leukocytes)

Pythagorean theorem and its nominal strain.

$$\left\{ e = \frac{l-L}{L} \right. \tag{3.1}$$

Effective Force from Larger-than-buoyant Glycogen Body Density

The glycogen body and spinal cord surrounded by meninges are submerged in the CSF with a density equal to the water $(1.00\,\text{g/cm}^3)$. This indicates that the specific gravity of the spinal cord and glycogen body immersed in CSF equals their density:

$$\left\{ \text{SG} = \frac{\rho}{\rho_{\text{H2O}}} \right. \tag{3.2}$$

The density of the spinal cord is slightly higher than that of the CSF, which indicates its minor tendency to sink Table 3.1). Currently, no studies have measured glycogen body density. Still, the density of glycogen is significantly higher than CSF, suggesting a glycogen body can cause a deformation of the spinal cord and dentate ligament network with a normal force F_{N} corresponding to the effective, submerged weight of the glycogen body. Here, we calculated the effective force imposed by the glycogen body on the spinal cord and the spinal cord on the dentate ligament. The applied simplified system assumes atmospheric pressure, without effects from the height of a fluid column, and that soft tissues are incompressible. The effective, normal force $_{\text{N,eff}}$ of tissue submerged in CSF was calculated as:

$$\left\{ \begin{aligned} F_{\text{N,eff}} \ &= m_{\text{ti}} \cdot g - \rho_{\text{CSF}} \cdot V_{\text{ti}} \cdot g \\ &= \rho_{\text{ti}} \cdot V_{\text{ti}} \cdot g - \rho_{\text{CSF}} \cdot V_{\text{ti}} \cdot g \\ &= \Delta\rho \cdot V_{\text{ti}} \cdot g \end{aligned} \right. \tag{3.3}$$

where m_{ti}, V_{ti}, and ρ_{ti} are the mass, volume, and density of the tissue of interest, respectively. ρ_{CSF} is the density of CSF, and $g = 9.81\,\text{m/s}^2$ is the gravitational acceleration. The glycogen body's specific gravity $(\text{SG}_{\text{GB}} = \frac{\rho_{GB}}{\rho_{CSF}})$ provides a similar understanding of its floating vs. sinking behavior when submerged in CSF.

3.2 Results and Discussion

This study characterized the 3D anatomy of the common quail lumbosacral region. We focused on topographic anatomy, geometric morphometry, and biomechanical properties of the anatomical structures relevant to possible mechanosensing functions of an avian lumbosacral organ. The 3D model of the LSO allowed quantifying the fluid space around potentially movable soft tissue. The likelihood that the glycogen body has higher specific gravity than the surrounding CSF and higher effective normal force than the spinal cord in the same area (50 μN vs. 10 μN, respectively) suggests that the glycogen body causes a spinal cord deformation under acceleration. The digital and classical dissection methods allowed us to study the identified topology of the denticulate ligament network, which ventrally supports the spinal cord (Polak et al., 2014; Schroeder and Murray, 1987). The ligament's topology data and morphometrics data on the spinal canal space filled with a cerebrospinal fluid allowed us to estimate the maximum potential strain of the ligaments under the spinal cord deformation along with the sagittal plane. We assume that the pre-stressed denticulate ligament network allows the spinal cord to deform under the load of the high-density glycogen body leading to soft tissue oscillations induced by external accelerations. The assumption is that the mechanoreceptive protrusions out of the spinal cord, called accessory lobes, sense soft tissue oscillations. The potential sensitivity of the soft tissue to external acceleration with movements suggests that the lumbosacral organ functions similarly to an accelerometer.

3.2.1 Morphometrics

Morphometric analysis and evaluation of the topographic anatomy found evidence to support our assumption that a potential LSO mechanosensing function is associated with the lumbosacral soft tissue oscillation inside the canal. We observed that the distinct spinal canal enlargement and the topology of the denticulate ligament network indicate an association with the glycogen body's shape and its center of mass. The 5.2 mm long glycogen body (see Table 3.3) locates the mid-length of the lumbosacral canal between the three vertebrae L4, S1, and S2, which correspond to the most pronounced spinal canal enlargement in all directions along the transverse plane (see Figure 3.6). The greatest height of the glycogen body, equal to 2.5 mm (see Figure 3.7 G-GH), was detected along the plane of the transverse section at the fusion of S1 and L4 vertebrae, where the canal has the maximum height, 3.7 mm (see Figure 3.6 E-F). Along the same plane, we discovered the largest ventral fluid space below the spinal cord, equal to 0.6 mm (see Figure 3.8 I-F). Whereas, outside the high-density glycogen body prominence, the overall height and width of the lumbosacral canal and the ventral fluid space below the spinal cord reduce from the anterior (lumbar vertebrae) to posterior sides (sacral vertebrae). The height and width of the canal reduce from 2.5 mm/3.2 mm (H/W at L2-L1) to 1.7 mm/2.2 mm in S5-S4 (see Figure 3.6 E-F and A-B). The fluid space below the ventral side of the spinal cord reduces from 0.4 mm at L2-L1 to 0.1 mm at S5-S4 (see Figure 3.8, I-F). Observing segmental overdevelopment around the glycogen body may be related to potential soft tissue oscillation. The glycogen body putatively functions as an
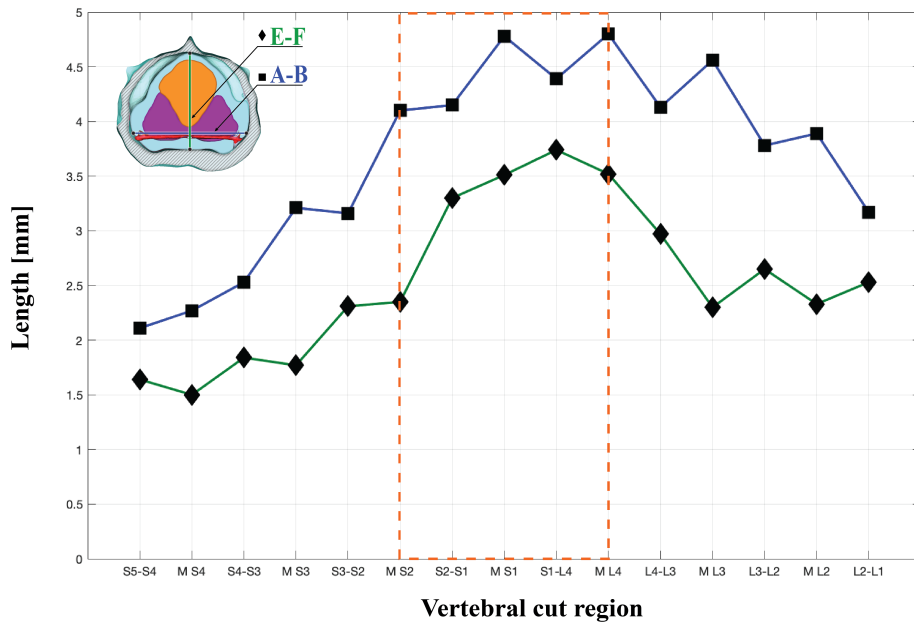
Figure 3.6: Morphometrics of the lumbosacral spinal canal (from Kamska, Daley, et al., 2020). A-B (blue curve, square markers): spinal canal width. E-F (green curve, diamond markers): spinal canal height. Orange dashed-line rectangular shows the glycogen body location region relative to the lumbosacral canal vertebral regions.

amplifier - the hypothesis we tested with a biophysical simulation and described the results in Chapter 5.

Visually the spinal cord morphology looks modified where the glycogen body is wedged between both hemispheres. To evaluate the change morphometrically, we measured the width along the coronal plane set at the level of the lateral longitudinal ligaments. We measured the spinal cord height along the parasagittal planes aligned respectfully to the top points on the left and right hemispheres and along the sagittal plane to evaluate the height variation of the connecting bridge between both hemispheres. The parasagittal height and width of the spinal cord reduce from the lumbar part toward the sacral part of the spinal cord, except for the glycogen body location region (see Figure 3.7 C-D, L-M). According to the averaged parasagittal measurements at the L3-L4 vertebral fusion region, maximum vertical spinal cord extension equals 1.9 mm (see Figure 3.7 L-M). The lateral extension also follows the trend of the spinal canal space by reaching a maximum in the middle of the L4 vertebra (3.6 mm) (see Figure 3.7 C-D). The change in the bridge height between the hemispheres also shows a dependence on the location of the glycogen body (see Figure 3.7 GH-I). Between L4 and S2 vertebrae, the hemispheres are barely connected with a bridge height equal to 0.4 mm. We suggest that the extension of the hemispheres in height and width could result from shape modification to maintain the stability of the lumbosacral soft tissue. We assume that the extension in height is aimed at holding a glycogen body; in width to prevent the spinal cord from rolling. The bridge height reduction may also stabilize the glycogen body by lifting down its center of mass to the level of the hemispheres' top points. We will check the
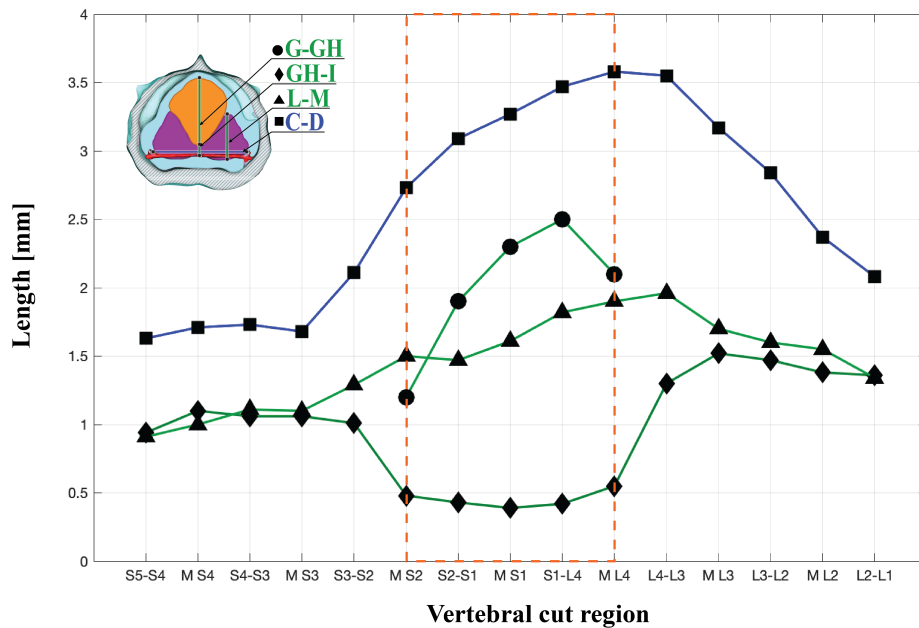
Figure 3.7: Morphometrics of the LSO soft tissue (from Kamska, Daley, et al., 2020). Abbreviations: C-D spinal cord width with square markers, G-GH glycogen body height with circle markers; GH-I middle of the spinal cord height shown with triangle markers, L-M spinal cord hemisphere height, diamond markers. Orange dashed-line rectangular shows the glycogen body location region relative to the lumbosacral canal vertebral regions.

spinal cord volume parameter to examine whether the enlargement is only a shape modification potentially caused by the glycogen body presence (see the following subsection).

The shape of the vertical lumbosacral canal expansion under the spinal cord at the glycogen body location region shows no segmental dependency associated with fusion or middle vertebral regions (see Figure 3.8). From the sagittal plane, for about 2 vertebrae between S1-L4 and M-S1, the expansion is distinctly seen as a dip (see Figure 3.4 A). The fluid space below the spinal cord at the region of the ventral dip exceeds three times that at the rest of the lumbosacral canal. Based on this observation, we hypothesized that the dip influences the soft tissue response amplitude. Approaching the biophysical simulation, we tested our assumption and described the results in Chapter 5. The dorsal side expansion of the canal is not regular and smooth but has transverse semicircular grooves resulting from the vertebral fusions. These grooves increase the dorsal vertical space of the canal. But the shape and size of the grooves are different. They vary along the vertebral canal, which can be seen in the plot (see Figure 3.8, E-G) by comparing the spikes at the vertebral fusion sites. The maximal spikes equal to 1.5 mm and 1.1 mm at the L3-L4 and S3-S2, which is beyond the region of the glycogen body prominence (Figure 3.8, E-G). Whereas the smallest spike equals 0.3 mm is at the fusion of the S1 and L4 vertebrae, exactly where the maximum height of both the lumbosacral canal and the glycogen body is. The transverse
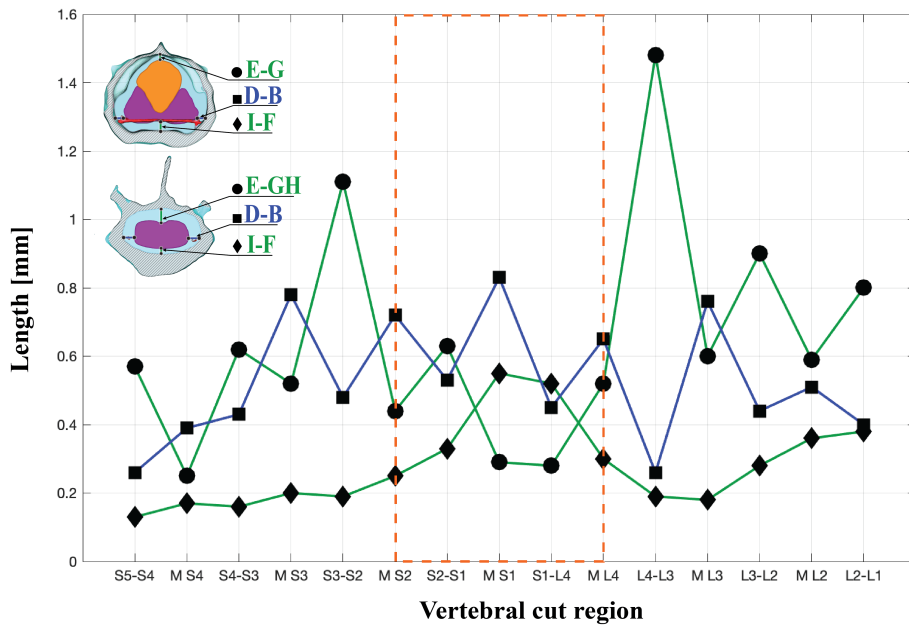
Figure 3.8: Morphometrics of the cerebrospinal fluid space (from Kamska, Daley, et al., 2020). E-G vertical distance between the glycogen body top and the spinal canal dorsal (circle markers), E-GH vertical distance between the spinal cord and the spinal canal dorsal in the range outside the glycogen body (circle markers), I-F vertical distance between the spinal cord ventral surface and the spinal canal (diamond markers), D-B horizontal, lateral distance between the spinal cord and the spinal canal (square markers). Orange dashed-line rectangular shows the glycogen body location region relative to the lumbosacral canal vertebral regions.

dorsal grooves are separated from the main longitudinal spinal canal by an arachnoid membrane (Necker, 2005; Stanchak, French, et al., 2020) and open into the canal roughly at the level of interconnection the denticulate ligament network with potentially mechanosensitive accessory lobes (Necker, 2006; Schroeder and Murray, 1987; Stanchak, Miller, et al., 2022; Yamanaka, Kitamura, and Shibuya, 2008) that protrude from the ventrolateral edge of the spinal cord (Eide, 1996; Necker, 1999). The topographic anatomy and morphometry let us assume that the transverse grooves contribute to the LSO mechanosensation by affecting the resistance of the cerebrospinal fluid flowing around moving soft tissue. We tested the hypothesis that grooves act as fluid relieves or simple flow canals using the modular LSO biophysical model (see Chapter 5).

We analyzed the lateral fluid space between the soft tissue and the spinal canal to assess all possibilities of soft tissue movement and cerebrospinal fluid flow. The left and right lateral distances between the spinal cord and the spinal canal are reminiscent of a "zig-zag" pattern from the coronal plane. The lateral lumbosacral expansion revealed an even more pronounced difference between the vertebral fusion regions and the middle vertebrae regions than the vertical canal extension on its dorsal side. In summary, the lateral extension of the fluid space exceeds the vertical one (see Figure 3.8). Segmentally, the highest extensions are

Table 3.2: Soft tissue volume and effective normal forces of the glycogen body. The volume of each soft tissue was measured segmentally in [mm³]. The effective normal forces (F_N of the glycogen body were calculated in [µN]) relatively to an appropriate vertebral segment.

Vertebra			S4	S3	S2	S1	L4	L3	L2	∑ S4-L2
Spinal cord	Volume	[mm³]	2.8	3.9	5.5	7.5	11.8	10.7	10.2	52.4
Glycogen body	Volume	[mm³]	-	-	1.4	6.8	4.8	-	-	13.0
CSF	Volume	[mm³]	3.3	5.6	8.3	11.5	10.8	14.3	10.8	64.6
Spinal canal ∑	Volume	[mm³]	6.1	9.5	15.2	25.8	27.4	25.0	21.0	130.0
			3.3	5.6	8.3	11.5	10.8	14.3	10.8	64.6
Glycogen body	$F_{N,eff,1.40}$	[µN]	-	-	5.5	26.7	18.8	-	-	51.0

in the middle vertebrae region (see Figure 3.6A-B). The largest lateral extension of the canal is at the middle of the vertebrae S1 and L4 (MS1 and ML4 are equal to 4.8 mm) at the glycogen body location. But compared to the overly developed vertical extension of the fluid space below the spinal cord holding the glycogen body, the lateral fluid space extension is monotonously following the left and right spinal cord edges of all lumbosacral vertebral segments. In plot Figure 3.8 D-B, we see that segmentally the space reduces smoothly transiting from lumbar vertebrae (2x 0.4 mm at L2-L1) towards sacral vertebrae (S5-S4 2x 0.15 mm)). The prominent "zig-zag" pattern allows us to assume that the soft tissue deformity toward the lateral side is unlikely. The narrowest point of each segment formed by vertebral fusion is the attachment area of the denticulate ligament network along the whole lumbosacral canal. The middle fluid expansion is the most oversized relative to a segment. The middle fluid expansion coincides with the location of the spinal nerve foramina. Analysis of canal morphology suggests that the medial expansions function as fluid relief pathways. After the fluid flows out of the grooves, we assume it splits against the accessory lobes, which sit on the junction of the ligaments' intersection (Eide, 1996; Necker, 1999; Schroeder and Murray, 1987). Then, presumably, fluid flows toward the dip through the lateral expansion. This assumption is based on morphological data and requires fluid dynamics simulation verification.

3.2.2   Volume Measurements

The lumbosacral canal, segmented in 3D from L2 to S4, allowed us to estimate the percentage of each anatomical component's available space. The glycogen body's total volume is 13 mm³ which 19 % of the lumbosacral canal volume. The spinal cord is 50 % of the canal volume. But if assessed precisely in the vertebrae with a prominent glycogen body - the spinal cord volume takes 52 %, and the remaining 45 % is a CSF (see Table 3.2). 52 % of the glycogen body contained in the S1 vertebrae, and the remaining part of the glycogen body is in the L4 (37 %) and the S2 (11 %). In total, the 50 % of the lumbosacral spinal canal space the CSF fills. However, the S1 vertebra that contains 52 % of the total volume of glycogen body equals to 13 mm³ is filled with the cerebrospinal fluid for 45 % (11.5 mm³), which is less than the average fluid volume measured

within the lumbosacral spinal canal. In the maximum-volume vertebral segment L4 ($11.8\,\text{mm}^3$), the fluid is also not the predominant volume, $39\,\%$ ($10.8\,\text{mm}^3$). In the L4 vertebrae, the spinal cord occupies $11.8\,\text{mm}^3$ ($46\,\%$), which is almost as much in volume as it takes up by the cerebrospinal fluid.
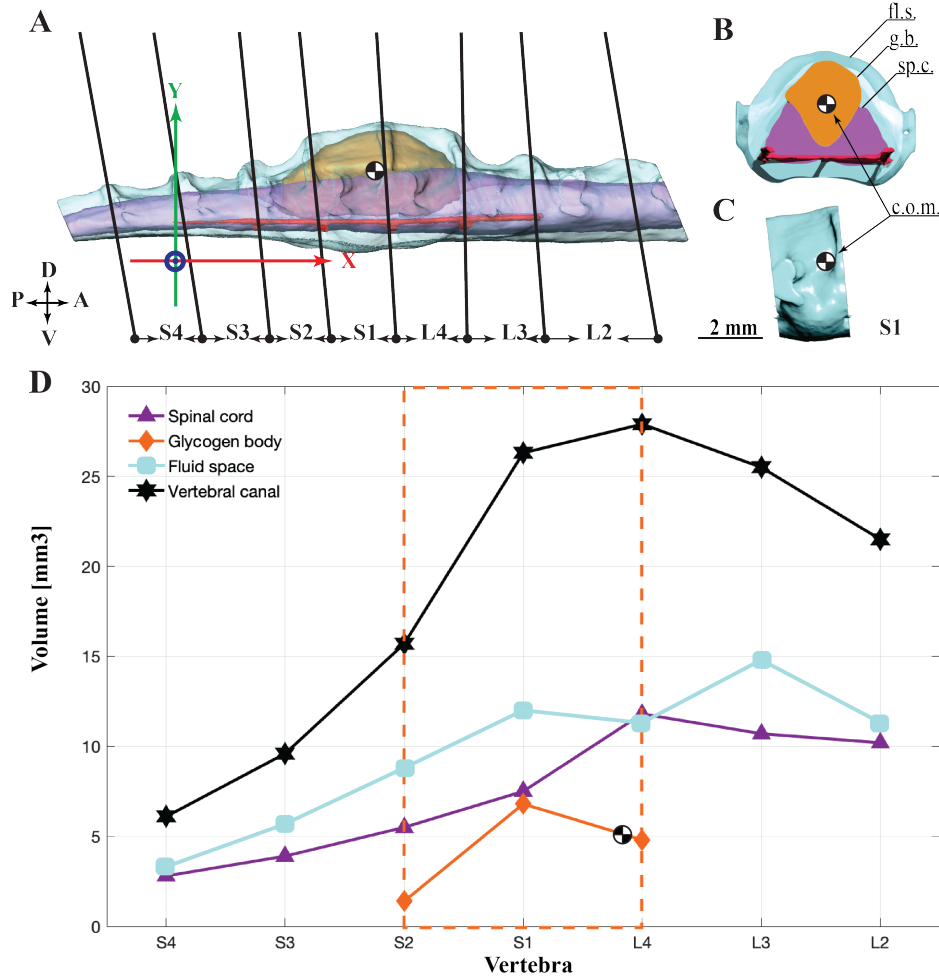
Figure 3.9: Volume measurements by spinal canal segments (modified from Kamska, Daley, et al., 2020). (A) Right lateral view at the 3D model of the spinal cord, the glycogen body, and the CSF surrounding both. Cuts are placed along the anatomical fusion zone, thus they are slightly tilted. The coordinate system's origin is placed between the geometric center of both femur head sockets, with the x-axis aligned in parallel with the denticulate ligament. The horizontal distance (x-axis) between the glycogen body's center of mass and the femur head (coordinate system center) is $6.2\,\text{mm}$, and the radial distance is $6.8\,\text{mm}$. (B) Segment S1 of the spinal canal and its contents. C. Right lateral view at the isolated segment S1 of the spinal canal. E. Data points show the volume measurements per spinal canal segment. Orange dashed-line rectangular shows the glycogen body location region relative to the lumbosacral canal vertebral regions. See abbreviations in Table 1.

Using modern 3D morphometric tools, we were able to evaluate whether the enlarged spinal cord intumescence at the lumbosacral region (J. J. Baumel, 1993)

Table 3.3: The length of each vertebra and the glycogen body. The length measurements [mm] on the digital model along the x-axis at the lateral longitudinal denticulate ligaments level.

	S4	S3	S2	S1	L4	L3	L2	GB
Length x-direction [mm]	2.2	2.3	1.9	2.2	2.4	2.2	3.1	5.2

is caused by the glycogen body rather than by increasing the neural tissue size (Imhof, 1904; Necker, 2005). It seems that the spinal cord's dorsal and lateral sides are modifications aimed at providing a steady-state balance at the time of its hypothesized oscillations. We analyze the spinal canal volume to quantify its enlargement associated with the avian unique spinal cord shape. As we are studying only part of the spinal canal, we evaluated the ratio of lumbosacral tissue volumes segmentally. We measured the length of each of the seven vertebrae along from L2 to S4 the x-axis on the lateral longitudinal ligaments level (see Figure 3.9 A, Table 3.3). Similar to the geometric measurement results, spinal cord volume decreases from the anterior to the posterior part of the spinal cord, from $2.8\,\text{mm}^3$ at S4 to $10.2\,\text{mm}^3$ at L2. However, the maximal segmental volume of the spinal cord is at the glycogen body location inside the L4 vertebra with a volume of $11.8\,\text{mm}^3$. Considering that L4 is not the longest vertebra from the lumbosacral canal, we can assume that the spinal cord enlargement is caused not only by a change in the shape of the hemispheres around the glycogen body holding area. We can assume the additional enlargement is also related to segmentally protruding accessory lobes out of the lateral edge of the spinal cord. Stanchak, Miller, et al., 2022 established the accessory lobes contain glycinergic neurons that laterally extend to the central canal through the spinal cord. To check whether the volume of the accessory lobes is related to the segment of the spinal protrusion, in Chapter 4, we measured and analyzed the chicken accessory lobes.

3.2.3   Buoyancy Forces Acting on Fluid-submerged Glycogen Body

The set of connective tissue inside the spinal canal that includes cerebrospinal fluid, meninges, and denticulate ligaments supports and cushions the weight of the neural soft tissue (Loth et al., 2001; Orosz and Bradshaw, 2007; Polak-Kraśna et al., 2019; Ramo et al., 2018; Schroeder and Murray, 1987; Simon and Iliff, 2016). However, the spinal cord inside the avian lumbosacral canal is loaded with extra mass added by the high-density glycogen body. Based on the glycogen body morphometry we have extracted from the quail LSO 3D model (see Table 3.2) and the literature observation on the glycogen density (see Table 3.1), we estimated a normal force applying by the glycogen body at the ventrally supporting spinal cord and denticulate ligaments. Following the Equation (3.3), we estimated a normal force produced by the glycogen body:

$$N, \text{eff} = 13 \times 10^{-9}\,\text{m}^3 \cdot 1.40 \times 10^3\,\text{kg/m}^3 \cdot 9.81\,\text{m/s}^2 = 51 \times 10^{-6}\,\text{N} = 51\,\text{µN}$$

The spinal cord stability relies not only on the buoyancy force since the specific gravity (SG = 1.04) is a bit higher than the CSF. We estimated the normal force produced by the spinal cord within the vertebral segments where the glycogen body is prominent - between L2, L1, and S4 vertebrae of the spinal cord ($\sum V_{\mathrm{L2,L1,S4}} = 24.8 \times 10^{-9}\,\mathrm{m}^3$). Following the Equation (3.3), the spinal cord's segments create a normal force of $F_{\mathrm{N,eff}} = 10\,\mathrm{\mu N}$. Thus, the normal force generated by the glycogen body is increased by the spinal cord and acts directly upon the dentate ligament network with 61 μN.

3.2.4   Denticulate Ligament Network Topology

The left and right lateral and ventral longitudinal ligaments, segmentally crossed by the ventral transverse ligaments (Schroeder and Murray, 1987; Streeter, 1904), form a hammock-like network of denticulate ligaments. At the S1–L4 vertebral fusion, where the glycogen body height and the vertical fluid space are maximal (see Figure 3.7 G-GH and Figure 3.8 I-F), an angle between longitudinal and transverse ventral ligaments is close to perpendicular, 84° (see Table 3.4 and Figure 3.10A and B). In the adjacent segments, the intersection angles are centered toward the glycogen body center of mass (see Figure 3.10).   The
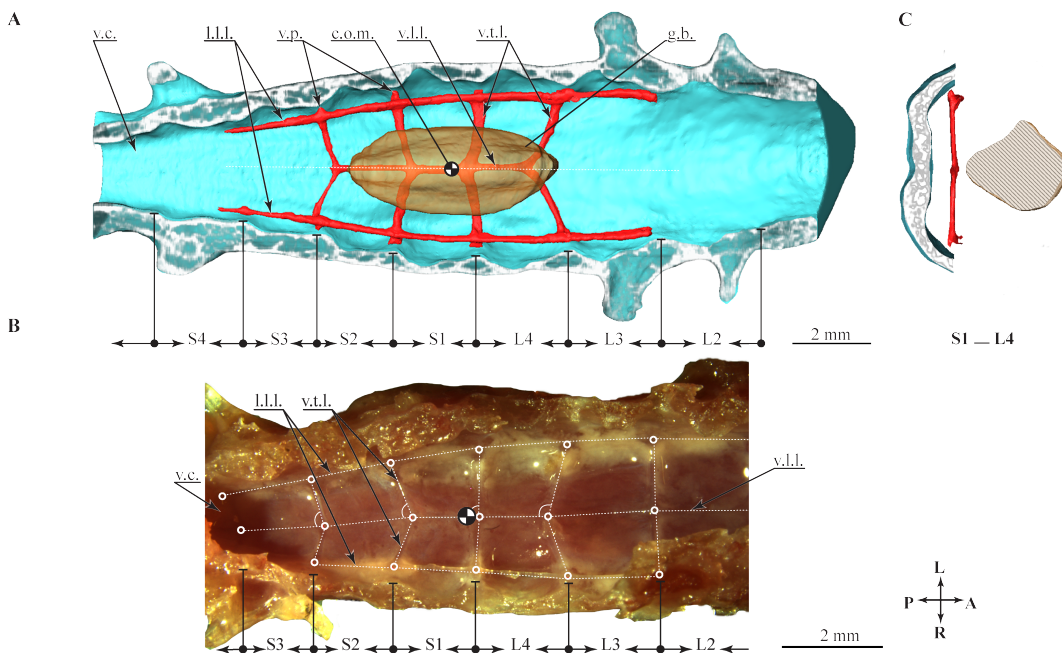
Figure 3.10: Denticulate ligament network topology (from Kamska, Daley, et al., 2020). (A) Digitally opened lumbosacral spinal canal from the dorsal side. The glycogen body is illustrated as a semi-transparent for evaluation anatomic topography. (B) Classically dissected spinal canal, else identical to A. (C) Transverse section through the spinal canal at the S1-L4 fusion region. See abbreviations in Table 1.

angle between the ventral longitudinal and transverse ligaments at the S2-S1 vertebral fusion is 71° and 98° at the L4-L3. Additionally, the μCT data (27 μm

Table 3.4: Intersection angles of transverse and longitudinal ligaments.
Numbers are mean (SD) angles over measurements on three classically dissected
lumbosacral samples of a common quail (see Figure 3.10).

S3-S2	S2-S1	S1-L4	L4-L3	L3-L2
72(5)°	71(6)°	84(4)°	98(7)°	92(10)°

voxel edge) discovered that the denticulate ligament network thickness is not
homogeneous.   The thickness of the lateral longitudinal ligaments varies from 3
to 6 voxels. In comparison, the birds' unique ligaments - ventral longitudinal
and transverse (Schroeder and Murray, 1987) are slimmer about two times (from
1 to 2 voxels). The discovered variations in the ligaments' thickness suggest the
network possesses an anisotropic stiffness that can be functionally related to the
soft tissue behavior inside the lumbosacral canal.

Digital dissection showed that the network is thickened at the intersections of
the ligaments. Classic stereomicroscopic dissection suggests that the thickenings
look like nodes (see Figure 3.10 B). At the intersections of the transverse and
lateral longitudinal ligaments, where we identified nodes, the literature has
described accessory lobes segmentally protruding from the spinal cord inside
the canal (Eide, 1996; Schroeder and Egar, 1990; Schroeder and Murray, 1987).
The 3D model of the denticulate ligaments contains parts of ventral processes,
also called the "robust feet" (Schroeder and Murray, 1987) extrude from the
lateral intersection nodes toward the ventrolateral sides of the spinal canal (see
Figure 3.10 C). The open field of the stereomicroscope allowed us to pull the
ligament with forceps away from the ventral side of the canal and observe the
ventral processes attached at the vertebral fusion (see Figure 3.11).

3.2.5   Biomechanical Properties of LSO Features

The qualitative evaluation of the denticulate ligaments stretching using forceps
showed that the ligaments did not rupture even when we pulled them more
than the maximally allowed spinal canal space (see Figure 3.11). We calculated
denticulate ligament strains by combining the digital dissection data on the fluid
space morphology and the classical dissection data on the length and topology
of the ligaments. Following the maximum possible dorsal and ventral position
of the neural soft tissue inside the lumbosacral spinal canal (see Table 3.5), we
revealed that the strain overall measured transverse ligaments of 5 % at the soft
tissue upward deformation, and 2 % for downward deformation. The maximum
downward deformation, the highest strain, is in transverse ligaments arranged
at the L4-S3 (5 %) fusion exactly where the ventral space below the spinal cord
is maximal (see Figure 3.12). The highest upward strain in S2-S3 (8 % does
not correspond with the maximum available vertical space between the neural
soft tissue and the spinal canal dorsal. By analyzing the calculation results,
we have to consider that the soft tissue of the lumbosacral sample processed
with iodine solution shrunken (Vickerton et al., 2013). Thus, unlike the ventral
edge of the soft tissue, whose relative level is determined by the network of
ligaments attached to the canal along the coronal plane, the dorsal edge of
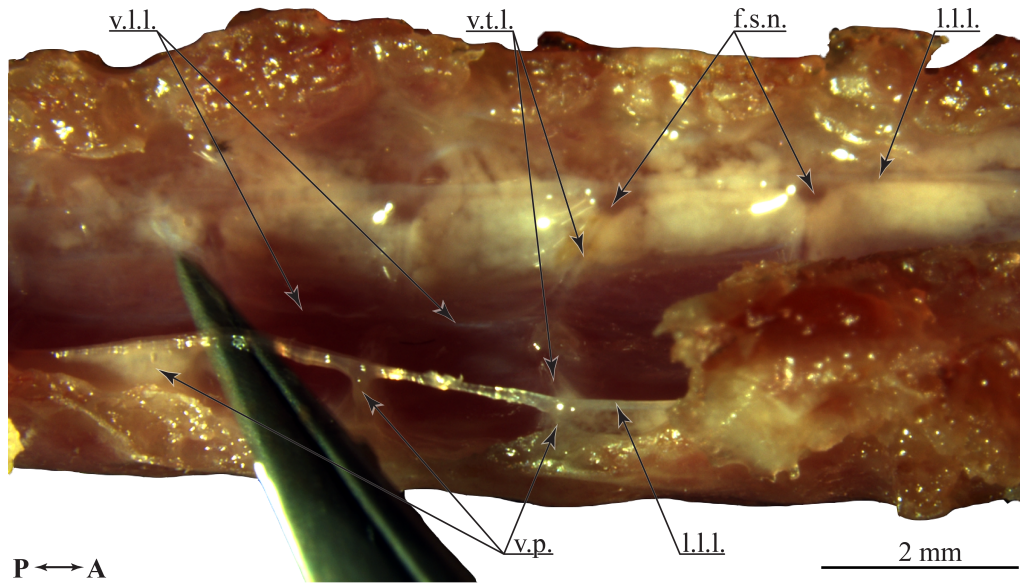
Figure 3.11: Denticulate ligament network attachment to the spinal canal (from Kamska, Daley, et al., 2020). An oblique view of the classically dissected quail's lumbosacral spinal canal, opened from the dorsal side, shows the network of dentate ligaments after the removal of the spinal cord and glycogen body from its surface. The right lateral longitudinal ligament raised with forceps demonstrates its elasticity and its attachment site to the spinal canal via the ventral process at the vertebral fusion region. See abbreviations in Table 1.

the soft tissue was most likely reduced toward the ventral side of the canal. Thus, the dorsal space increase potentially resulted in an overestimation of the maximum potential upward movement of the soft tissue.

The denticulate ligaments are involved in the spinal cord movement under physiological load (Polak-Kraśna et al., 2019). Depending on the canal features, the spinal cord mobility degree varies. For example, birds have suspensory ligaments (J. Baumel, 1985) that release a spinal cord from any tension in the brachial plexus region by diverting tensile forces from the plexus roots (Orosz and Bradshaw, 2007). The lumbosacral region contains no suspensory ligaments (Schroeder and Murray, 1987), whereas the canal morphology modification, the glycogen body presence, and the denticulate ligament topology are likely to

Table 3.5: Calculation of transverse ligaments strain. Strain calculation is virtual, in the range of maximum possible soft tissue vertical oscillations inside the lumbosacral canal.

	S3-S2	S2-S1	S1-L4	L4-L3
Dorsal fluid space (up) [mm]	0.48	0.37	0.41	0.56
Ventral fluid space (down) [mm]	0.19	0.33	0.52	0.19
Transverse ligament length $\bar{L}$, at rest [mm]	1.21	1.51	1.61	1.67
Transverse ligament length $l_{up,virt}$ stretched [mm]	1.30	1.55	1.66	1.77
Transverse ligament length $\bar{l}_{down,virt}$ stretched [mm]	1.23	1.54	1.69	1.68
Nominal strain up $\bar{e}_{up}$ [%]	7.9	3.0	3.2	5.8
Nominal strain down $\bar{e}_{down}$ [%]	1.3	2.4	5.2	0.7

enhance spinal cord movements.
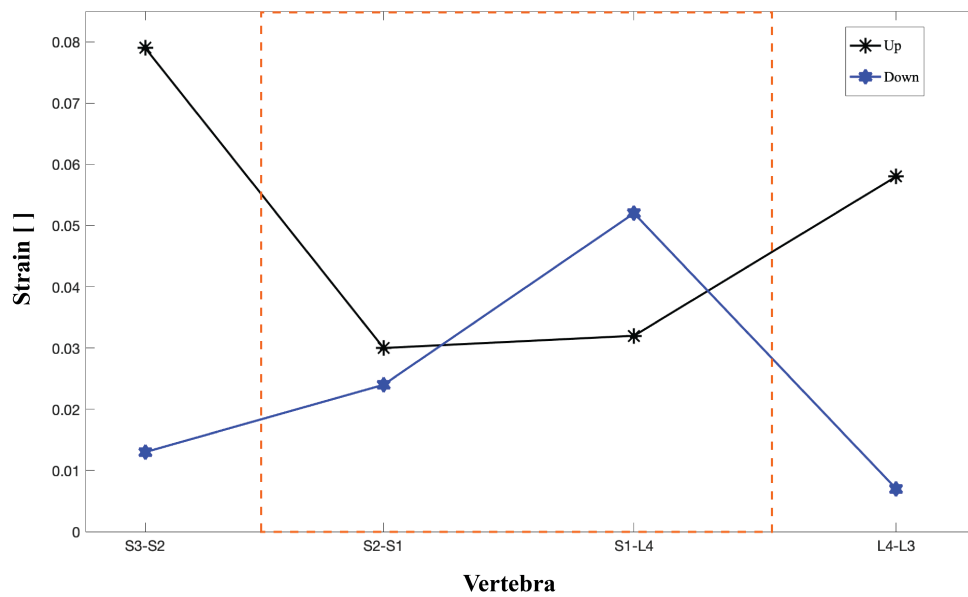
Figure 3.12: Maximum deformation of transverse ligaments toward the dorsal-ventral canal sides (from Kamska, Daley, et al., 2020). The ligaments' strain is calculated according to the maximum glycogen body dorsal and spinal cord ventral positions. Asterisk markers (black line) show the maximal transverse ligament strain at the dorsal position, and the blue line with hexagram markers the ventral position strain. Orange dashed-line rectangular shows the glycogen body location region relative to the lumbosacral canal vertebral regions.

3.3 Conclusions

Based on the topographical anatomy and 3D morphometrical analysis, and biomechanical properties estimation, we updated the hypothesis on the mechanosensing function of birds' lumbosacral region. The digital dissection of the common quail lumbosacral region combined with the stereomicroscope dissection allowed us to extract the morphological data on the bone, soft and connective tissue. We revealed that the location of the high-density glycogen body corresponds to the maximum fluid space around the soft tissue inside the lumbosacral canal. The predominance of the ventral fluid space over the dorsal one, excluding the transverse grooves, can suggest potential oscillations are asymmetrical. The transverse semi-circular grooves may function as canals for relieving the cerebrospinal fluid flowing around moving lumbosacral soft tissue. Simplified calculations have shown that collectively the glycogen body, spinal cord, and denticulate ligament network surrounded by cerebrospinal fluid inside the narrow but segmentally dilated spinal canal potentially responds with oscillations to external acceleration induced by locomotion. Combined, all the LSO distinctive anatomical features potentially functionally related to the putative mechanism of strain-based sensitivity suggest that the lumbosacral organ is more consistent with accelerometer function. However, we can not exclude that the LSO sensing is associated with ligaments strain-biased- and fluid flow pressure excitation mechanisms of mechanosensing neurons in the accessory lobes.

Chapter 4

Functional Soft Tissue Motion in the Avian LSO

Topic

In this project, the fundamental question concerns the ability of the spinal cord to move inside the avian lumbosacral canal, with consideration of the influence of adjacent anatomical structures.

Motivation

The morphological and biomechanical properties of the unique lumbosacral anatomical structures we have established in Chapter 3. The usage of digital and classical dissection methods indicates that the lumbosacral specializations collectively resemble a fluid-filled mass-spring-damper system. An overly developed fluid space around the soft tissue suggests the possibility of its mobility inside the lumbosacral canal. The soft tissue, supported by the hammock-like denticulate ligament network, potentially oscillates under the external acceleration caused by avian locomotion. We aim to test our hypothesis that soft tissue is movable inside the spinal canal. We also hypothesize that the mobility of the soft tissue is affected by the dentate ligaments and varies depending on the amount of acceleration induced by the bird's locomotion. The accessory lobes with potential mechanosensory function segmentally protrude from the spinal cord hemispheres into the spinal canal. The accessory lobes are intimately close to the denticulate ligaments and approximately coincide with the bony transverse grooves on the dorsal side of the canal. Due to such topographic anatomy, the accessory lobes presumably are stimulated through the denticulate ligaments stretching and/or cerebrospinal fluid flow. However, no studies have tested whether the soft tissue is movable within the lumbosacral canal. Identifying *in vivo* soft tissue behavior inside the lumbosacral canal at the locomotion is a non-trivial task. The capabilities of currently available functional imaging technologies are still limited and cannot directly visualize the behavior of small-sized neural tissue embedded inside highly pneumatized bones of the fused lumbosacral vertebrae covered with multilayered tissue. In this project, to explore the soft tissue mobility directly inside the avian lumbosacral canal instead of *in vivo*, we developed a new *in situ* method. We digitally dissected the LSO region of avian cadavers in various orientations. Alteration of gravity orientation to the LSO sample revealed minor

changes in the neural soft tissue position inside the canal. Additionally, our adaptation of the traditional diceCT protocol allowed us to study the denticulate ligament network's topological features and suggest their potential impact on soft tissue mobility. Using a simplified biophysical LSO model, we tested our hypothesis that soft tissue mobility depends on the dentate ligament network and on the amount of external acceleration induced by avian locomotion.

Synopsis

There are several hypotheses related to the mechanosensory function of the putative lumbosacral organ. We assume that the LSO, likewise a fluid-filled mass-spring-damper system, is sensitive to acceleration. The neural soft tissue embedded inside the expanded spinal canal supported by the denticulate ligament network could become entrained by external accelerations. Mechanoreceptive accessory lobes potentially percept ligament stretching and cerebrospinal fluid flow around the soft tissue and directly transmit sensor information to the central neural system. Studies about the mobility of the neural soft tissue inside the avian holistic lumbosacral canal are absent. We explored the soft tissue mobility directly inside the avian lumbosacral region by facilitating *in situ* digital dissection method. We developed and tested protocols for MRI and μCT imaging facilities to find the sample processing approach causes minimal influence on soft tissue behavior. Our novel approach for *in situ* digital dissections of the LSO allowed us to identify the soft tissue's static deflection and observe fine structures of the denticulate ligament network adjacent to the spinal cord. The biophysical LSO model developed based on the 3D anatomical observation allowed us to test our hypothesis that soft tissue mobility is limited by ligaments' pre-tension and depends on acceleration.

4.1 Materials and Methods

In vivo visualization of the soft tissue response to external acceleration directly within the avian lumbosacral canal has not yet been available. Instead, we approached *in situ* techniques as an alternative. However, the *in situ* visualization techniques also come with their limitations. Measurements of the soft tissue movements inside the lumbosacral canal are currently available only under static loading conditions using cadaver samples. To get contrast images for the soft tissue, we worked on modifying already existing protocols for magnetic resonance imaging (MRI) and micro-computed tomography (μCT) imaging facilities. Biomechanical simulation using a qualitatively replicated LSO model allowed us to study the soft tissue behavior in its dynamic state and check the effect of the denticulate ligament network topology on soft tissue mobility and its sensitivity to acceleration.

4.1.1 Digital *in situ* Dissection

For measuring soft tissue static deflection within the spinal canal, we approached the *in situ* techniques that require preliminary sample treatment with chemical solutions that affect the shape and size of the soft tissue (Gignac, Kley, et al., 2016; Jonmarker et al., 2006; Vickerton et al., 2013). Depending on the extent,
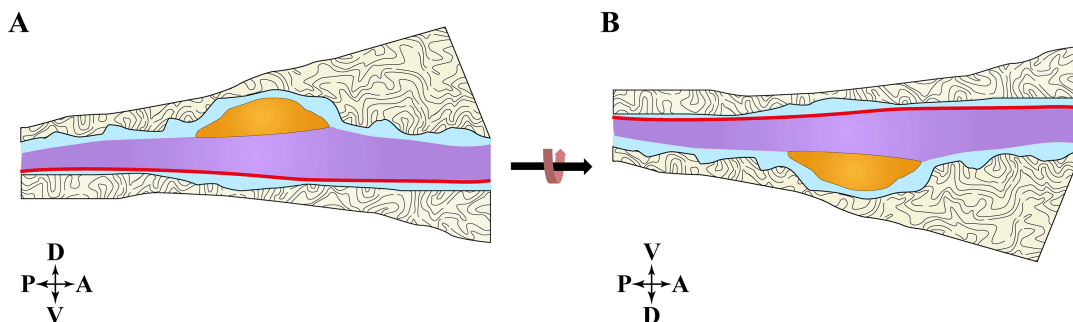
Figure 4.1: Schematic illustration of LSO scanning for *in situ* measurement of soft tissue static deflection. For visualization of the lumbosacral soft tissue deflection under static acceleration, the same sample was 3D imaging in its (A) standard and (B) inverted orientations.

shrinkage of the tissues can affect the accuracy of measurements (Jonmarker et al., 2006; Noguchi et al., 2000) of the relative position of the soft tissue within the spinal canal. We tested different chemical solutions to find one that would cost minimal shrinkage to a processing sample but allow us to reach the highest possible image contrast and resolution. We were working on modifications for MRI and (μCT) protocols. Our more successful protocol for MRI allowed visualizing fine soft tissue structures by avoiding using fixation and contrast-enchanting steps of chemical treatment. But the most optimal technique for studying the soft tissue movements directly inside the canal we succeeded in developing for the μCT facility. Our modifications of the traditional diffusible iodine-based contrast-enhanced computed tomography (diceCT) protocol allowed us to observe new morphological details of the denticulate ligaments network.

Details about the protocols are explained in the following paragraph. To study whether the soft tissue deflects inside the spinal canal under static acceleration, we digitally dissected the lumbosacral regions of cadaver chicken samples in standard and inverted orientations (see Figure 4.1). The chemically treated sample of the lumbosacral region we scanned with MRI immediately after the fixation step. And then, the same sample we stained with an iodine-based solution and scanned with μCT. The chemically-free treated sample was scanned only with MRI.

Sample Processing for Scanning

In total, we obtained four young female chicken cadavers (*Gallus gallus domesticus*) (Linnaeus, 1758) as cooled carcasses from commercial breeder Frischemarkt Bleyer GmbH. We used two samples to test soft tissue reaction on the fixative solutions and two to scan the lumbosacral region processed with and without chemical treatment. The birds' age varied between 35 and 40 days; average body weight was (1110 ± 21) g; the body size varied between 15 and 20 cm. The birds were all slain 36 hours before the dissection. At the first stage of sample processing - we dissected both carcasses according to the practice written by Gurtovoy et al., 1992. We cut off the pelvic bones before isolating the lumbosacral vertebrae from the thoracic and caudal vertebrae. For mounting the sample inside the vessel (20 mm in diameter), we truncated protruding vertebral processes.

Tissue Reaction on the Fixative Solutions

The tissue fixation step precedes its contrast-enhancement staining step (Gignac, Kley, et al., 2016). There is no ideal universal fixative solution (Gignac, Kley, et al., 2016) that equally preserves the fine structures of cellular organelles of the different tissue types (Eltoum et al., 2001; Nowacek and Kiernan, 2010). To maximize the quality of sample scans, we have to consider tissue types and test the shrinkage reaction (Metscher, 2009b; Vickerton et al., 2013). The spinal cord tissue mainly contains a high concentration of lipid molecules (Bruce et al., 2017). Because the lipids are soluble in alcohol (Jeffery et al., 1989), the alcohol concentration has to be minimized in both fixative and staining solutions (Gignac, Kley, et al., 2016). To choose a fixative solution that would cause minimal neural soft tissue shrinkage, we tested their reaction on 10 % neutral buffered formalin (NBF) and 4 % formalin on chicken samples (see Figure 4.2). We opened the lumbosacral canal of two samples and examined the reaction of the glycogen body and spinal cord to both fixative solutions. We chose NBF 10 % to fix the samples, which caused a rapid shrinkage reaction, but only for the first few minutes. Formalin 4 % did not cause a fast reaction, but shrinkage continued even after 40 minutes; we could observe the process of the soft tissue separating from the pia mater.
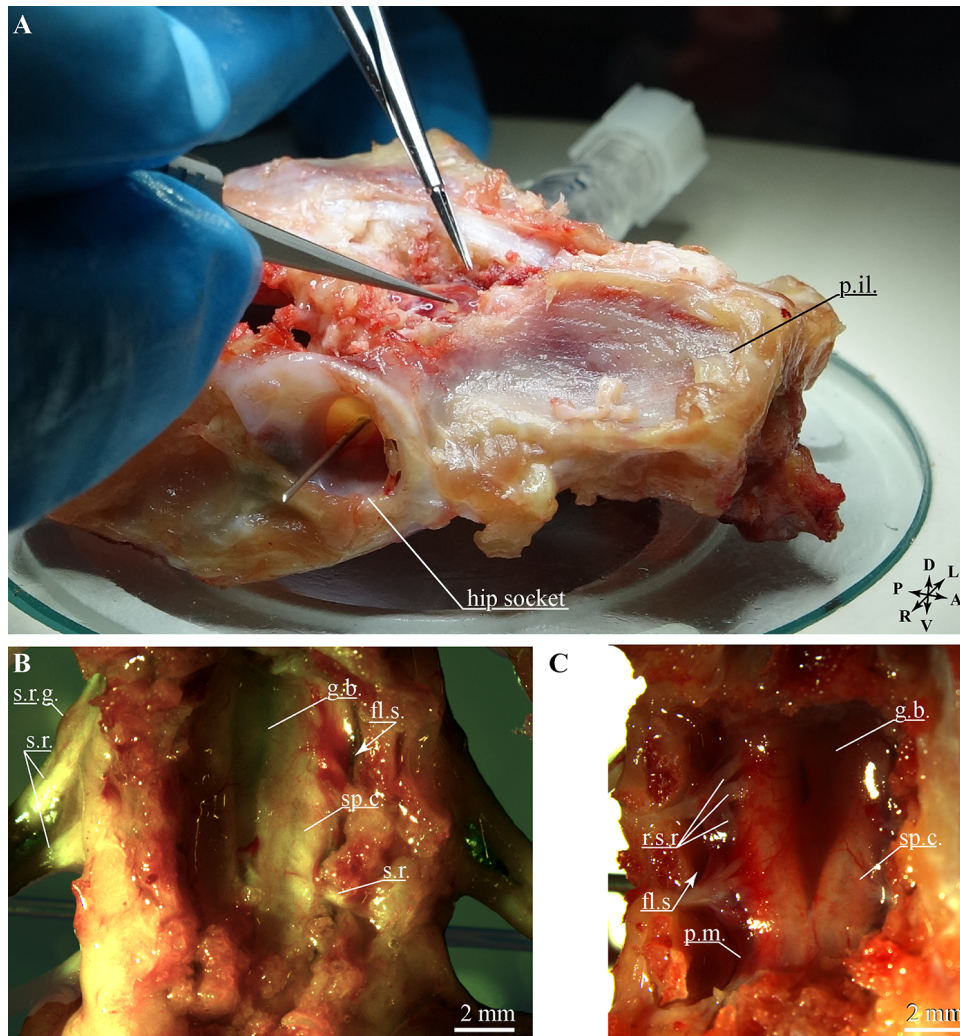
Figure 4.2: Testing of soft tissue reaction to fixing solutions (A) Synsacrums of cooled fresh chicken cadaver opened from the dorsal side were used to test soft tissue reaction on two types of fixative solutions. (B) 10 % NBF solution resulted in instantaneous but not intensive shrinkage, which stopped within a few minutes; (C) 4 % formalin resulted in the superficial but intensive neural tissue shrinkage lasting 40 minutes. See abbreviations in Table 1.

Sample Processing with Chemical Treatment

Our previous experiences in fixation and contrast-enhancing sample processing have revealed that chemical solutions diffusion through the spinal canal to the deep inside embedded lumbosacral soft tissue is inhibited. To enable the chemical solution to achieve the soft tissue effectively fast - we modified the traditional diceCT protocol. We opened inlets through the bone tissue to the spinal canal mechanically. We opened the solutions inlet without compromising the integrity of the soft tissue by using burr (tip diameter 0.9 mm) and trephine (1.8 mm), and micro curettes (tip diameter 1 mm and 1.5 mm) under the stereomicroscope (ZEISS Stemi 305 Trinocular Stereo Microscope). We immersed a freshly isolated chicken lumbosacral sample in an ice bath to slow down soft tissue autolysis and maintain internal homeostasis by suppressing dehydration processes (see
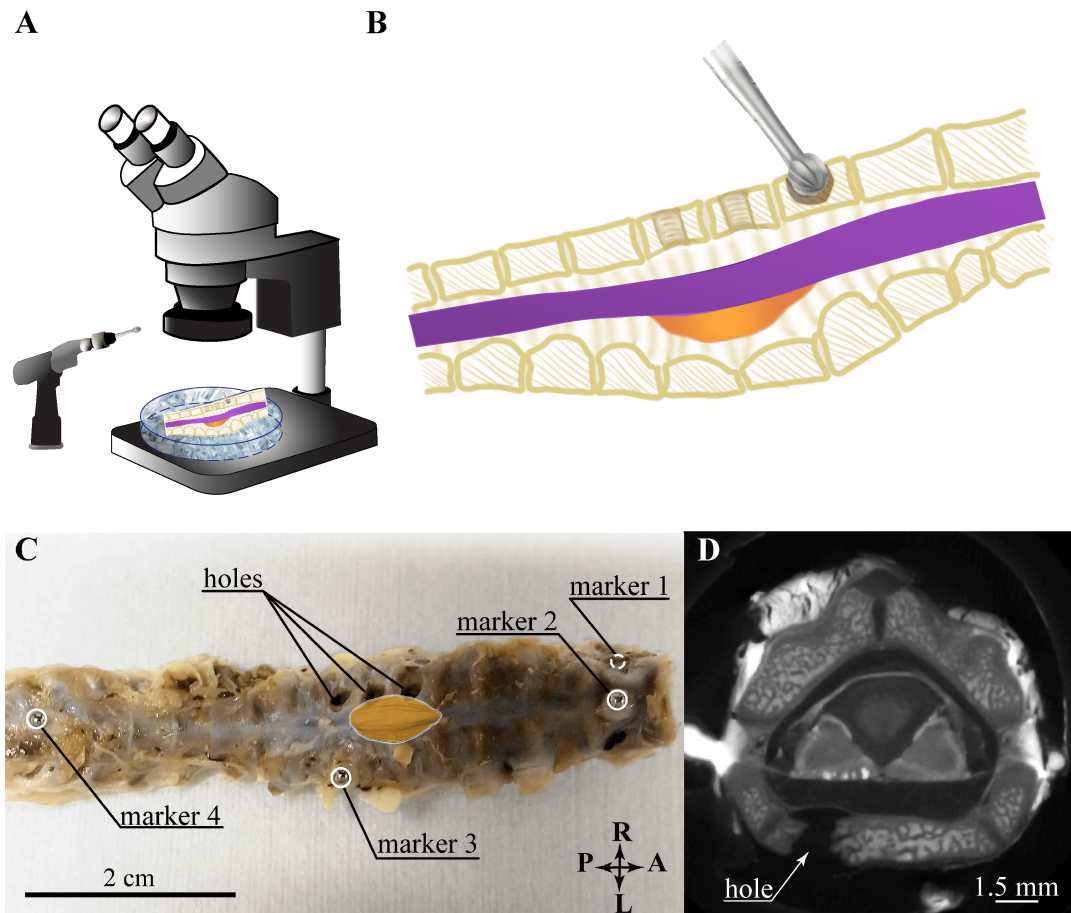
Figure 4.3: Details on our innovative step in the diceCT sample processing technique. (A) Freshly isolated lumbosacral sample immersed in an ice bath prepared for a mechanical process of drilling under the stereomicroscope. (B) Zooming in on the sample shows that the drilling processing opens the inlet through the bone tissue without compromising the integrity of the soft tissue. (C) A ventral view of the processed sample shows the locations of the inlets and, attached to the bone surface, the steel marker beads relative to the glycogen body location. (D) A transverse cross-section through the lumbosacral canal at its maximum height at the inlet area demonstrates the quality of μCT data. Our updating for the diceCT resulted in those fixative and staining solutions treating the soft and connective tissue. The inlet area on the cross-section demonstrates an absence of any neural soft tissue deformation caused by the mechanical processing step.

Figure 4.3). After drilling holes through the spinal canal's ventral wall, we fixed the lumbosacral sample with neutral-buffered formalin 10 % for nine days. We then fixed the MRI scan specimen with a 2.30 mm-thick silicone insert (Ecoflex 00-10) inside the 20 ml vesicle immediately filled with fresh fixative solution. For the μCT, the same sample was fixed in 10 % neutral-buffered formalin for three months, then transferred for 65 hours into a 4 % Lugol's iodine solution prepared according to the method described in Hitchins et al., 1998. We transferred the stained sample from the Lugol's solution to the running tap water. With a 20 ml syringe, we gently pump tap water through the holes in the vertebrae to replace iodine solution out of the canal for the termination of a staining process. In 20

minutes, the sample was immersed in neutral-buffered formalin 10 % solution. For the further step of the inverted 3D model alignment with the standard oriented model of the lumbosacral organ, three steel balls 1.5 mm in diameter were glued directly to the bone surface of the sample. The sample was fixed inside a 20 ml vesicle in an identical method to the one used for MRI scans.

Sample Processing without Chemical Treatment

We dissected another chicken cadaver for imaging LSO using the MRI protocol developed for samples processed without fixative and staining samples. We cut off the anterior and posterior vertebrae from the lumbosacral region and immediately immersed the freshly isolated lumbosacral region in an isotonic saline solution. The LSO sample was tightly fixed inside a 20 ml syringe with a silicone liner (Ecoflex 00-10). We used the syringe instead of a conical tube with a cap to remove all air bubbles from the surrounding sample saline solution. The remaining air bubbles were squeezed out of the syringe with a piston to minimize susceptibility artifacts during MRI scanning.

4.1.2   Sample Scanning

Magnetic Resonance Imaging

Magnetic resonance imaging was acquired with a 14.1 Tesla horizontal magnet (Magnex Scientific, Oxford, UK), equipped with a gradient system with a maximum strength of 1 T/m (Resonance Research Inc., Billerica, Ma) and an inner diameter of 12 cm, interfaced to a Bruker Avance III console (Bruker Biospin, Ettlingen, Germany). Vesicles with samples were placed inside a homebuilt 2-cm volume coil and oriented inside the coil to align the lumbosacral region in standard and inverted orientations relative to the scanner coordinate system.

Micro-Computed Tomography

We scanned the chicken lumbosacral region in standard and inverted orientations to studying if the soft tissue moves inside the lumbosacral canal. For scanning, we used Metris X-tek custom 190 kV bay system without filters (Manchester X-ray Imaging Facility). Processed sample of the chicken lumbosacral region with on the bone surface attached still beads markers we tightly fixed with a silicone liner (Ecoflex 00-10) inside a conical tube filled with fresh 10 % NBF fixative solution. Then the tube with the sample was mounted on the horizontal holder and installed inside the scanning chamber. We scanned the tube with the sample in its standard and horizontal orientations. An angle of inclination of the coronal plane of the standard orientated sample relative to the horizontal rotational stage deviated by 7 degrees, and the inverted orientation deviated by 3 degrees. The sample scanned in the inverted orientation has an angle of inclination of the coronal plane relative to the rotational stage different by 10 degrees from the coronal plane of the sample scanned in the standard orientation. The voxel size of the isotropic μCT image stack was 39 μm. After back-projection,

generated 796 images (TIFF format, bright signal against a black background), each is 1000 x 1000 pixels.

To study the topographic anatomy of the lumbosacral structures in 3D, we scanned the same LSO sample with a Metris X-tek custom 160 kV bay system without filters (Manchester X-ray Imaging Facility) but in a vertical orientation. The tube with the LSO sample mounted inside was vertically installed inside the scanning chamber. During the whole process of micro-CT scanning with the sample rotation inside the scanner chamber, the X-rays emitted by the X-ray generator passed through the sample with relatively the same thickness. The voxel size of the original isotropic image stack was 40 µm, and after back-projection, were generated 994 images (TIFF format, bright signal against a black background), each is 1000 x 1000 pixels.

4.1.3   3D Segmentation

To evaluate protocols we developed for imaging the relative position of the soft tissue inside the lumbosacral canal, we segmented in 3D anatomical structures based on both MRI and µCT data. We chose that imaging protocol that allows us to reach consistency in 3D models' volume and shape segmented based on standard and inverted orientations scans of the same lumbosacral sample. MRI data of both samples were processed with and without chemical treatment, and the µCT data we segmented in 3D using Amira (versions 6.5.0 and 2020.02).

3D Segmentation of MRI Data

MRI data of both samples processed with (see Figure 4.13 A, B) and without chemical treatment were segmented using a manual selection tool. We applied the interpolation function between two to three segmented slices and constantly switched working planes. MRI data on sample fixed with 10 % NBF and kept in the same fixative solution during the scanning process allowed to segment a glycogen body, a spinal cord, and a cerebrospinal fluid (CSF) space. MRI data on the chemical-free processed sample allowed observation and segment not only a glycogen body, spinal cord, and CSF space but fine structures: accessory lobes and some parts of longitudinal ligaments with intersection nodes on CSF space.

3D Segmentation of Micro-CT Data

The quality of the µCT data allowed us to segment in 3D a cerebrospinal fluid space, a spinal cord, a glycogen body, and steel markers using a semi-automatic approach using a threshold function; segmented structures were interpolated between two to five segmented slices. Denticulate ligaments and accessory lobes we segmented manually on every second to the third slice using the interpolation function; working planes were switched as needed depending on the shape of the fine structures.

3D Surfaces Generation

Surfaces of each anatomical structure segmented on the MRI and the μCT data we rendered with the "SurfaceGen" module and afterward saved as individual Label Field Amira Mesh [AM] files (Ruthensteiner and Heß, 2008). For studying the soft tissue deflection, we pre-aligned a cloud of anatomical models' surfaces generated based on the inverted scan to a cloud of surfaces generated based on the standard scan. We conducted the pre-alignment step using Amira (version 2020.02), but for fine alignment, we approached an additional software. For this aim, we exported the surfaces of each anatomical structure as an individual object [OBJ] file. For studying the topographic anatomy of the LSO, we reduced the number of triangles on each surface using Autodesk Maya (version 2020). We exported the surfaces from Amira as standard triangle language [STL] files. Following Buchanan et al., 2014, I removed non-manifold edges, manually closed holes, and smoothed polygonal meshes.

4.1.4 Soft Tissue Deflection Measurements

For accurate measurement of soft tissue deflection, we decided to use 3D models generated based on lumbosacral sample scanned with μCT facility (see Figure 4.4). Preliminary alignment of the inverted models with the corresponding standard models based on CSF space anatomical features showed that the value of soft tissue static deflection is in the range close to the resolution of the scans. In addition, different bone densities and imaging system errors reduced the potential accuracy level achievable by aligning models based on CSF space anatomical features. The signal intensity of used MRI-compatible markers was low compared to markers used for the μCT scanning.
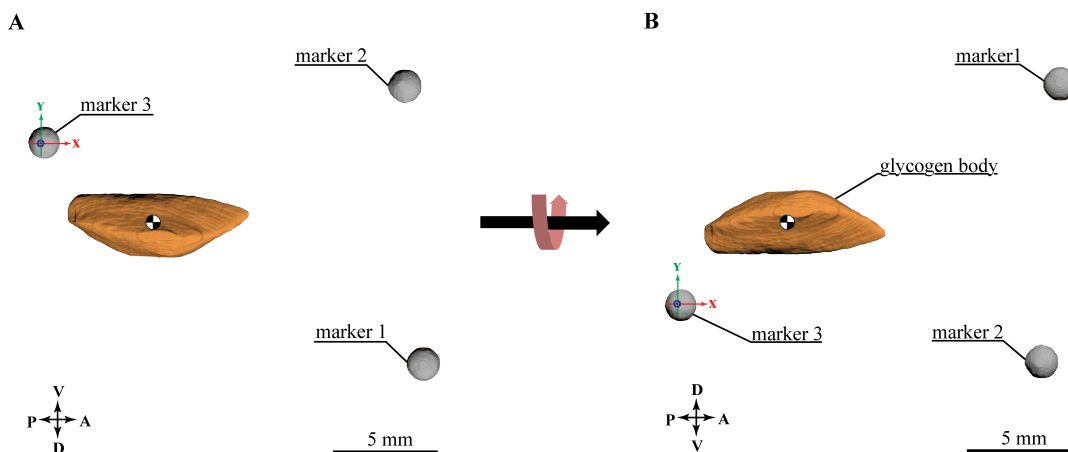
Figure 4.4: Alignment 3D models of the LSO scanned at inverted and standard orientations. The glycogen body and three markers were scanned in (A) down (inverted) and (B) up (standard) orientations, segmented as 3D models, and aligned by the steel markers' center of mass.

Determining the Coordinate Origin

We determined the origin of the coordinate system for the chicken lumbosacral organ based on the sample scanned with μCT in its standard orientation. The coordinate origin was determined by the intersection point of the sagittal, transverse, and lower coronal planes (see Figure 4.5). First, we adjusted the coronal plane according to the sites of ventral processes attachment to the spinal canal's left and right sides. These sites are the narrowest region of each vertebral canal segment formed at the junction of the vertebral body and pedicle. In Figure 4.5, these sites are indicated with yellow spheres. Second, we determined a sagittal plane. The sagittal plane's dorsal edge was adjusted to the highest points of each spinal canal segment, formed by neural arches fusion of adjacent vertebrae. In Figure 4.5, these sites are indicated with yellow spheres distributed along the spinal canal on its dorsal side. The ventral edge of the sagittal plane was adjusted to the segmental series of the midpoints between the left and right sites of ventral processes attachments to the spinal canal (see the left and right ventrolateral sides of the spinal canal indicated with yellow spheres Figure 4.5). The transverse plane was determined by rotating the sagittal plane 90 degrees. To establish a coordinate origin for the chicken LSO, we shifted the coronal plane down (see the lower coronal plane in Figure 4.5) to the level of the left and right acetabular sockets surrounding the femoral heads. The 3D model does not contain the pelvic girdle since it was cut off to make the sample fit the tube for scanning. Before the cutting-off step, we pinned a steel needle through the center of the right acetabular socket into the sacral vertebra to reference the femoral head location level.
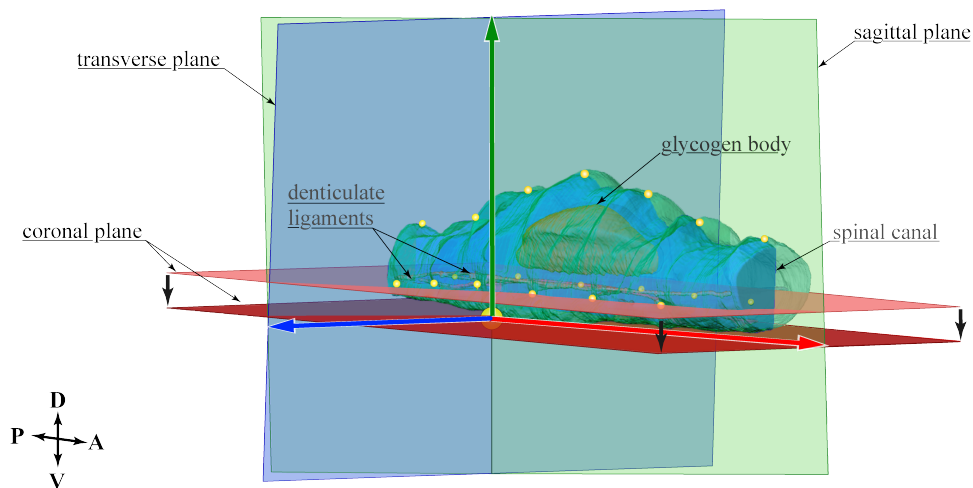
Figure 4.5: Determining the coordinate origin for the chicken LSO. Three intersected planes (x-red, y-green, z-blue) in a prominent yellow sphere show a local coordinate system. The sagittal and coronal planes are adjusted to the anatomical features of the chicken synsacrum. The lower coronal plane used to determine the coordinate origin is at the level of the acetabular sockets. The transverse plane is a 90-degree rotated sagittal plane.

3D Models Alignment and Analysis

Using *in situ* imaging technique, we studied if the LSO soft tissue is sensitive to static acceleration by tracking the glycogen body position inside the lumbosacral canal relative to the markers' cloud attached directly to the spine surface. Both 3D LSO models of the specimen scanned in standard and inverted orientation contain a set of three 1.5 mm markers we used to align models (see Figure 4.4). After the standard and inverted LSO models were aligned, we measured the distance between the center of mass of the glycogen body's 3D models. For
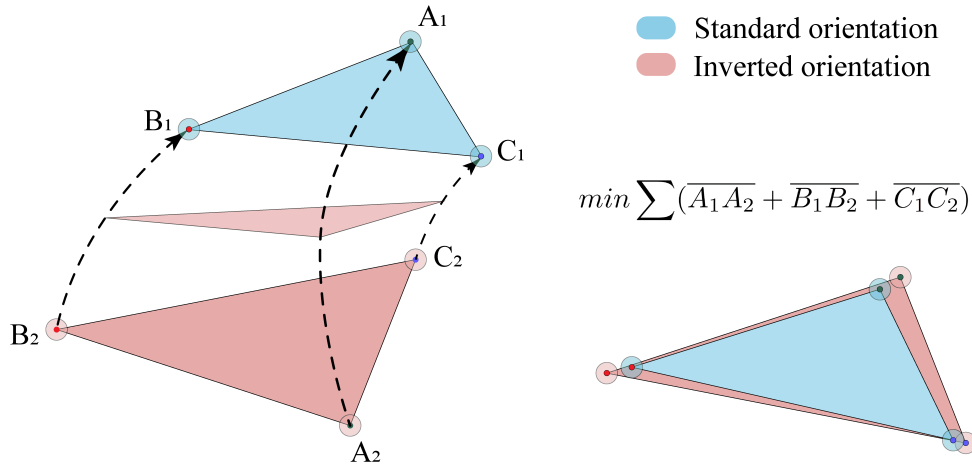
Figure 4.6: Illustration alignment of the inverted 3D model to the standard one. Three markers scanned in standard and inverted orientations constitute point clouds. Two-point clouds form triangles with unequal sides and angles. The iterative closest point (ICP) algorithm is employed to align two clouds by minimizing the sum of the difference between corresponding points of two clouds of points.

the fine alignment of the target 3D model (inverted) to the reference one (standard) by corresponding markers and measuring the soft tissue deflection by the distance between the center of masses of the target and reference glycogen bodies, the iterative closest point (ICP) algorithm (Besl and McKay, 1992) was approached. The algorithm's function was to minimize the distance between the two-point clouds formed by the markers. The coordinates of the center of mass of each marker and the glycogen body of both, pre-aligned in Amira (version 2020.02) 3D models, were extracted in Autodesk 3ds Max (version 2021). Given the coordinates of the three markers in both orientations, we applied the ICP algorithm in Matlab (version 2019b) to obtain the transformation matrix between the two 3D models (see Figure 4.6).

4.1.5 Biophysical Simulation

Biomechanical modeling and simulation techniques allow testing the structure-function relationship for anatomical structures (Hutchinson, 2012) that are not accessible for *in vivo* or *in situ* studies. The digital dissection of the chicken allowed us to observe the denticulate ligament network topological features that potentially influence soft tissue mobility. Particularly we segmented in 3D the medial ligaments extruding vertically from the horizontal part of the denticulate

ligament network to the ventral side of the canal. However, *in situ* imaging techniques do not allow us to test our hypothesis that the observed denticulate ligament topology affects soft tissue mobility. Therefore, we approached the LSO biophysical model to test our assumption that soft tissue mobility depends on acceleration and the denticulate ligament pretension (see Figure 4.7). The benefit of the biophysical simulation is the possibility of manipulating with parameters of individual anatomical structures. We have qualitatively reproduced the topology of the denticulate ligament network based on anatomical observations of digital dissection of the domestic chicken (*Gallus gallus domesticus*) digital dissection. We tested the pretension parameter of the ligaments as a limiting factor for soft tissue mobility through the static and dynamic simulation.
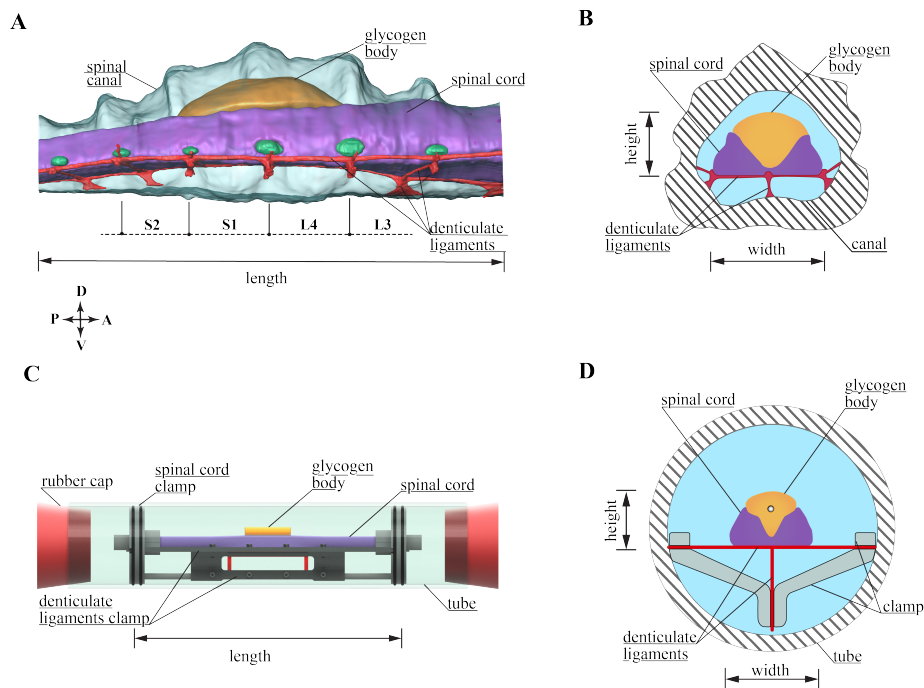
Figure 4.7: Simplification and scaling of the LSO morphology to study the impact of ligaments on soft tissue mobility. (A) Right lateral view at the lumbosacral region of a 3D domestic chicken model. The medial ligaments make up the vertical part of the denticulate ligament network, which in the juvenile chicken were visible beyond the segments with prominent glycogen body. (B) Anterior view on the schematic transverse section of the lumbosacral canal combines the S1-L4 fusion region of the maximum glycogen body height and vertebrae where a medial ligament is observable in the chicken sample. (C) The biophysical model with the spinal cord and glycogen body was designed based on the 3D common quail morphology described in Chapter 3, and denticulate ligament network topology parametrized based on the chicken sample digital dissection, mounted in a fluid-filled glass tube with an inner diameter of 51 mm. (D) Anterior view on the schematic transverse section of the LSO biophysical model combines replicated soft tissue, and the denticulate ligament network consists of horizontal and vertical parts. Image (C) is by An Mo.

Simplification and Scaling Denticulate Ligament Network

We applied a parametric design and tested different fabrication methods and prototypes of the simplified architecture to find one that made the biophysical soft tissue sensitive to the ligaments' pretension configuration and the amount of applied acceleration. The simplified design of the denticulate ligament network includes key topology features we have observed in the domestic chicken lumbosacral organ. The transverse and vertical medial ligaments mimic an assembling design as if they extruded from the intersection nodes located segmentally on the ventral longitudinal ligament. Following topographic anatomy, we positioned the three bilateral transverse ligaments equidistantly along the length of the glycogen body. The resulting distance between the transverse ligaments at the glycogen body region was applied to arrange the rest of the transverse ligaments. The location of the medial ligaments was also consistent with anatomical observations outside the glycogen body location. The various angles formed by intersecting ligaments have been simplified to right angles. To install the qualitatively replicated soft tissue system adjacent to denticulate ligaments, we designed the medial and lateral ligaments clamped at their ends were designed fixtures clamp installed along the left and right lateral and ventral sides of the internal tube wall (see Figure 4.8 D).

We have no aim to mimic the structural or mechanical complexity of the chicken LSO. We developed a simplified, parametric model with a low, appropriate number of design parameters for testing our assumption on the denticulate ligament network function. Thus, the spinal cord and the glycogen body for the biophysical simulation were replicated by approaching a protocol of simplifying, scaling, and fabricating the common quail lumbosacral organ that we have developed as part of the project on quantifying how the LSO morphological features impact the entrainment of the soft tissue under external loads (see Chapter 5).

Fabrication of the Biophysical Model

To find a suitable material to replicate the simplified morphological and physical parameters of the spinal cord and glycogen body qualitatively, we tested different materials and approaches (see description of the soft tissue fabrication protocol in Chapter 5). We individually molded the spinal cord and the glycogen body with silicone rubber (Ecoflex 00-10). The molds were pre-treated with a release agent (Ease Release 200, *Smooth-On*), and liquid-degassed silicone was poured into the molds. To give the glycogen body a visual contrast, we added yellow pigments (Silc Pig, *Smooth-On*) to the silicone before the molding stage. The density of the silicon models of the spinal cord and the glycogen body was identical equal to $1.04\,\mathrm{g/cm^3}$). Since the glycogen body is about $25\,\%$ denser than the spinal cord, we inserted aluminum rods into the glycogen body model to increase its density to $1.46\,\mathrm{g/cm^3}$. We inserted separated rods to retain the glycogen body model's flexibility.

We applied an anisotropic elastic microfiber fabric (MSC-00014-S, *Stratasys*) with thickness $436\,\mathrm{\mu m}$ ($\pm\,16$) that stretches 26 times more easily in one direction than
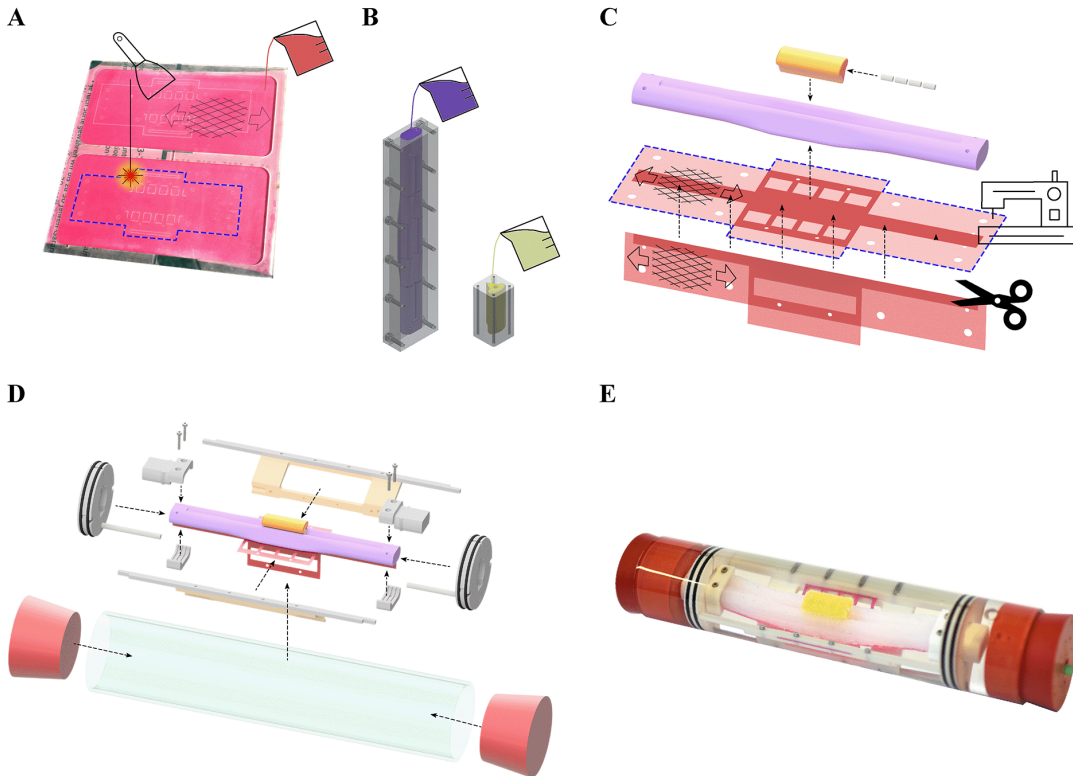
Figure 4.8: Fabrication of the LSO biophysical model with extended ligaments network. (A) Coating the microfiber cloth with a thin layer of silicone rubber (Ecoflex 00-10) and laser cutting already cured fabric by the pattern of the simplified denticulate ligament network topology. Arrows indicate the high-stiffness direction of the microfiber cloth; orthogonal is its low-stiffness direction. (B) Individual modeling of the spinal cord and the glycogen body using silicone rubber (Ecoflex 00-10) according to the protocol approached in Chapter 3. (C) Stitching together two pieces of microfiber fabric cut from the patterns of the transverse and medial ligaments, gluing the ligament model to the ventral side of the spinal cord model. Insert aluminum rods into the glycogen body to increase its density. (D) Clamping ends of the LSO model with custom build fixtures and mounting it inside a glass tube. (E) Photo of the assembled LSO model inside the glass tube filled with water. Images (A), (B), (C), (D) are by An Mo.

the perpendicular one (Hepp and Badri-Spröwitz, 2021) to fabricate denticulate ligament network. We coated the fabric with a thin layer of silicone rubber (Ecoflex 00-10) to increase stiffness in both directions. To avoid curing the silicone layer on the overstretched and distorted fabric, we firmly attached the fabric to a flat surface before applying silicon. The attachment method allowed us to remove the air bubbles accumulated between the surface and the attached fabric as the silicone spreads over the fabric's surface. The coated fabric of thickness $586\,\mu m$ ($\pm$ 17) was laser-cut following the simplified ligament topology pattern. The step of the fabric cut was after the silicone had been cured since the coating causes non-linear behavior of the fabric (Farboodmanesh et al., 2005). To make the step maximally reproducible, we focused on developing the method of stitching both pieces to each other using a sewing machine (Super J15, *Toyota*). We tested several approaches of stitching a vertical piece of tissue at right angles
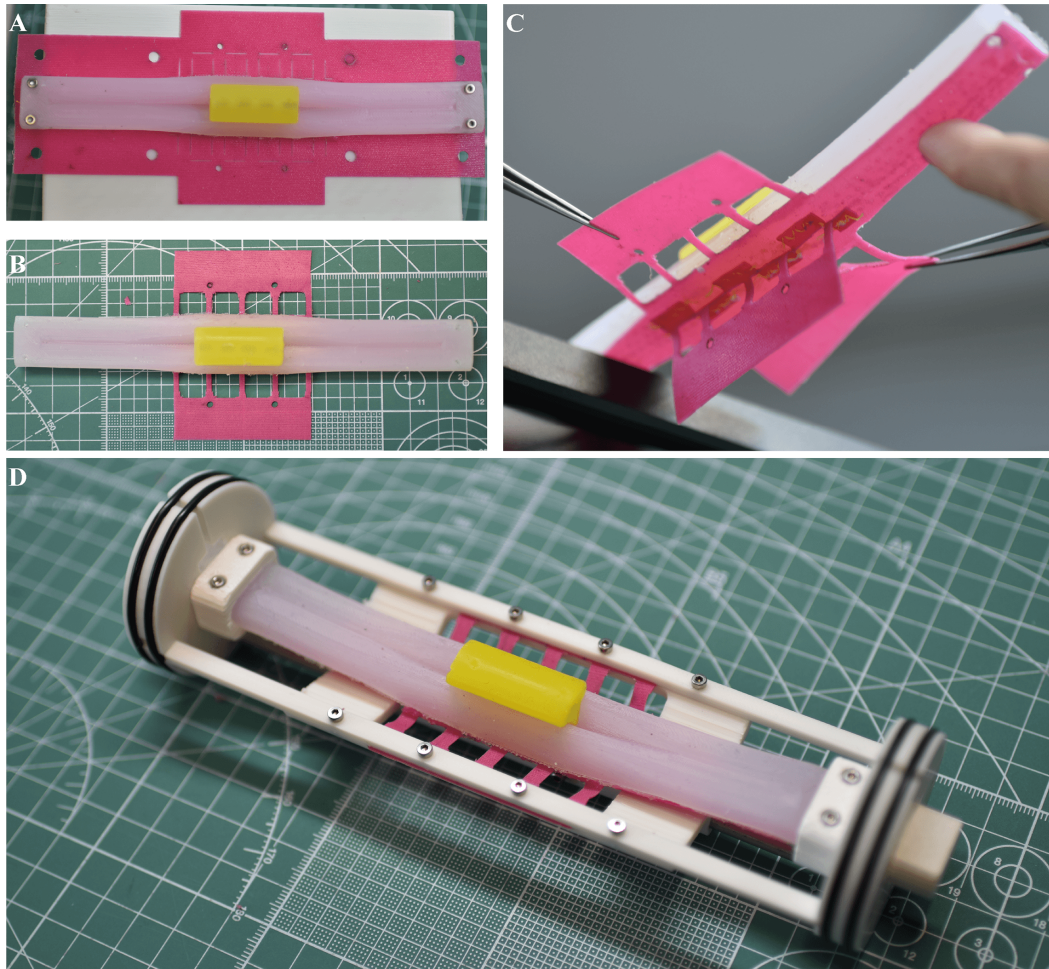
Figure 4.9: Fabrication of denticulate ligament network biophysical model.
(A) The dorsal view on the soft tissue model is glued to a piece of microfiber tissue replicating the ventral dentate ligaments. (B) The same view on the LSO model, but after trimming an excess microfiber cloth. (C) The ventral view on the LSO model demonstrates transverse and medial ligaments stitched at right angles using a "zig-zag" stitch. (D) The LSO denticulate ligaments clamped with the designed fixtures clamp at the ends.

with a horizontal one to replicate the position of the medial ligaments relative to the transverse ligaments. We slit the fastening line perpendicularly with equal spacing along the vertical piece of fabric to sew it at right angles along the middle line of the horizontal fabric (see Figure 4.9). The edges of the cut fabric were crosswise stitched to the horizontal piece of fabric along its middle line using a "zig-zag" pattern. At the final fabrication step, we glued the denticulate ligaments model's horizontal part with the spinal cord's ventral side with silicone glue (Sil-Poxy).

Mechanical Simulation of Soft Tissue Deflection

To test our hypothesis that denticulate ligaments constrain soft tissue mobility inside the lumbosacral canal, we use two configurations for the denticulate ligament network's biophysical model, changing their pretension parameter.

We approached two ligaments configuration: "relaxed" and "tensioned" (see Figure 4.10). We achieved the "relaxed" configuration of the LSO biophysical
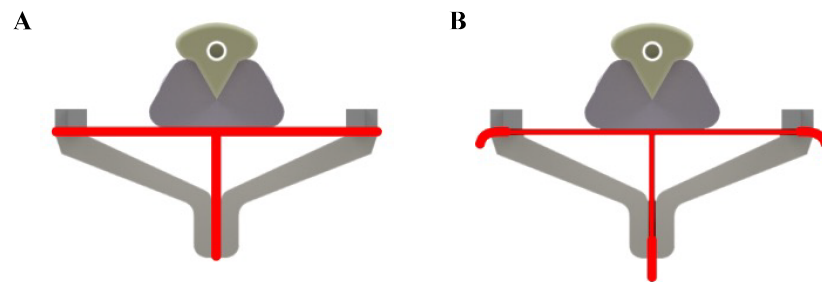
Figure 4.10: Pre-tensioning configuration of the denticulate ligament network biophysical model. Anterior view on the rendered transverse section of the (A) "relaxed" and (B) "tensioned" configuration models. Both images are by An Mo.

model by clamping transverse and medial ligaments at their ends without any tension. For getting the "tensioned" configuration of the ligaments' biophysical model, we stretched both transverse and medial ligaments by 3.5 mm and clamped them tightly by fixtures. We developed a mechanical simulation that aims to study the behavior of soft tissue under static and dynamic accelerations. We mounted to a 3D-printed PLA platform the glass tube contained inside
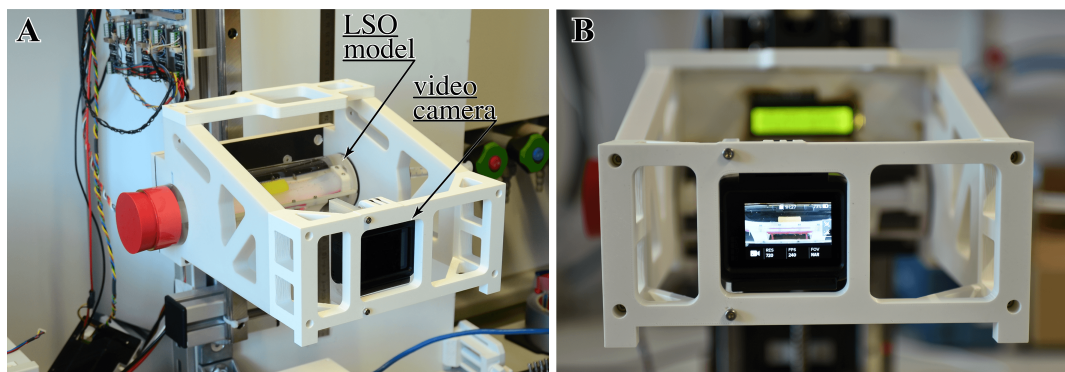
Figure 4.11: The solid PLA platform holds the LSO model and the video camera. (A) Oblique view on the 3D-printed PLA platform shows a mounted biophysical LSO model on one side and the GoPro video camera on the opposite side. (B) View of the LSO model through the camera LCD screen.

the LSO biophysical model (see Figure 4.11 A). On the opposite side of the platform, we mounted a compact video camera (Hero 5 Black, GoPro) so that the lens focuses on the lateral side of the biophysical LSO model Figure 4.11 B). Installing the camera and the biophysical model on one solid platform allows the camera to record the soft tissue response to static and dynamic accelerations in a local coordinate system.

Soft Tissue Deflection under Static Acceleration

Using a biophysical model that replicates the chicken lumbosacral organ based on the results of the digital dissection, we repeated our experiment on studying the

soft tissue deflection under the static state. The biophysical simulation benefit is that we can manipulate the model's parameters. We tested the impact of the ligaments on soft tissue mobility by tuning their pretension. With this aim, we have the biophysical model at both "tensioned" and "relaxed" configurations of the denticulate ligaments (see Figure 4.10). By altering the applied gravity orientation, we measured the biophysical model soft tissue deflection at both configurations under static acceleration. We approached the fixed-mounted camera to record the relative position of the soft tissue inside the glass tube at both standard (see Figure 4.12 A) and inverted (see Figure 4.12 B) orientations. We recorded the soft tissue deflection in a video format and then converted it to 28 single images in a [Tiff] format using Adobe Premiere Pro (version 2021). Measurements of soft tissue position inside the tube were repeated
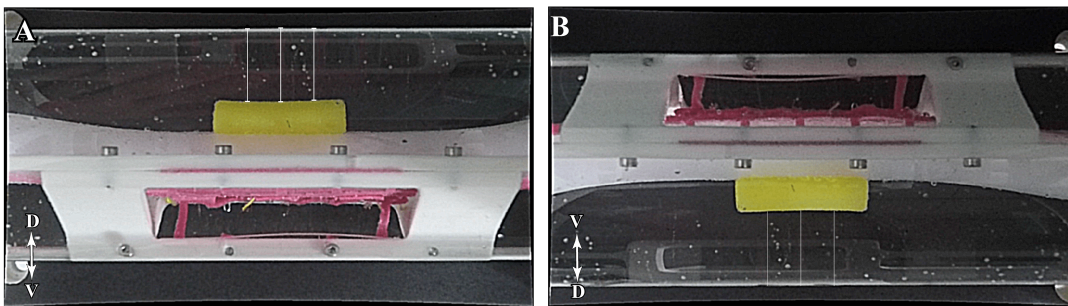
Figure 4.12: Measurement soft tissue deflection under static acceleration. The soft tissue deflection was estimated as the difference of distances between the glycogen body and a glass tube measured on the biophysical model in its (A) down (inverted) and (B) up (standard) orientations.

seven times per each orientation equally for both configurations of the ligaments. The soft tissue position was measured by the distance between the edge of the glycogen body's dorsal side and the edge of the glass tube, where the soft tissue is mounted. For measurement accuracy, the average distance was estimated for each image with three lines from the middle and both ends of the glycogen body (see Figure 4.12). For the measurements, we used ImageJ open-source image processing software (version 1.51w, https://imagej.nih.gov/ij/). However, the distance measurements between the edges of the glycogen body and the glass tube required preprocessing. The boundary of the glycogen body and the glass tube must be plain, i.e., it must be freed from any internal artifacts. Next, we compared the averaged distances between the glycogen body and the glass tube measured in the standard and inverted LSO model orientations for the same ligament configurations.

Soft Tissue Deflection under Dynamic Acceleration

The dynamic deflection test allowed us to study the dependence of soft tissue mobility constrained by dentate ligaments in different pre-tensioning configurations on the amount of external acceleration. We applied a manual oscillation to the LSO biophysical model for both configurations. The locomotion simulator used to quantify individual LSO morphological features in Chapter 5, which produces oscillations up to a maximum 4.5 Hz at ± 5 mm amplitude,

was not applicable. Thus, studying the dependence of soft tissue deflection on external acceleration required an observable amplitude for which a sufficiently high acceleration had to be applied. We simulated the vertical locomotion manually by placing the LSO model and camera housing the PLA platform in standard orientation on a vertical linear rail (SVR-28, *MISUMI*) to avoid undesired rolling/pitching motion. Manual linear shaking with an amplitude of $\approx 60\,\text{mm}$ and a frequency of $5\,\text{kHz}$ measured with a linear encoder (AS5311, *AMS*) resulted in soft tissue vibrations within the tube for both configurations of the denticulate ligaments. We extracted soft-tissue displacement data from video recorded by a fixed-mounted camera at $240\,\text{Hz}$ using open-source image analyzing software (Tracker, https://physlets.org/tracker/).

4.2 Results and Discussion

4.2.1 LSO Processing Efficiency for Visualization

MRI data of a sample fixed and scanned in $10\,\%$ NBF solution and a sample that, after isolation from the rest of the body, was immediately immersed in isotonic saline and scanned with identical scan settings we compared based on the image quality and visibility of anatomical structures. Chemical-free treated samples scanned in isotonic saline allowed to segment in 3D soft anatomical structures, including accessory lobes and some parts of longitudinal ligaments (see Figure 4.13 E and F). The specimen fixed with $10\,\%$ NBF also preserved the soft anatomical structures (see Figure 4.13 A and B). But, the fine LSO structures - the accessory lobes and dentate ligaments - became visible only on μCT after iodine amplification (see Figure 4.13 C and D). The comparison of MRI data indicated that the sample does not need to be chemically fixed but needs to be scanned in isotonic saline.

The chemical-free MRI protocol allowed us to visualize in 3D the soft tissue without a shrinking effect and also showed the topographic anatomy of the accessory lobes relative to the nodes on lateral longitudinal ligaments. However, by imaging the chicken spinal sample of the lumbosacral region with μCT, we achieved on $20\,\mu$m higher resolution than with MRI. Moreover, the MRI-compatible markers intended to align the inverted sample scan to its standard orientation scan showed us a low contrast. The low image contrast is one of the primary reasons we considered that the MRI data is unsuitable for accurately measuring the relative soft tissue position inside the lumbosacral canal. As alternative markers for alignment, the anatomical features were also qualified as unsuitable. The different bone densities and imaging system errors reduced the potential accuracy level achievable. Therefore, despite the advantage of MRI in preserving the shape of the soft tissue, we measured the soft tissue deflection inside the chemically processed sample of the lumbosacral region scanned with μCT.
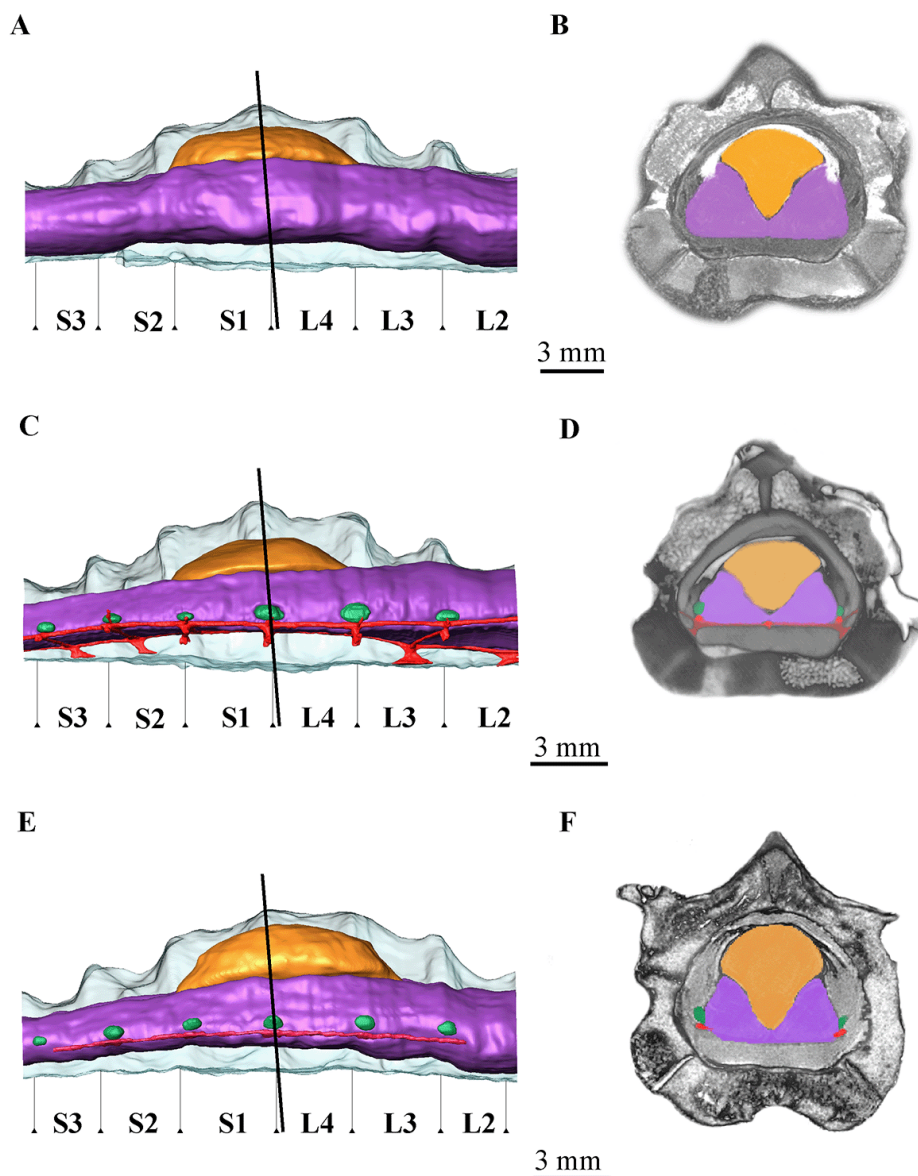
Figure 4.13: Comparison of 3D models created on the different LSO processing protocols. The LSO processing results are exhibited in three 3D models arranged from top to bottom. LSO soft tissue surrounded by cerebrospinal fluid, shown from the right lateral view on the left side of the figure. On the right side, the transverse section through the spinal canal at the fusion region of the S1 and L4. In (A) and (B), the sample with carving holes through the vertebral body, fixed with 10 % NBF during nine days and scanned with a 14.1 Tesla MRI, allowed segment in 3D a glycogen body and a spinal cord surrounded by a cerebrospinal fluid-filled inside the lumbosacral spinal canal. In (C) and (D), the same sample with the opened inlet through the vertebral body was fixed for three additional months with 10 % NBF and stained with 4 % Lugol's solution for 65 hours, allowed to segment fine structures: accessory lobes and denticulate ligament network. In (E) and (F), the freshly isolated lumbosacral region immersed in the isotonic saline and scanned with MRI showed the glycogen body, the spinal cord, and marginal accessory lobes contacting nodes on the lateral longitudinal ligaments.

4.2.2   Static Deflection on Micro-CT Data

The anatomical topography and physiological function of the specializations in the lumbosacral region have been described in some detail based on results of classical dissection approaches (Azcoitia et al., 1985; C. Benzo and L. De Gennaro, 1981; Eide and Glover, 1996; Necker, 2005; Schroeder and Murray, 1987; Watterson, 1954), digital dissection approach (Stanchak, French, et al., 2020) and by applying both types of approaches (Haimson et al., 2021; Kamska, Daley, et al., 2020). Following our assumption that LSO, similar to the fluid-filled mass-spring-damper system, acceleration sense is one of the essential mechanical parameters for the neural soft tissue, which conceivably moves inside the lumbosacral spinal canal. However, the mobility of the neural soft tissue in the avian LSO remains unclear. The currently available imaging tools do not allow examining *in vivo* the soft tissue response to external acceleration caused by avian locomotion. However, an alternatively approached *in situ* method also limits us from imaging the soft tissue directly inside the canal at the dynamic state. To examine whether the neural soft tissue is sensitive to acceleration, we scanned a chicken cadaver lumbosacral region in a static state by altering the applied gravity orientation.   The hypothetical sensitive axis
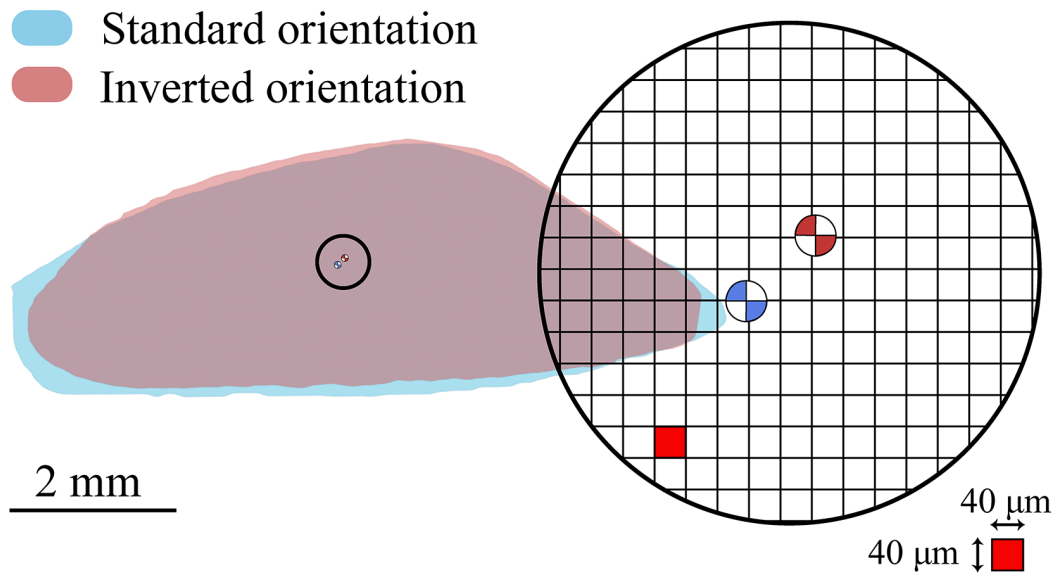
Figure 4.14: Assessment of soft tissue deflection within the lumbosacral canal. The soft tissue deflection measured *in situ* on a difference of glycogen body positions in standard and inverted orientations. Position for movable glycogen body in each scanning orientation was detected relative to three markers attached to the outer surface of the lumbosacral spine. The measurements were on LSO μCT data produced using our modification of the diceCT protocol.

was aligned with the force of gravity constantly acting on the glycogen body in both orientations. Based on the μCT data (with a 40 μm voxel edge), the lumbosacral region is scanned in its standard and inverted orientations. We segmented in 3D a glycogen body to measure the soft tissue deflection relative to their position inside the spinal canal. We aligned the sample μCT data scanned in an inverted orientation to the same sample but scanned in its standard

orientation to measure the glycogen body position changes. We approached three steel markers directly attached to the bone surface for digital alignment. We segmented three markers in 3D based on μCT data of the sample scanned in inverted and standard orientations. The results of an investigation of glycogen body displacement based on a comparison of two oppositely oriented scans of the same specimen, which were aligned using a set of markers, revealed a soft tissue deflection in the dorsoventral spinal direction equal to 82 µm (see Figure 4.14) with an error of 80 µm. Revealed displacement of the neural soft tissue on 82 µm under the glycogen body's quasi-steady load indicates the potential ability of the LSO to generate proprioceptive signal via excitation of accessory lobes by ligaments strain caused by the soft tissue displacement (Schroeder and Murray, 1987). We evaluated the level of deflection relative to the fluid space inside the channel available for movement. But to understand the magnitude of soft tissue deflection, it is essential to evaluate the level of deflection relative to the fluid space inside the channel available for dorsoventral movement. We approached the evaluation of the space by morphometric measurement described in (Kamska, Daley, et al., 2020) by averaging two neighboring mid-vertebra values of L4 and S1 vertebrae. Digital dissection of the chicken lumbosacral region based on μCT showed that the maximum static deflection takes only 3 % relative to the fluid space below and above the neural soft tissue that is potentially available for soft tissue movement. However, considering the 3D anatomical observations that show an additional vertical part of the denticulate ligaments extending between the spinal cord ventral surface and the dura of the spinal canal allows us to assume that bounded soft tissue can move freely only on the ventral side of the canal. In such a case, the soft tissue quasi-static deflection measured *in situ* takes up 8 % of the available space.

4.2.3 Evaluation of *in situ* Measurement Errors

The imaging system, data collection, and analysis used to measure static soft tissue deflection *in situ* resulted in the uncertainty of the result. Moreover, 82 µm of the soft tissue's static deflection measured *in situ* is close to the μCT scanner resolution equals 40 µm. To evaluate the accuracy of our measurements of the soft tissue deflection, we need to detect and evaluate the major sources of the system errors. We distinguished four major sources of error (see Figure 4.15) that resulted from the 3D segmentation of a glycogen body and markers. The uncertainty caused by the imaging facility system is the first link in a chain of cause-and-effect errors. The next links that continue the chain are 3D segmentation, applying the cost function to alignment, and alignment itself.

The error caused by differences in the 3D segmentation of markers scanned in their different orientations is estimated by the shape parameter of the outer surface. To estimate the error caused by the shape parameter, we compared cross-sections of two different 3D models of the same physical marker. We took a cross-section through each marker along a triangular plane formed by the cloud of 3 markers (see Figure 4.16). The triangular plane represents the area available for translation and rotation of the pre-aligned inverted marker cloud relative to the cloud in the standard orientation. Before comparing 2D cross-sections
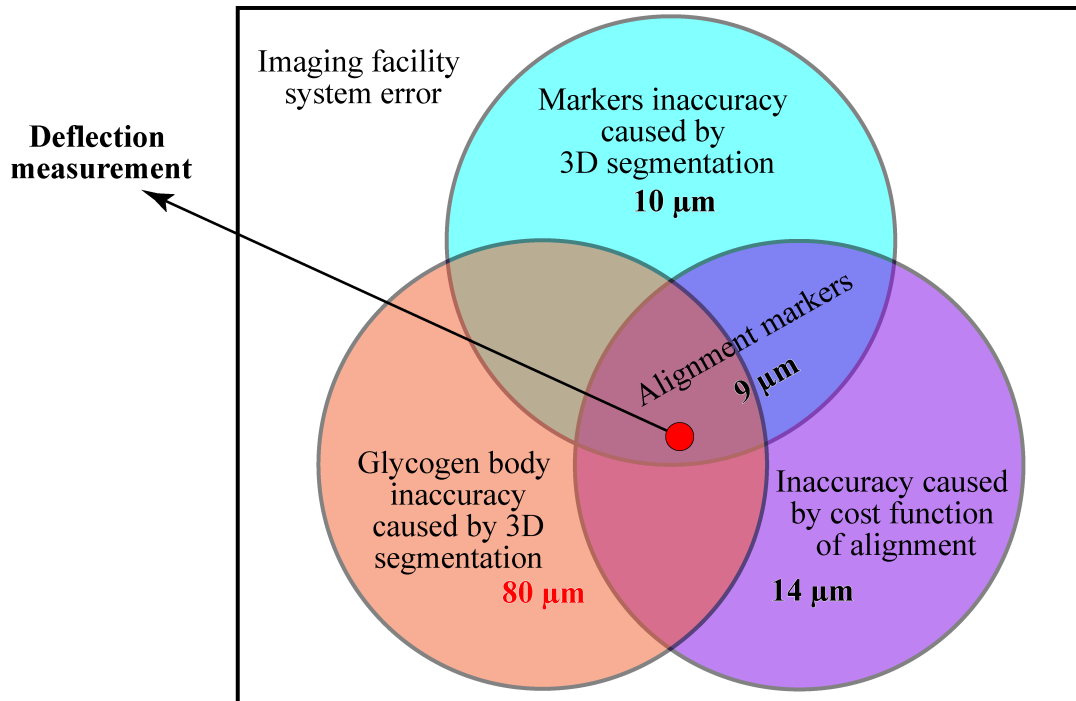
Figure 4.15: Primary sources of errors that caused uncertainties in 3D models alignment. The Venn diagram shows four major error sources resulting from the imaging facility system that caused uncertainty of the static deflection measurement *in situ*. Scanning in two opposite orientations, 3D segmentation, and alignment of corresponding three steel beads markers resulted in a chain of cause-and-effect errors. Varying of the signal intensity for the same markers scanned at two different sessions and automatic 3D segmentation resulted in an error of 10 µm. The variation of 3D models' shapes caused the deviation of the models' COM. As a result, the distance between markers scanned in inverted orientation is not identical to the distance between corresponding markers scanned in the standard orientation, leading to the inaccuracy of 17 µm, inherent in any alignment method we would choose to apply for alignment (see Table 4.1). The markers' misalignment of the inverted 3D model to the standard caused an error of 12 µm, the minimal one of the imaging facility system. The 3D models' shape variation of the same glycogen body scanned in its standard and inverted orientations resulted in the error caused by shifting a center of mass toward the broader region of the 3D model. Thus 3D segmentation of the glycogen body resulted in an error of 80 µm, the maximal one of the imaging facility system error.

of two different 3D models of the same marker, we individually aligned these 3D models by their center of mass. Then we estimated the thickness of the non-overlapping area of compared 2D cross-sections. The analysis revealed that the second marker gives the maximum error of a quarter voxel relative to two other markers (see Figure 4.16 B). The errors of the first (see Figure 4.16 A) and third (see Figure 4.16 C) markers are less than half a voxel.

Errors caused by the imaging facility and 3D segmentation resulted in different distances between the inverted scan markers than those between the same physical markers but scanned in the standard orientation. The difference
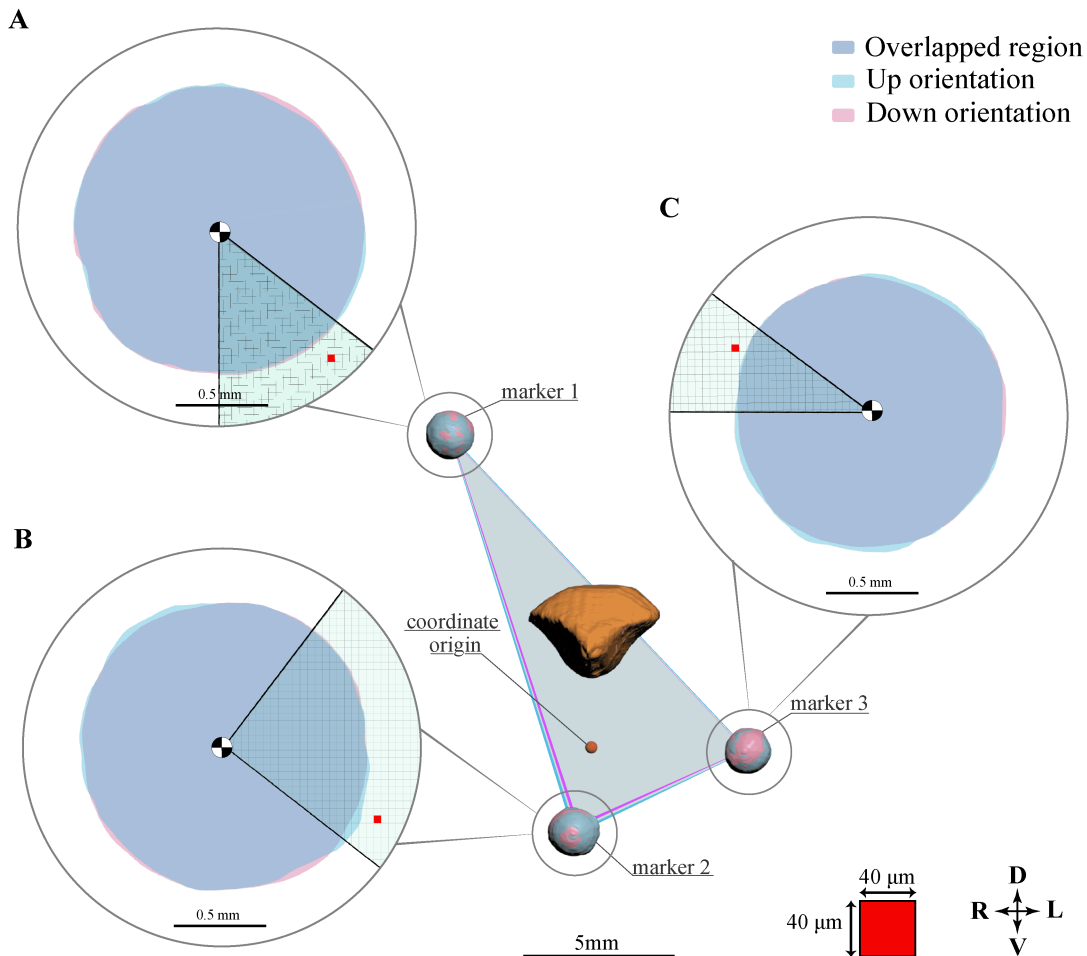
Figure 4.16: Errors estimation of glycogen body deflection measurements caused by markers imaging. The error caused by 3D segmentation of markers is evaluated individually for (A) "Marker 1", (B) "Marker 2", and (C) "Marker 3" based on non-overlapping regions of 2D cross-sections through the 3D models of the marker scanned in two orientations. The 3D models of the corresponding marker were preliminarily aligned by their centers and then cross-sectioned along the plane formed between three markers. The figure in the center shows the result of the final alignment of the inverted sample to the standard sample. The marker-based alignment resulted in the errors caused by the 3D segmentation plus the cost function of the applied alignment method and the alignment itself.

Table 4.1: Error caused by imaging and 3D segmentation of standard and inverted models.

Markers	Distance between markers, [mm]		Difference of distances, [mm]
	Standard	Inverted	
1-2	13.861	13.855	0.006
2-3	18.327	18.314	0.013
3-1	23.117	23.084	0.033
Mean.			0.017
SD			0.014

in distance between 3D models of the corresponding markers scanned in different orientations affects the accuracy of the alignment method we apply in the next step. The same physical markers scanned in two different orientations formed two not congruent triangles (see Figure 4.16). The average difference in the distances between the corresponding markers from the standard and inverted orientation scans is 17 µm (±14) (see Table 4.1). This value is a cost function, which shows the error inherent to the system, even before we align models. In other words, we have measured an error that is a priori included in any method that we apply at the alignment stage.

The error caused by the glycogen body was estimated similarly to the methods approached for evaluating an error caused by markers' μCT scanning and 3D segmentation. We also evaluated the shape parameter on the surfaces' irregularity of the standard and inverted 3D models aligned by their COM (see Figure 4.17). Based on the thickness of a non-overlapping region of 2D sagittal sections through the glycogen body 3D models, we found that the surface irregularity of the glycogen body gives an error equal to 2 voxels. Thus, an evaluation threshold of an uncertainty influenced by the quality and quantity of steps applied by conducting the *in situ* tests, we chose maximum permissible error (A. Thompson et al., 2021) caused by 3D segmentation of the glycogen body.
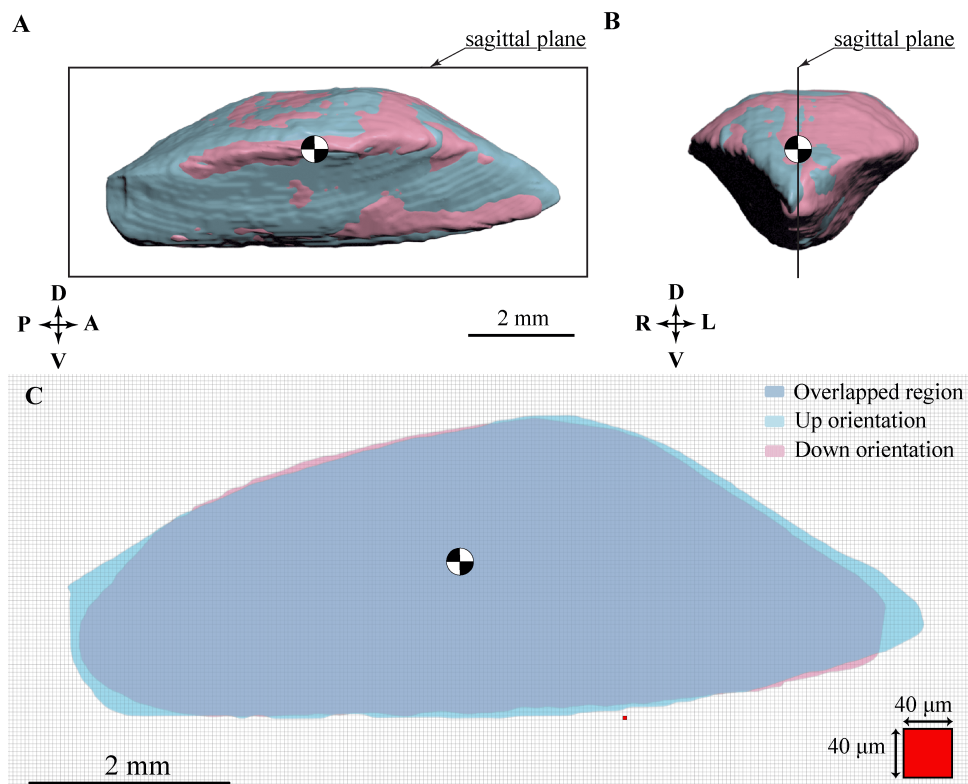
Figure 4.17: The measurement error estimation of the glycogen body deflection caused by the glycogen body imaging. (A) Sagittal and (B) anterior views of center-aligned 3D models of the glycogen body scanned in upper and lower orientations. Error evaluation based on (C) non-overlapping regions of 2D sagittal sections through the center-based aligned 3D models of the glycogen body scanned in the up (standard) and down (inverted) orientations.

For the alignment transformation of the inverted 3D model to the standard one, we applied the iterative closest point (ICP) algorithm in MatLab (Besl and McKay, 1992), which allowed us to minimize the distance between two markers clouds. Error caused by alignment estimated as the mean of distances between corresponding markers equals 12 µm (±9).

4.2.4 Anatomical Observation

Our modification of the diceCT protocol allowed us to update a 3D map with details on the topology of the denticulate ligament network, determine osteological features that characterize the transverse grooves on the dorsal side of the lumbosacral spinal canal, and generate 3D models of the marginal accessory lobes (see Figure 4.18). Anatomical observation of the denticulate ligament network suggested that the network's topology reduces the soft tissue mobility inside the lumbosacral canal. Also, the study of the three-dimensional topographic anatomy of the accessory lobes allowed us to assume that the mechanism of their stimulation is associated with both the ligament strain and cerebrospinal fluid flow.

Denticulate Ligament Network Topology

The attachment of the denticulate ligament network via processes to the dura has an important biomechanics role by elevating, supporting, and stabilizing the spinal cord loaded with the glycogen body inside the spinal canal, both at rest and in dynamics (McCormick and Stein, 1990; Polak-Kraśna et al., 2019; Schroeder and Murray, 1987). Micro-computed tomography (40 µm voxel edge) of a juvenile chicken lumbosacral region allowed us to determine and segment in 3D not only a horizontal part of the denticulate ligament network, earlier observed in quail and described in chapter Chapter 3, but vertical part classified by Necker, 2005 as medial ligaments (see Figure 4.18 B, C, E and Figure 4.19 A). Additionally, we could examine in 3D the attachment of the network horizontal part to the lateral sides of the canal via ventral and lateral processes that had been identified earlier by Schroeder and Murray, 1987 on 2D histology slices (see Figure 4.18 C, D, E and Figure 4.19 B). Ventral processes and medial ligaments are the thicker parts of the ligament network, varying in diameter from 3 to 12 voxels. In comparison, lateral processes are the thinnest ones, from 1 to 4 voxels in diameter.

Denticulate Ligament Network Processes

The ventral and lateral processes extend between the nodes on the lateral longitudinal ligaments and the dura mater at the fusion of adjacent vertebrae. Digital histological sections through the spinal canal revealed that the lateral and ventral processes attach to the bony canal in 2 different junctions of the neural arch (see Figure 4.19 B). The bilateral lateral process attaches to the junction of the lamina and pedicle, right below the opening of the groove into the spinal canal. The bilateral ventral process attaches at the junction point of the pedicle and vertebral body. Schroeder and Murray, 1987 noticed that
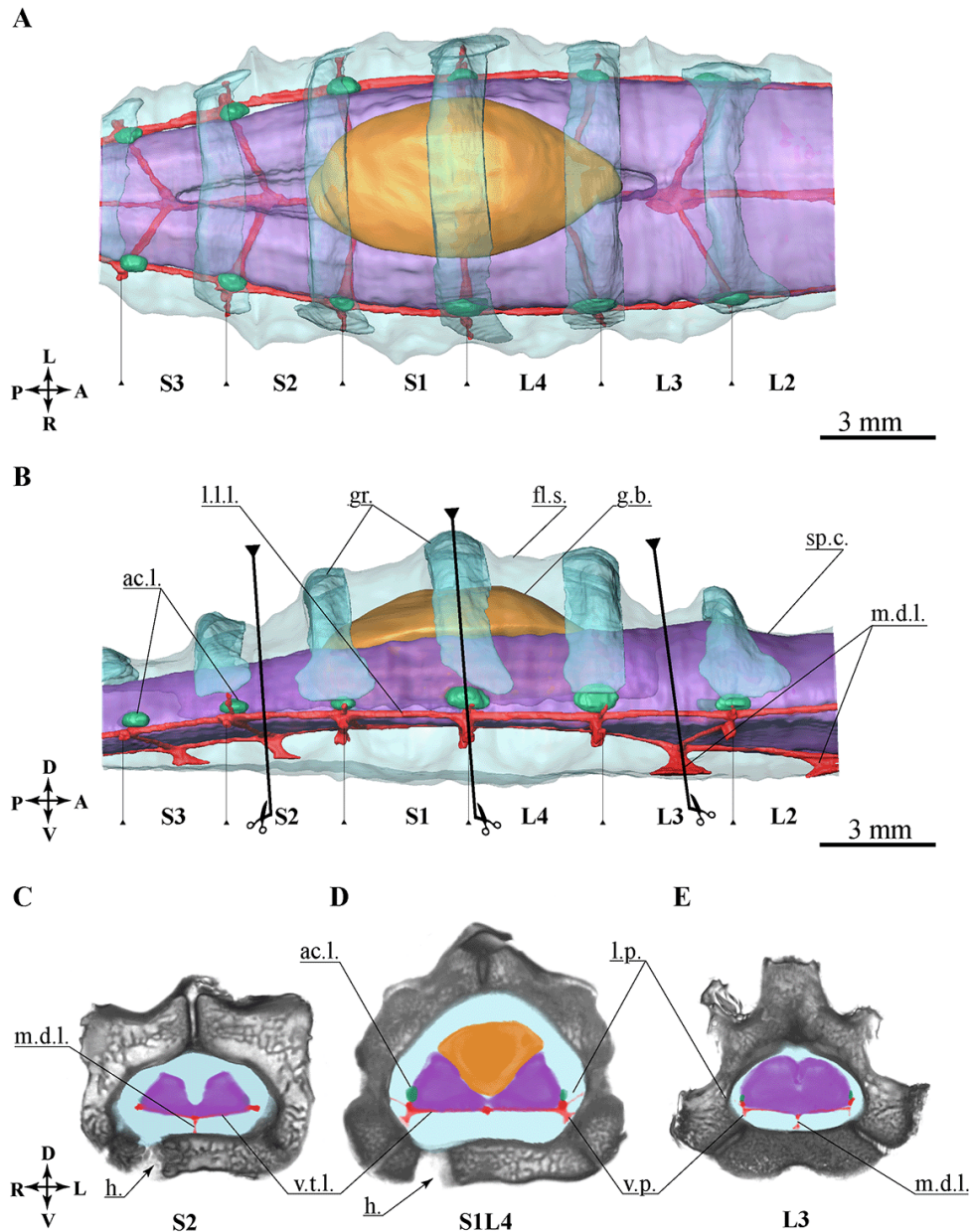
Figure 4.18: Chicken LSO anatomical features in 3D. Digital dissection based on μCT data obtained through our modification of the diceCT protocol. The 3D model demonstrates the morphology and topographic anatomy of the soft tissues and fine structures that constitute the lumbosacral organ. Topographic anatomy of the neural soft tissues: a glycogen body, spinal cord, and bilaterally extruding accessory lobes relative to the denticulate ligament network topology and the transverse grooves of the bony spinal canal shown from (A) dorsal and (B) right lateral views. Transverse sections through the fused lumbosacral spinal column at (C) S2, (D) S1L4, and (E) L3 show interposition of the accessory lobes and intersection nodes of lateral longitudinal ligaments with transverse ligaments. Outside the glycogen body location, the transverse ligaments form a "V" shape. The transverse ligaments form a straight line at the site of the glycogen body, between the S2-L4. See abbreviations in Table 1.
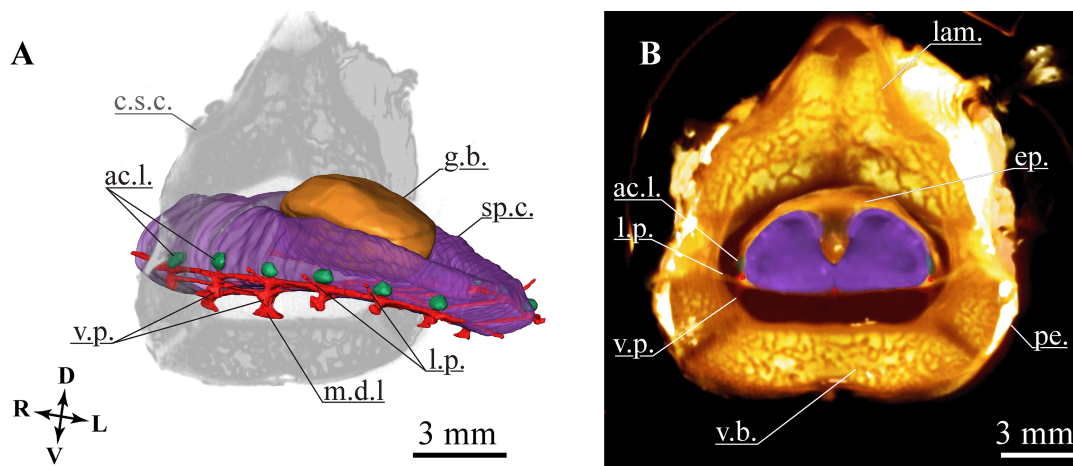
Figure 4.19: Osteological features of the attachment sites for the network's processes. (A) Lumbosacral soft tissue's posterior oblique view shows an area where the ligaments are attached to the lumbosacral spinal canal. (B) Digital histological slice demonstrates the spinal canal regionalization and denticulate ligament network attachment sites via the lateral and ventral processes. The 3D map shows the topographic anatomy of the accessory lobes relative to the denticulate ligament network and osteological features of the spinal canal. See abbreviations in Table 1.

the width of the ventral processes is more than would be estimated on the lumbosacral soft tissue parameters. We estimated that the thickness of the ventral processes is about five times higher than the lateral ones. The width could have a biomechanical function associated with potential asymmetrical limitation of the neural soft tissue movement inside the canal. Still, to avoid speculative interpretation, morphological observation must be explored in the future for biomechanical properties.

Medial Ligaments

The medial ligaments are overlooked in the literature. So far, only Necker, 2005 documented their presence based on 2D histological slices through the lumbosacral region of 7-day-old pigeons and newly hatched and embryonic chickens. We focused on the medial ligament distribution along the lumbosacral segments in 3d. Based on our μCT scan of a juvenile chicken, the medial ligaments were visually detected only in the lumbar (L3, L2) and sacral (S2, S3) vertebrae, in the region without the glycogen body (see Figure 4.18 B, C, E). Our observation coincides with Necker's observation on the newly hatched chicken (see Figure 21 B and 22 B in Necker, 2005). However, Figure 1 of Necker, 2005 shows that in the pigeon's LSO, the medial ligaments were identified at the glycogen body region. We could interpret this variation of the ligament network topology results from an evolutionary adaptation that correlates with the locomotion modalities. However, it is necessary to study more samples of birds of the same age category from different locomotor modality groups so that our assumption does not become a speculative statement.

In contrast to the lateral and ventral processes attaching to the spinal canal at

the junction of the vertebral bony parts, medial ligaments attach to the canal at the middle region of a corresponding vertebral body. From the lateral side, we can observe that the medial ligaments attach to the ventral side of the canal at a non-rectangular angle. Unfortunately, accurate measurements of an attachment degree inside the lumbar segments of the canal are infeasible because of borders between the arachnoid membrane and the medial ligaments are not clear. Still, we can see that the angles between the medial ligaments and the ventral side of the lumbar vertebrae are acute to the glycogen body. Inside the sacral canal segments, the medial ligaments have more explicit boundaries distinguishing them from the edges of the arachnoid mater, allowed to measure that an obtuse angle toward the glycogen body is around 152 (± 6) degree (mean and SD were calculated based on two medial ligaments measured in the S1 and S2 vertebrae on the same lumbosacral sample scanned in three horizontal and one vertical orientation inside the μCT scanning chamber).

The lateral and ventral longitudinal ligaments form a different curvature along the sagittal plane (see Figure 4.18 B). The lateral longitudinal ligaments follow the points of the ventral and lateral processes attachments to the lateral side of the lumbosacral canal. Between the S2 and L3 vertebrae, the ligaments extend in about the same plane but curve slightly from L2 to the anterior side and from S3 to the posterior side of the canal. In contrast, the ventral longitudinal ligament forms a concave down shape. In the range of the glycogen body location (S1, L4 vertebrae), the ventral longitudinal ligament is in the plane with lateral longitudinal ligaments. In the lumbar (L3, L4) and sacral (S2, S3) vertebrae, where medial ligaments are visible, the ventral longitudinal ligament bends downward toward the ventral side of the canal. Following the cross-sections through the lumbosacral canal, we observed that at the segments where we have not detected medial ligaments (L3-L4, L4-S1, S1-S2), the transverse ligaments form an unfolded angle (see Figure 4.18 D). Whereas in the segments with medial ligaments (L1-L2, L2-L3 and S2-S3, S3-S4), the intersection nodes on the ventral longitudinal and transverse ligaments are located below the intersection nodes of the lateral longitudinal ligaments. The cross-sections show that the left and right transverse ligaments form a "V" shape in the case of the medial ligament extruding between the ventral junction and the ventral side of the canal (see Figure 4.18 C, E). Measurement along the cross-sectional plane showed that

Table 4.2: Digitally measured angles between left and right transverse ligaments. Measurements were conducted along the transverse sections settled segmentally through the spinal canal at the ventral intersection nodes. The mean and SD were calculated from the angles measurements at the same lumbosacral spine sample scanned in three horizontal orientations and one vertical inside the μCT scanning chamber.

Transverse ligaments	S4-S3	S3-S2	S2-S1	S1-L4	L4-L3	L3-L2	L2-L1
The angle between [deg]	152 ± 3	163 ± 2	172 ± 0	180 ± 0	180 ± 0	159 ± 3	149 ± 2

the angle between the transverse ligaments formed by the ventral junction with the extruded medial ligament (L2-L3 and S2-S3) is approximately 20 degrees less than the angle formed by the ligaments in the adjacent segments where no medial ligaments were found (L3-L4, L4-S1, S1-S2); and 10 degrees more than the angle measured in one segments (L1-L2 and S2-S3) further from the ones without medial ligaments, but with glycogen body. This observation reveals a general trend that the further the ventral node with the extruded medial ligament from the area of the glycogen body, the smaller angle between the transverse ligaments (see Table 4.2).

Functional Topography of Accessory Lobes Organization

The literature has already described that accessory lobes with potentially mechanoreceptive capabilities protrude from the spinal cord in close association with lateral longitudinal ligaments (Schroeder and Murray, 1987) right at the point of intersection with ventral transverse ligaments (Eide, 1996) below to grooves opening inside the canal (Necker, 1999). However, imaging tools were limited in studying the topographic anatomy of the accessory lobes regarding suggested mechanisms of the LSO mechanosensation. 3D segmentation of the LSO anatomical features allowed us to extract morphometric data and study the topographic anatomy of the mechanosensing accessory lobes. The accessory lobes are hypothesized to be associated with two different mechanisms of accessory lobes' excitation. Data analysis in 3D allowed us to consider fluid and strain-based excitation mechanisms as complementary. We assumed that the mechanism of accessory lobes' excitation by ligaments strain caused by spinal cord oscillations is associated with cerebrospinal fluid flow dynamics through the transverse grooves. However, the deviation in the volume of accessory lobes within the same segment indicates that their shapes were deformed non-uniformly (see Table 4.3). This effect could be caused by chemical treatment, the duration after the chicken was slain, and the organism's characteristics. It limited our morphometric data on accessory lobes for studying the excitation mechanism. Whereas the LSO in 3D allowed us to analyze the topographic anatomy of the accessory lobes relative to the denticulate ligaments network and test the hypothesis that transverse grooves morphology modifies the cerebrospinal fluid flow resistance and affects the amplitude of the soft tissue response is described in Chapter 5.

Table 4.3: Digitally measured accessory lobes' volume. Measurements were conducted segmentally along the spinal cord from the left and right sides. The table presents the mean and SD of accessory lobe volume measured from both sides within the same segment. 3D models of accessory lobes were segmented based on the μCT data of the juvenile chicken.

Accessory lobes	S4-S3	S3-S2	S2-S1	S1-L4	L4-L3	L3-L2
Volume, [mm^3]	0.07 ± 0.01	0.08 ± 0.01	0.08 ± 0.05	0.12 ± 0.08	0.10 ± 0.03	0.07 ± 0.00

MRI scanning of a fresh chicken cadaver lumbosacral region allowed us to evaluate the topographic anatomy of the accessory lobes segmented on iodine-enhanced μCT relative to the lateral longitudinal ligaments and grooves. The observation on μCT data shows that ovoid-shaped accessory lobes are tightly adjacent to the intersection nodes of lateral longitudinal and ventral transverse ligaments from which are extruding the lateral and ventral processes attached to the lateral sides of the lumbosacral canal. The intimate location of the accessory lobe at the apex of the intersection node of the lateral longitudinal ligament and the lateral process indicates that potential mechanoreceptors are ligament-strain stimulated when the soft tissue moves down toward the ventral side of the canal. This interpretation is consistent with the topological features of the dentate ligament network, potentially limiting soft tissue movement to the dorsal side of the canal. (Necker, 1999) earlier already described that accessory lobes are at the level of grooves' lateral opening toward the lumen of the lumbosacral canal. However, osteological structures that organize grooves haven't been described before. The digital histological cross-sections through the lumbosacral canal show that bilateral transverse grooves on the dorsal side of the spinal canal are formed by the adjacent vertebrae laminar parts fusion. The attachment site for the denticulate ligament network's processes serves a cylinder-shaped hard bone pedicle, the lower part of the neural arch that protects the spinal cord and nerves. Thus, a vertebral osteology analysis shows that the accessory lobes at the lamina and pedicle junction level coincide with the grooves' termination level.

4.2.5   Ligaments Influence on Soft Tissue Mobility

Static soft tissue deflection results, measured *in situ*, showed that the LSO soft tissue exhibited a minor change in position. We assume that minor deflection is caused by the medial ligaments, which presumably limit the mobility of the spinal cord toward the dorsal side of the canal. Hypothetically, soft tissue mobility depends on the ligaments' topology and stiffness. But, currently, it is impossible to manipulate with a parameter of the denticulate ligaments pre-tension neither *in vivo* nor *in situ* without destroying the integrity of the LSO interdependent system. We assume that the deflection of the soft tissues depends on the amount of acceleration. This assumption is supported by the soft tissues that slightly change their position when the direction of gravity changes from positive to negative. Unfortunately, the currently available imaging techniques still do not allow us to test our assumptions either *in vivo* or at least *in situ*. Hence, we approached the benefit of the biophysical simulation. The possibility to manipulate with parameters of individual anatomical structures allowed us to test if there is a cause-and-effect of the denticulate ligaments pre-tension on low soft tissue deflection observed *in situ*. We modified the LSO biophysical model that we have designed for the project on studying the time and frequency response of individual key anatomical structures that are potentially relevant to the mechanosensing function of the LSO (see Chapter 5). It is known that the stiffness of different denticulate ligaments is not equal but differs depending on the amount of elastin and collagen in fibrils (Schroeder and Egar, 1990).

Nevertheless, the mechanical properties of avian denticulate ligaments are still unavailable, so we replicated the denticulate ligament network qualitatively. We believe that the material stiffness we used to model the ligaments is somewhat higher than biological ones. The topology observed in 3D based on μCT data of the chicken lumbosacral organ was simplified and scaled. To examine the ligament pre-tension parameter, in the first place, we developed different (in number) qualitative prototypes of the simplified network topology and tested them. We chose the one that, depending on ligament pre-tension, exhibited sensitivity to static and dynamic acceleration acting on the constant mass of the replicated glycogen body and spinal cord.
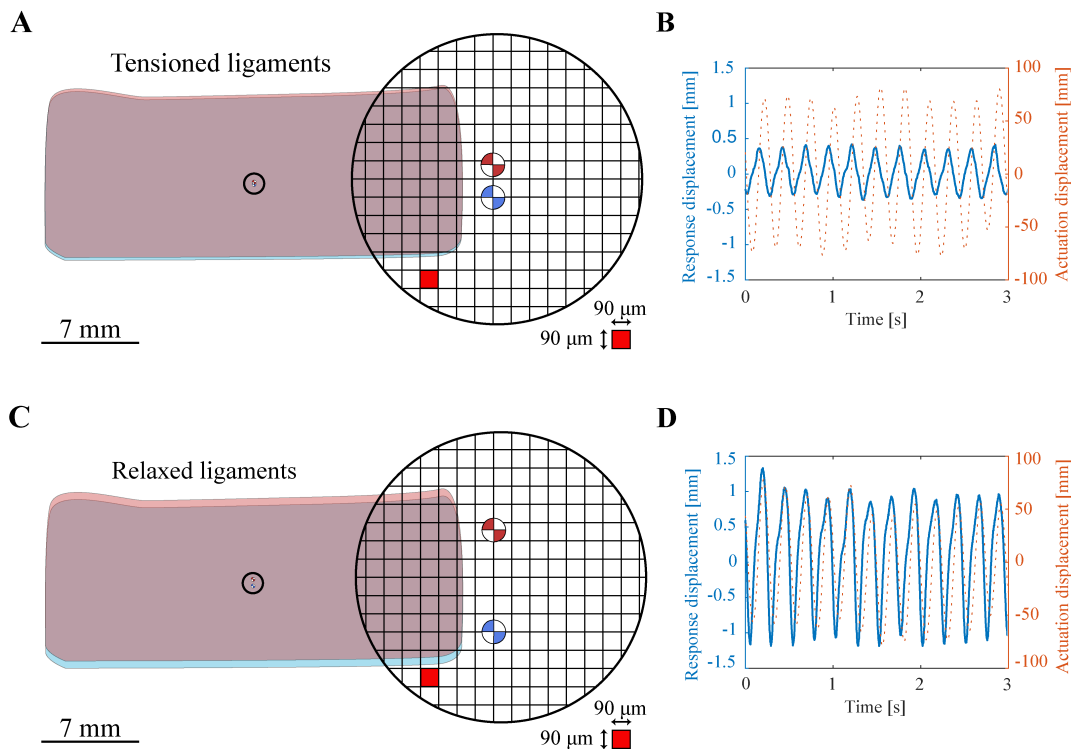
Figure 4.20: Assessment of soft tissue mobility dependence on ligament pre-tension and amount of acceleration. Internal response of qualitatively replicated lumbosacral soft tissue supported by tensioned denticulate ligaments at (A) a static state of the biophysical model and under (B) external actuation. To assess the quantitative contribution of the transverse (horizontal) and medial (vertical) ligaments, we reproduced the static (C) and actuated (D) state for the soft tissue supported with the ligaments in the relaxed configuration. The external actuation on the biophysical model in the tensed and relaxed configurations of the ligaments and generation of plots (B and D) were evaluated by the second co-author of this project, An Mo.

The biophysical experiment established our assumption on the cause-and-effect of the denticulate ligaments pre-tensioning on the soft tissue position changes. The biophysical model of the LSO with tensioned ligaments shows that the soft tissue deflection is equal to 160 μm ($\pm$ 80) in the (see Figure 4.20 A) static state and 700 μm ($\pm$ 40) (see Figure 4.20 B) under dynamic state (see table). The relaxed configuration allowed the soft tissue deflects for 460 μm ($\pm$ 100) (see Figure 4.20 C) at a static state and 2130 μm ($\pm$ 130) (see Figure 4.20

D) at the dynamic state. The evaluation of the static and dynamic deflection dependency on the ligaments' pre-tension revealed the tensioned configuration results in ≈ 3 times less soft tissue deflection than the relaxed configuration, which evidence the deflection increase with acceleration. These results evidence that soft tissue deflection under static and dynamic accelerations directly depends on the denticulate ligaments' pre-tension. The sensitivity of the soft tissue to the amount of acceleration, the denticulate ligaments topology, and stiffness supports the assumption about existing of the strain-based mechanism of the accessory lobes excitation contributes to the lumbosacral organ in percept avian locomotion (Kamska, Daley, et al., 2020; Schroeder, 1986a,b; Schroeder and Egar, 1990; Schroeder and Richardson, 1985b). Also, the ligaments' contribution in limiting the neural soft tissue mobility potentially indicates that the LSO, as the mass-spring-damper system, resets to equilibrium after the oscillation caused by external stimulus.

4.3 Conclusion

Revealed dependency of the soft tissue mobility to pre-tension and amount of acceleration indicates that the denticulate ligament directly influences the dynamic behavior of the soft tissue housed inside the lumbosacral organ. The limiting impact of the denticulate ligament network on soft tissue mobility suggests the mechanosensor system of the LSO resets to equilibrium after the oscillation caused by external stimulus. Establishing a relationship between soft tissue mobility and the pre-tensioning parameter of the denticulate ligaments allows us to assume that the LSO is a strain-sensitive intraspinal mechanosensor acting as an accelerometer or even as a perturbation sensor. The maximal static deflection measured in situ is relatively small, less than 8% out of available space inside the lumbosacral canal, potentially indicating that the available space is reserved for the higher soft tissue deflections that occur in response to a large external acceleration or even perturbation of the bird. If accessory lobes are sensitive enough to detect tiny soft tissue oscillations induced by acceleration, we could consider the LSO as an accelerometer. But if accessory lobes are tolerant to low deflection but tuned to sense perturbation events - the LSO is a perturbation sensor.

Chapter 5

Modeling Avian Lumbosacral Soft Tissue Mechanics

Topic

This project aimed to understand the sensitivity characteristics of oscillating soft tissue under external load, considering the influence of spinal canal morphology. For this purpose, we studied the time and frequency response of biophysical models of different configurations.

Motivation

The scientific literature has previously suggested the connection of lumbosacral anatomical adaptations with the potential function of the intraspinal mechanosensor. Still, the principle and mechanisms explaining the mechanosensory function of the avian lumbosacral organ remain unclear. Besides, the previously suggested hypotheses on the LSO mechanosensory function explain the role of not all unique anatomical features of the soft tissue and the spinal canal as an interacting complex. We established in Chapter 3 the geometric and biomechanics properties that evidence the LSO similar to the fluid-filled mass-spring-damper system. In Chapter 4, we found that LSO soft tissue exhibits minor changes in position and observed previously undocumented details of the denticulate ligament network. However, the currently available functional imaging technologies are limited and do not allow *in vivo* visualization of the behavior of small neural tissue embedded within highly pneumatized fused lumbosacral vertebrae covered by multilayer tissue. This project aimed to quantify the influence of individual anatomical LSO features related to mechanosensing through the time and frequency response of soft tissue to external vibrations. Therefore, we incorporated physical properties of key morphological parameters using soft robotics approaches based on 3D anatomical observations and taking advantage of the configurable modular LSO biophysical model. The custom-designed linear locomotion simulator allowed us to study the mechanical response of the quantitatively replicated LSO.

Synopsis

Recent studies of the morphological and mechanical properties of the unique anatomical features that constitute the LSO have suggested it is a locomotion sensor organ acting similarly to a fluid-filled mass-spring-damper system. Unfortunately, observation of intraspinal oscillations inaccessible so far neither *in vivo* nor even *in situ*. Alternatively, we approached a biophysical simulation. By mimicking the LSO model using soft robotics techniques, we quantified the time and frequency response of the replicated soft tissue on controlled external acceleration. Key morphologies and physical properties established for soft and bone tissue were replicated based on a 3D map of the *Coturnix coturnix* (common quail's) lumbosacral region. The topology of the denticulate ligament network was replicated based on 3D anatomical observation on the *Gallus gallus domesticus* (domestic chicken) lumbosacral region. With our configurable biophysical model, we studied the impact of each anatomical feature that is hypothetically associated with the mechanosensitive function of the LSO under external accelerations produced by the linear oscillation setup. The biophysical simulations supported our hypothesis that unique anatomical features collectively could respond as a mass-spring-damper system on the external entrainment.

5.1 Material and Methods

5.1.1 Biophysical Simulation

The biophysical simulation aimed to infer function (Hutchinson, 2012) from unique morphological features of the LSO, currently inaccessible using *in vivo* or even *in situ* methods. To quantify soft tissue's time and frequency response under locomotion, we developed a configurable LSO biophysical model. Using a custom-built actuated locomotion simulator, we oscillated the model, imitating birds' vertical up-down movements at cursorial locomotion, and measured the soft tissue response to movement. We simplified the complexity of the LSO morphology based on the 3D map of the common quail *(Coturnix coturnix)* lumbosacral region (see Figure 5.1) described in Chapter 3. The LSO was scaled up to make it convenient for fabrication and manipulation using soft-robotic tools. We qualitatively replicated the spinal cord, glycogen body, denticulate ligament network, cerebrospinal fluid, and spinal canal, including semicircular grooves, by maintaining interactions between anatomical features that are hypothesized to be related to mechanosensation. Using a locomotion simulator and a modular LSO biophysical model, we tested seven hypotheses on the mechanosensory function of the unique LSO anatomical features:

1. The soft tissue can be entrained by external oscillations induced by locomotion.

2. High glycogen body density leads to amplification of the spinal cord oscillations.

3. Cerebrospinal fluid dampens soft tissue oscillation amplitudes and reduces spinal cord deflections.

4. The relatively small fluid space between the soft tissue and the spinal canal wall filled with the cerebrospinal fluid causes a damping effect on the oscillation.

5. Transverse semicircular grooves on the dorsal side collectively with an overly developed fluid space resembling a dip on the ventral side of the lumbosacral spinal canal influence the CSF dynamics.

6. The asymmetry between the dorsal and ventral vertical fluid spaces between the soft tissue and the spinal canal walls leads to asymmetric oscillations.

7. The denticulate ligaments supporting the neural soft tissue inside the spinal canal limit the amplitude of the oscillations by increased stiffness and unique network topology.

Simplification and Scaling 3D Anatomy of the LSO

The LSO biophysical model design implements the morphology of the lumbosacral region between vertebrae L4 and S2, i.e., the region of the glycogen body prominence. We simplified the LSO morphology to minimize the number of
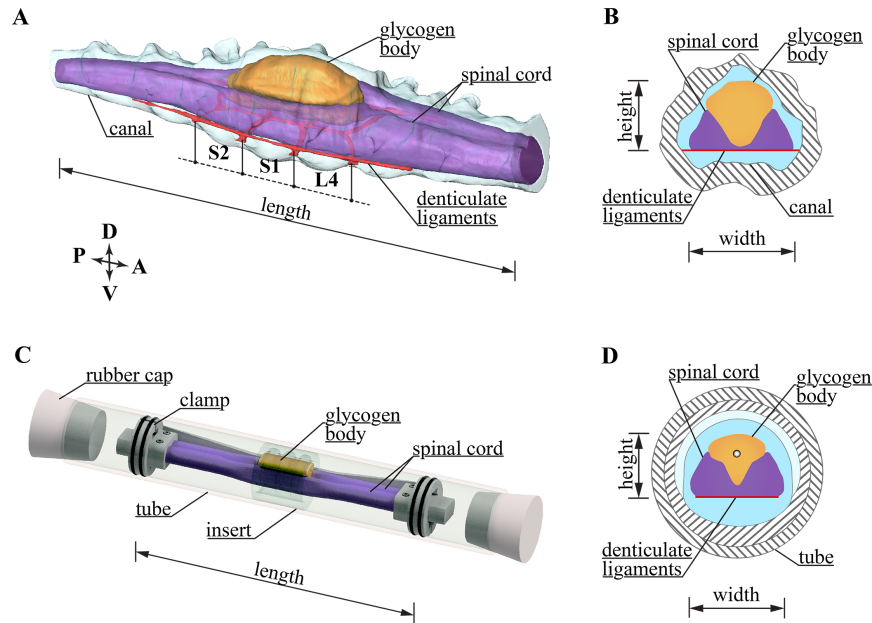
Figure 5.1: Simplification and scaling of the LSO morphology to simulate the soft tissue motion under controlled external acceleration. (A) Oblique view at the lumbosacral region of a 3D common quail model (studied in Chapter 3). All soft and connective tissues are enclosed in an endocast formed in the lumbosacral spinal canal. (B) Anterior view on the schematic transverse section through the lumbosacral canal at the fusion region of the S1 and L4 vertebrae. (C) An oblique view of the LSO biophysical model consists of the spinal cord, glycogen body, and three transverse semicircular grooves in a water-filled glass tube. The ends of the soft tissue are clamped with custom-designed fixtures. (D) Anterior view of the schematic transverse section through the LSO biophysical model at the middle transverse semicircular groove. Image (C) is by An Mo.

physical parameters influencing soft tissue behavior and adjusted material properties to investigate the individual influence of each part. To avoid developing an unreliable LSO biomechanical model that would corrupt the simulation results, we had to follow a balance between realism and reductionism of the morphological parameters (Hutchinson, 2012). The original soft tissue morphology derived from the digital dissection of the quail lumbosacral region (see Chapter 3) was linearly scaled to a good-sized model suitable for fabrication and instrumentation. We implemented morphometric parameters by maintaining a constant volume ratio between the glycogen body, spinal cord, and cerebrospinal fluid (see Table 5.1). The up-scaling of the small-sized anatomical structures resulted in scaling the quail lumbosacral region up to ≈6 times, roughly the size of the ostrich one (Streeter, 1904). Anatomical irregularity and asymmetry were simplified with a parametric design, so the morphology of the LSO biophysical model is similar but not identical to the biological references (see Figure 5.1). We remained only functionally relevant parameters to replicate anatomical features evidencing that the LSO reminisces of a fluid-filled mass-spring-damper system. To characterize the soft tissue response to the external actuation caused by locomotion, we needed to consider the influence of interaction with surrounding cerebrospinal fluid flowing inside the complex shape lumbosacral canal. Therefore, besides the

Table 5.1: Biophysical model design parameters. The parameters of selected anatomical structures were measured in the L4-S2 region. Volume percentages for both the biophysical model and its biological reference are calculated from the sum of selected anatomical structures. The soft tissue parameters of the biological reference common quail model are taken from Chapter 3.

Unit	Parameter	LSO Reference	LSO model
Length [mm]	Width, w	3.5	21
	Length, l	20	140
	Height, h	5.0	30
Volume L4-S2 [mm^3]	Spinal cord, V_{SpC}	25 (36%)	4761 (35%)
	Spinal fluid, V_{CSF}	31 (45%)	6323 (47%)
	Glycogen body, V_{GB}	13 (19%)	2487 (18%)
Density [g/cm^3]	Spinal cord, ρ_{SpC}	1.0	1.0
	Spinal fluid, ρ_{CSF}	1.0	1.0
	Glicogen body, ρ_{GB}	$1.4 - 1.5$	1.0, 1.5, 2.0

soft tissue models, we qualitatively replicated morphological parameters for the spinal canal (see Chapter 3 and the ligaments network topology Chapter 4). We simplified the topology of the three segmentally arranged transverse semi-circular grooves formed at S2-S1, S1-L4, and L4-L3 vertebral fusion to the equidistant parallel identical regular-shaped grooves. The longitudinally oriented sinusoidal dip between the L4 and S2 vertebrae was simplified to a symmetrical longitudinal dip in the ventral part of the canal, extending along the L4-S2 region (see fig. 5.1 C).

Design and Fabrication of the Biophysical Model

We tested various designs, fabrication methods, and materials to implement simplified morphology and biophysical parameters of the lumbosacral organ in the biophysical model. We were selecting materials and fabrication approaches guided by the general tenets of soft robot fabrication (Whitesides, 2018): reproducibility, mimicking the properties of soft tissue as much as possible, and inexpensive. For replicating the simplified morphology of the LSO, we focused on the L4-S2 region. The spinal cord is described in the literature as visco-and poroelastic with very little inherent stiffness (Ramo et al., 2018) but simultaneously a slight stretchability (E. C. Clarke, 2011). To model the behavior of the spinal cord, the surrounding pia-arachnoid complex, which provides stiffness and recovery from stress, has been considered (Ramo et al., 2018). The glycogen body density is higher than the spinal cord and cerebrospinal fluid (based on the literature review in Chapter 3). Therefore, in designing the glycogen body model, we focused on our aim to study how greater-than-buoyant density affects the amplitude of the spinal cord oscillation. This subsection summarized our design experience and described the fabrication details we applied. The first series of prototypes of the LSO model was manufactured directly on a 3D printer (*Carbon M1*). The simplified 3D models of the spinal cord and the glycogen body were modeled as merged empty shells using Autodesk 3Ds MAX software (version
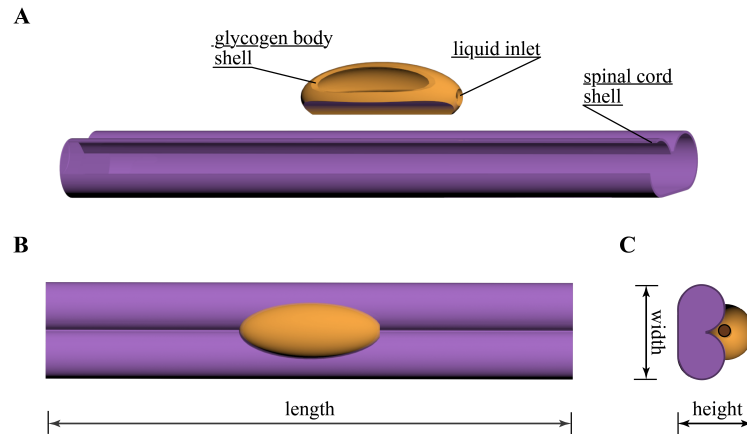
Figure 5.2: LSO model prototype designed as 3D-printed shells. (A) An oblique view of the models of the spinal cord and the glycogen body designed as empty shells. (B) Dorsal and (C) anterior views of assembled LSO soft tissue models.

2021) (see Figure 5.2). The glycogen body model design implied manipulating its mass without affecting the volume by using a liquid of different densities poured through a closable inlet to the model cavity. Using the 3D printing material Silicone (*SIL*) 30, we tested five different wall thicknesses of the shell models: 2.0 mm, 1.5 mm, 1.0 mm, 0.5 mm, 0.4 mm. Nevertheless, the 3D-printed model of the spinal cord retained a rigidity that did not allow us to simulate oscillations that would result from the visco-elastic nerve soft tissue. Therefore, for the next prototyping of the LSO soft tissue, we abandoned the idea of using shells in model design but instead turned to silicone rubber model molding.
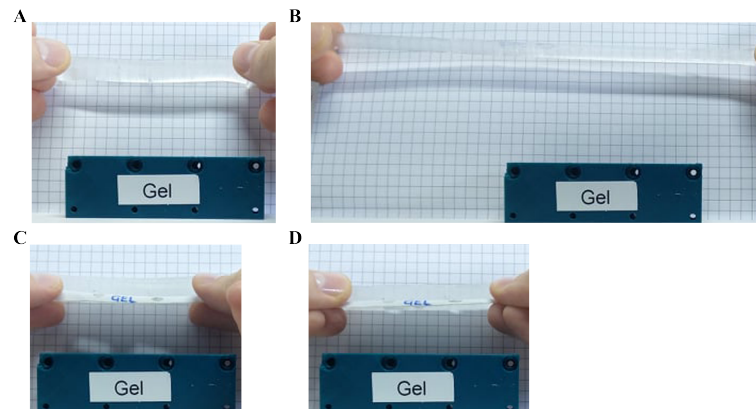
Figure 5.3: Elongation test on spinal cord model with and without reinforcement. As an example of how cloth reinforcement reduces model stretch is shown on the softest silicone rubber we have tested, Ecoflex Gel, *Smooth-On*. The (A) initial length of the pure silicone model can be (B) elongated by 150 %. The (C) initial length of the reinforced silicone model with a microfiber cloth (*MSC-00014-S, Stratasys*) can be elongated by 14 % under a similar stretching force.

We hand-tested the flexibility and extensibility of five hyperelastic silicone rubbers in different hardnesses: *00-50, 00-30* to *00-10*, and *"Gel"* of the Ecoflex™ series. According to the bendability parameters, we chose a super soft silicone

rubber with hardness (*00-10*) to reproduce soft tissue models. Because the pure silicone model elongates by 150 %, we needed to reinforce the spinal cord model to reduce stretchability but preserve bendability. We approached a microfiber cloth (*MSC-00014-S*, *Stratasys*) that affects increasing tensile strength (Hepp and Badri-Spröwitz, 2021) (see Figure 5.3). Reinforcement of the extra-soft silicone rubber with a microfiber fabric substituted for the missing pia-arachnoid complex (Ramo et al., 2018).
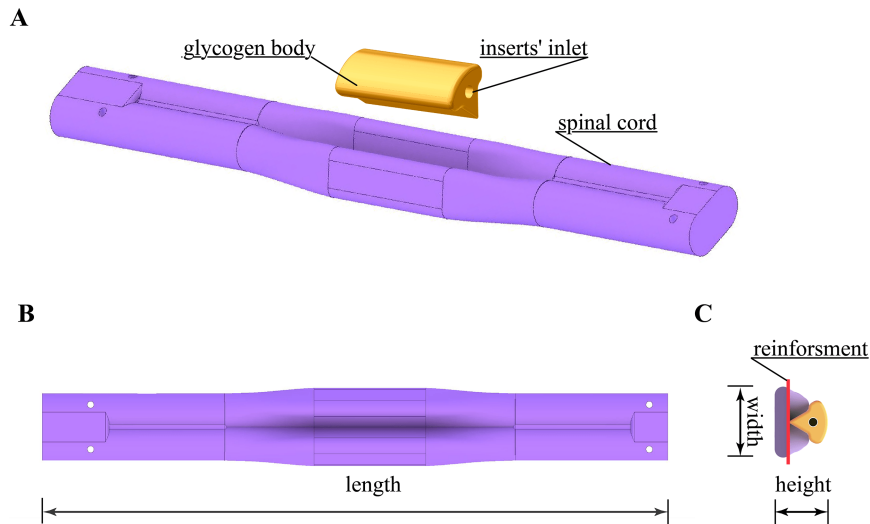
Figure 5.4: Latest generation LSO model designed for silicone molding. The flattened and elongated width of the spinal cord model and the deep placement of the dorsally flattened glycogen body aims to stabilize the dynamics of vertical soft tissue oscillations. (A) An oblique view of the soft tissue-separated models shows design modifications. (B) The dorsal view shows the spinal cord reproduced in natural design considering the glycogen body accommodation between the two hemispheres. (C) The anterior view shows the glycogen body inlet, filled with metal inserts, and the spinal cord reinforcement with the microfiber cloth.

During the pilot tests, we revealed shortcomings in the fabrication approaches and materials used and the shape of the models themselves (see Figure 5.4 A). Hence, we modified the shape of the soft tissue 3D models. The new spinal cord model design consists of two connected parallel cylinders flattened on the ventral side and widened at the glycogen body location region. Between the two hemispheres in the middle on the dorsal side was modeled a groove aimed for mounting the glycogen body model (see Figure 5.4 B). A cross-section of the critical region at the center shows that holds the spinal cord has the shape of two connected triangles (see Figure 5.4 C). The model's cross-sections of two symmetric anterior and posterior endings are two connected circles flattened on the ventral side. The transitions between the three mentioned above critical regions are smooth. An elliptical shape of the glycogen body model was simplified and fitted ventrally to the groove between the hemispheres of the spinal cord. The configurable design of the modular LSO model allowed us to manipulate the glycogen body mass without changing its volume and keep constant parameters of the rest anatomical and biophysical features. We implemented the
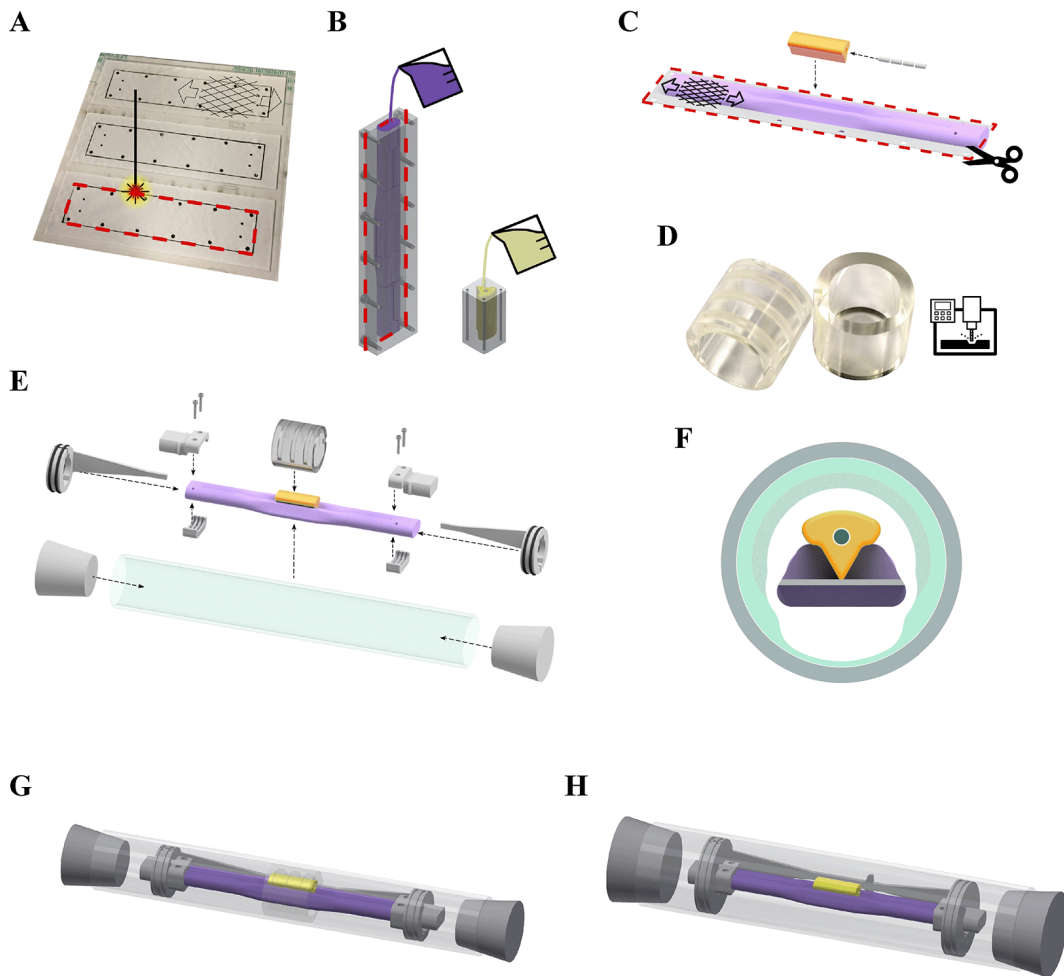
Figure 5.5: The modular lumbosacral organ model fabrication. (A) Laser-cutting microfiber cloth aimed to reinforce the spinal cord model. Arrows indicate the high-stiffness direction of the microfiber cloth; orthogonal is its low-stiffness direction. (B) The spinal cord and glycogen body modeling with silicone rubber (*Ecoflex 00-10*). The microfiber cloth is installed into the spinal cord mold before the silicon pouring. (C) Insertion of aluminum rods into the glycogen body to increase its density. Trimming excess microfiber tissue extruded from the spinal cord model and gluing the glycogen body between its hemispheres. (D) For hypotheses related to the influence of the shape (5) on the soft tissue response, we equipped the LSO model embodied inside a narrow canal with a transparent polymethyl methacrylate (*PMMA*) cylindrical insert with either dorsal semicircular grooves or ventral depression or grooves+depth. (E) Clamps the LSO model's ends with custom-made fixtures and installs an assembled model inside a borosilicate glass tube. (F) Transverse section through the model assembled to test hypothesis 5 using insert with grooves+depth. Oblique view of the LSO biophysical installed inside the (G) narrow and (H) large glass tube canals. All images but (D) are by An Mo.

cylindrical hole throughout the entire model length to manipulate the glycogen body mass without affecting model volume and shape (see Figure 5.4 A and C). We inserted separate equal spaces of aluminum rods, allowing for preserving a bendable glycogen body. Adjusted glycogen body densities of ($1.46\,\mathrm{g/cm^3}$) and

$(2.00\,\text{g/cm}^3)$ were calculated according to the equation:

$$\begin{cases} V_{\text{GB}} = V_{\text{SR}} + V_{\text{AL}} \\ \rho_{\text{GB}}V_{\text{GB}} = \rho_{\text{SR}}V_{\text{SR}} + \rho_{\text{AL}}V_{\text{AL}} \end{cases} \tag{5.1}$$

Where ρ_{SR} and ρ_{AL} are the density of silicone rubber $(1.04\,\text{g/cm}^3)$ and aluminum $(2.71\,\text{g/cm}^3)$, respectively. V_{SR} and V_{AL} are the volume of the silicone rubber structure and the aluminum rod, respectively. By inserting aluminum rods inside the hole, it was accomplished to achieve the reference $(1.46\,\text{g/cm}^3)$, lighter $(1.06\,\text{g/cm}^3)$, and heavier $(2.00\,\text{g/cm}^3)$ configurations of the glycogen body model.

Based on the new design of the soft tissue models, we developed molds using Autodesk AutoCAD (2018 version) and 3D-printed from polylactic acid (PLA) using standard fused deposition model printers (FDM, *Stratasys Fortus 450mc* and *Prusa i3 MK3S*). The inner surfaces of the molds were processed with a
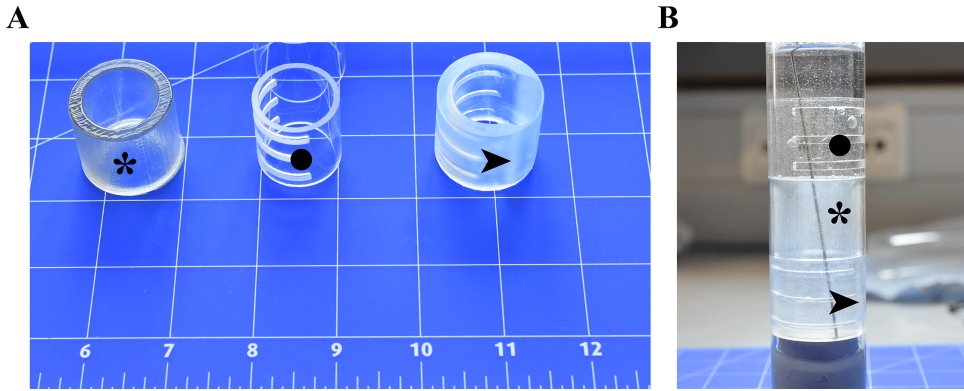
Figure 5.6: Evaluation of material transparency for insert fabrication. Evaluation of transparency in (A) air and (B) water showed that the glass insert ($\bullet$) is the most transparent yet hard reproducibility. 3D printing of epoxy resin is the least transparent insert ($*$) out of testing. The PMMA-made insert ($\succ$) that required manual carving was chosen for further experiments as most optimal by transparency and reproducibility. Photos are by An Mo

release agent (Ease Release 200, *Smooth-On*). For the spinal cord reinforcement, the microfiber cloth was preliminary laser-cut (PLS6 150D, *Universal Laser Systems*) following the mold outlines and then was mounted between dorsal and ventral parts of the assembled mold (see Figure 5.5 A). The degassed silicone rubber was poured into both assembled molds and left to cure (see Figure 5.5 B). To provide visual contrast to the glycogen body model, we added yellow pigment (Silc Pig, *Smooth-On*) to the uncured silicone rubber before pouring. After releasing the spinal cord model from the mold (see Figure 5.5C), we manually trimmed the protruding microfiber tissue from the side edges of the already polymerized silicone. Under the tested hypothesis, aluminum rods were inserted inside the model to increase the density of the glycogen body. At the final fabrication step, we glued the ventral side of the glycogen body model into the gutter between two hemispheres of the spinal; cord model using silicone glue (Sil-Poxy).

To evaluate the effect of the canal morphology on the soft tissue response, we designed four configurations of the insert: the reference one contains both grooves and dip, and two other inserts that individually include grooves, dip, and one insert without any shapes on the inner wall. We looked for an optically transparent material to track the soft tissue model oscillation during the locomotion simulation. We tested three different materials and their surface processing methods to fabricate the inserts: 3D printing of epoxy resin, manual glass-blowing, and carving into the transparent polymethyl methacrylate (PMMA) (see Figure 5.6). The inserts made of PMMA were designed for the narrow canal with an inner diameter of 34 mm (see Figure 5.5 D). The inner diameter of the narrow canal with a plugged-in insert reduces its size further to 24 mm. To control the position and tension applied to the spinal cord model mounted inside the different sizes and modifications of the glass tubes, we approached the custom-designed 3D-printed PLA clamps. For model 9, we developed a rigid frame constituting the left and right lateral and ventral longitudinal 3D-printed PLA clamps to fix the denticulate ligament network rigidly.

Locomotion Simulation Linear Set-up

The custom-design actuated locomotion simulator is approached to simulate the up-down movements produced by birds during terrestrial locomotion (see Figure 5.7). Janet Hauptmann (Richter), 2018, an undergraduate student at DLG, worked on building this simulator. An Mo, a doctoral student at DLG, extended it. The 20 mm plywood setup is a linear vertically installed table
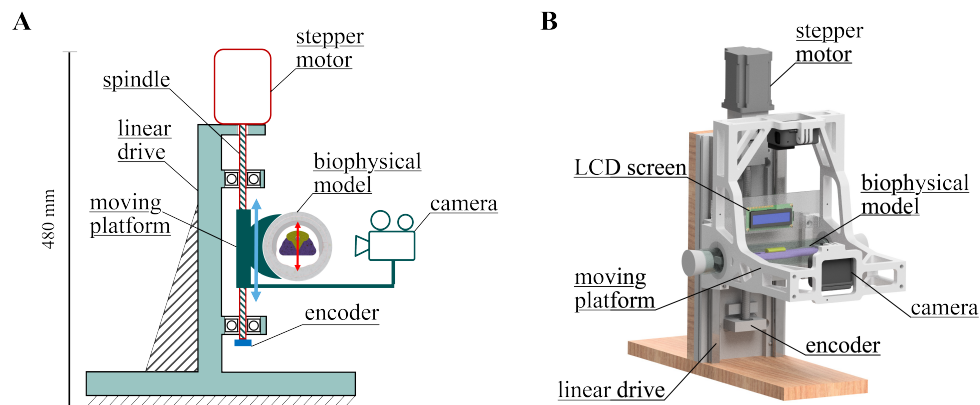
Figure 5.7: The actuated locomotion simulator. (A) schematic and (B) 3D rendering, is shown in assembled state. A mounted at the moving platform camera measures the LSO biophysical model response (red arrow). The encoder registers the position of the spindle (blue arrow), which moves vertically with a slider driven by a stepper motor. Video recordings and encoder data are synchronized using the LCD screen. Images are by An Mo.

with a support construction. On the vertically oriented spindle is a movable 3D-printed PLA platform on which the biophysical models are to be tested and the video camera (Hero 5 Black, *GoPro*). The controlled vertical oscillations of the platform were generated by a linear drive (KUHC1205-340-100, *MISUMI*) through a stepper motor (103H7823-1740, *Sanyo Denki*) and a spindle. A spindle

rotation and pitch result in the linear slider displacement along the vertical linear drive. The spindle rotations were counted by the rotary encoder (AS5045, *AMS*) and sampled by a single board computer (Raspberry Pi, v. 4B), with 10 μm resolution at 2 kHz update frequency. The stepper motor driver is controlled by a microcontroller (Teensy 4.0, *PJRC*). Information about the status of the locomotive simulator is displayed on the LCD screen.

Collecting and Analyzing Data

We assembled eight models of the LSO varying depending on the tested parameter. The reference version of the biophysical LSO model replicates morphological and biomechanical properties relevant to the LSO potential mechanosensing functions described in Chapter 3. It consists of the spinal cord combined with the longitudinal ligaments and the glycogen body, mounted inside the water-filled narrow glass tube equipped with a "grooves+dip" insert. The Mass of the glycogen body, size and shape of the canal, and soft tissue position inside the glass tube are modular. The parameters of the spinal cord reinforced with the longitudinal ligaments were constant throughout all experiments. The biophysical simulation for testing all hypotheses follows an identical protocol. We had to remove the maximal possible air bubbles from seven models filled with water to reduce the noise they could produce during model oscillation. We
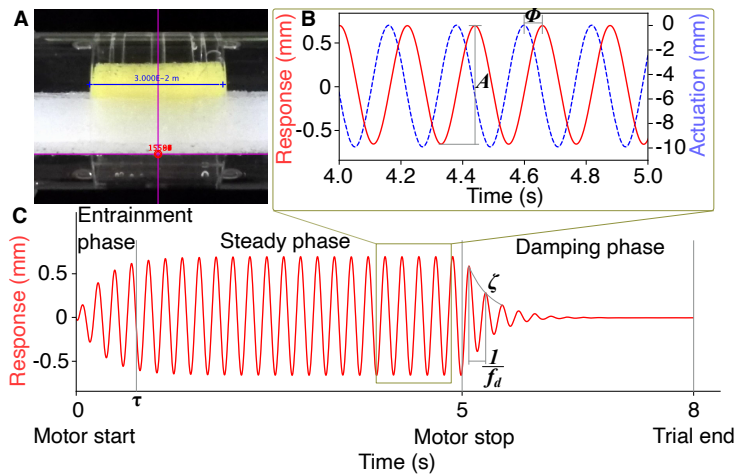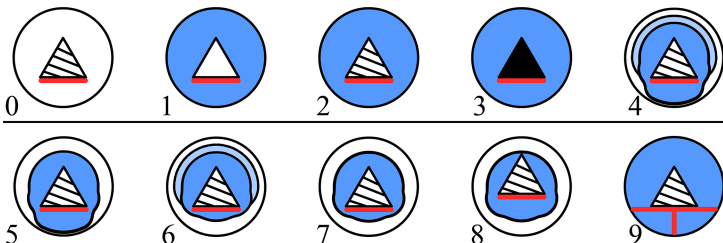
Figure 5.8: Typical model response to external motion. The data shown is extracted from trial 1, model 2, at 4.5 Hz external oscillation frequency. Each experiment shows three phases; The **entrainment phase**, with a settling time τ spanning from start until the model reaches 90 % of the steady state amplitude. In the **steady phase** we measure the model's peak-to-peak amplitude A, and the phase shift ϕ between the external actuation and the model's response. The **damping phase** starts when the motor is switched off (5 s). We calculate the model's decay rate ζ and the damped oscillation frequency f_{d}. Image and plots are by An Mo

fully immersed glass tubes with preliminary installed soft tissue models into the water, manually removed accumulated air bubbles, and closed tubes with rubber caps on both sides. We have pierced through a rubber cap with a medical needle opening an outlet to remove some remaining air and water excess, which prevents the tube from closing. Each LSO model was mounted and tightly fixed

inside a 3D-printed PLA platform attached to the locomotion simulator. On the opposite side of the platform is a lightweight, compact video camera (Hero 5 Black, GoPro).

Table 5.2: Schematic representation of the LSO biophysical models. Circles represent cross-sections through the middle glass tubes; a blue color illustrates a water-filled fluid space; a white color illustrates an air-filled fluid space. Contours within the circle represent inserts that modify the internal shape of canals. Different fill of triangles represents varying density glycogen body (ρ_{GB}). "Grooves" is an insert with three transverse semi-circular grooves parallel to each other equidistantly located on the dorsal side inside the canal. "Dip" is an insert with a single longitudinally oriented groove on the ventral canal inside. "Grooves+dip" is an insert that combines "dip" and "grooves." "Uniform" is an insert for decreasing a canal size with no shape affecting it. All inserts are developed and used only for models with narrow canals. Data in the table and models' logos are by Dr. Fernanda Bribiesca-Contreras with support by An Mo.

Model #	Canal	Diameter [g/cm³]	ρ_{GB} [mm]	Notes
0	large	51	1.5	in air
1	large	51	1.0	
2	large	51	1.5	
3	large	51	2.0	
4	narrow	24	1.5	grooves+dip
5	narrow	24	1.5	dip
6	narrow	24	1.5.	grooves
7	narrow	24	1.5.	regular insert
8	narrow	24	1.5	shift up
9	large	51	1.5	ligaments

For each LSO model, the actuated locomotion simulator is driven in a vertical oscillation with an amplitude of $\pm 5\,$mm. Each tested model was driven 8 times at four frequencies: 3.0, 3.5, 4.0 and 4.5 Hz. The motor driver (G201X, *geckodrive*) controls the stepper motor in micro-step mode and tracks the sine motion (see Figure 5.8 B, dashed blue line). Soft tissue oscillations in response to locomotor simulator actuation were recorded with the compact video camera (Hero 5 Black, *GoPro*) at a sampling frequency of 240 Hz (see Figure 5.8 B, solid red line). Before the multiple sampling step of the recorded data, we eliminated the source of measurement error generated by the GoPro camera through the fisheye effect. We removed the distortion caused by the camera lens using the "Single Camera Calibrator App" (Matlab, MathWorks, Natick, MA). The further data processing step was determining the amplitude of the soft tissue by tracking position its position relative to local coordinates. Using free video analysis and

modeling tool Tracker (Software, n.d.), we follow the ventral side edge of the spinal cord at a point vertically aligned with the center of the glycogen body model length on preliminary cropped and contrast-enhancing filtered video data (see Figure 5.8 A). The next step after data extraction was filtering using the 4th-order zero-lag Butterworth filter (cutoff frequency 9 Hz). Then filtered data were interpolated in Matlab, where we divided the soft tissue oscillation data into three phases. The first one is Entrainment phase A with settling time τ from the start of the switched-on motor till the second steady phase B with peak-to-peak amplitude A, phase shift ϕ, asymmetry ratio β. A stable swinging characterizes the steady-state phase without damping or at least the damped swinging. The last is the damping phase C with decay rate ζ, damped oscillation frequency f_d. To synchronize the data flow on the simulator motor actuation collected by the motor driver and the LSO model response recorded with the camera, we used the LCD to display the state of the simulator mode.The LCD was mounted so that it was in focus with the camera lens pointed at the lateral side of the LSO model. To evaluate the dependence of the soft tissue's time and frequency response on the morphological parameter being tested during external acceleration, we are analyzing three phases of the soft tissue oscillations: entrainment, steady, and damping (see Figure 5.8).

According to the values of the model oscillations phases, we test our seven hypotheses on the LSO anatomical features mechanosensing related functions (see Table 5.2). We evaluate the influence of the studied parameter on the LSO soft tissue behavior under external actuation:

1. The LSO soft tissue oscillates under the dynamic entrainment of birds' locomotion is tracing on a steady-state phase on all models without ligaments (0-8). We expect to observe a soft tissue response to external rhythmic excitation with rhythmic oscillations.

2. The larger-than-buoyant glycogen body density amplifying the soft tissue oscillation is studied on amplitude response and settling time. Assuming the amplitude of soft tissue oscillations increases with a glycogen body density, we compare the soft tissue response of three LSO models (1-3) differently by the GB mass configuration.

3. The cerebrospinal fluid damping the soft tissue oscillation amplitudes and reducing spinal cord deflections is tested on amplitude response and decay rate. We compare two LSO models mounted inside a large glass tube, identical in soft tissue parameters but different in filling: water (2) and air (0).

4. The small space between the soft tissue and the walls of the lumbosacral spinal canal filled with cerebrospinal fluid causes a damping effect on oscillations is examined by the settling time and decay rate. We compare the behavior of identical soft tissue models mounted inside large (2) and narrow (7) glass tubes.

5. The semicircular grooves on the dorsal side of the lumbosacral canal and dip under the spinal cord affect flow resistance is examined on the soft

tissue oscillation amplitude and decay rate. We compare four different inserts configurations replicating the spinal canal morphology between L4-S2 vertebrae: "groove+dip" (4) as the reference; only "dip" (5); only "groove" (6); without any canal shaping (7).

6. The asymmetry of the vertical fluid space between the soft tissue and the spinal canal walls leads to asymmetric oscillations is tested on the model's amplitude asymmetry ratio. We compared the oscillations of the LSO model, in which the soft tissue is mounted inside a narrow glass tube centrally (7), with an identical LSO model but shifted dorsally (8).

7. The network of dentate ligaments, described in vertebrates as rigid connective tissue stabilizing the spinal cord, coupled with unique avian topology, restrains putative soft tissue vibrations within the lumbosacral canal. The restraining function is tested on the soft tissue oscillation amplitude at the steady phase. We compared models with (9) and without (2) denticulate ligament network under the spinal cord mounted inside the large glass tubes.

The data obtained were processed in Python v. 3.8 (Python.org, n.d.) by Dr. Fernanda Bribieska-Contreras, with support from An Mo. The analysis showed that the oscillation of the models in all tests was stable. We calculated the amplitude of soft tissue oscillations inside the glass tubes entrained by external oscillations. We applied filtering to analyze the data extracted from different test sessions of mechanical simulations using different parameter LSO models. For this aim, the consecutive positive and negative peaks between 3.0 and 4.8 s were subtracted from the settling phase of each analyzed LSO model.

5.2   Results and Discussion

The biophysical simulation of the LSO response on the birds' locomotion was limited to up-or-down movement. But, even under the limits of the locomotion simulation and the LSO morphology simplification, we get the results that show the mechanics happening inside the micro-fluid environment are likely more complex than we initially expected. Vertical spinal cord movements produce drag force opposing the original fluid movements. The fluid dynamics revealed dependency on the canal morphology. Viscoelastic silicone rubber reinforced with microfiber tissue that retains the elasticity necessary to simulate spinal cord behavior, combined with the modular design of the LSO model, allowed us to test our seven hypotheses (see Table 5.3) we put to the anatomical structures with potential relation to the mechanosensitive function.

Table 5.3: Hypotheses test using 9 LSO models with controlled variables.

Hypothesis	Model #	Controlled variable
1	0 - 8	$\sim$
2	1 - 3	Density
3	0, 2	Fluid type
4	2, 7	Canal size
5	4 - 7	Canal morphology
6	7, 8	Soft tissue location
7	2, 9	Ligament network

5.2.1   Spinal Fluid Damping Effect

We compared the LSO biophysical models filled with water (2) and air (0) to test our assumption that the CSF causes a damping effect on the neural soft tissue within the lumbosacral spinal canal. Water, which is identical to CSF in viscosity (Bloomfield et al., 1998), exerts more resistance than air (Rumble, 2021), which explains a reduction of the soft tissue oscillation amplitude and production of a high damping effect for the water-filled model 2 comparative to the air-filled model 0. Analysis revealed that the peak-to-peak amplitude measured in the air-filled model 0 was significantly higher (t-test; p values $<1 \times 10^{-4}$)) than for the water-filled model 2 for all tested drive frequencies. A peak-to-peak amplitude revealed direct dependency on drive frequencies for both fluid types. The in-air-filled model 0 produced a stronger amplitude with values ranging from $0.85\,\mathrm{mm}$ to $2.41\,\mathrm{mm}$ than the water-filled 2 model with values ranging from $0.13\,\mathrm{mm}$ to $1.33\,\mathrm{mm}$ (see fig. 5.9 A). The small peak-to-peak amplitude in water can indicate the association with the CSF cushion function (Eklund et al., 2007) as vital in protecting the spinal cord during the oscillation induced by locomotion from damage that could be caused by excessive strain and impact on the spinal canal walls.

Settling times for all drive frequencies in the soft tissue oscillations significantly
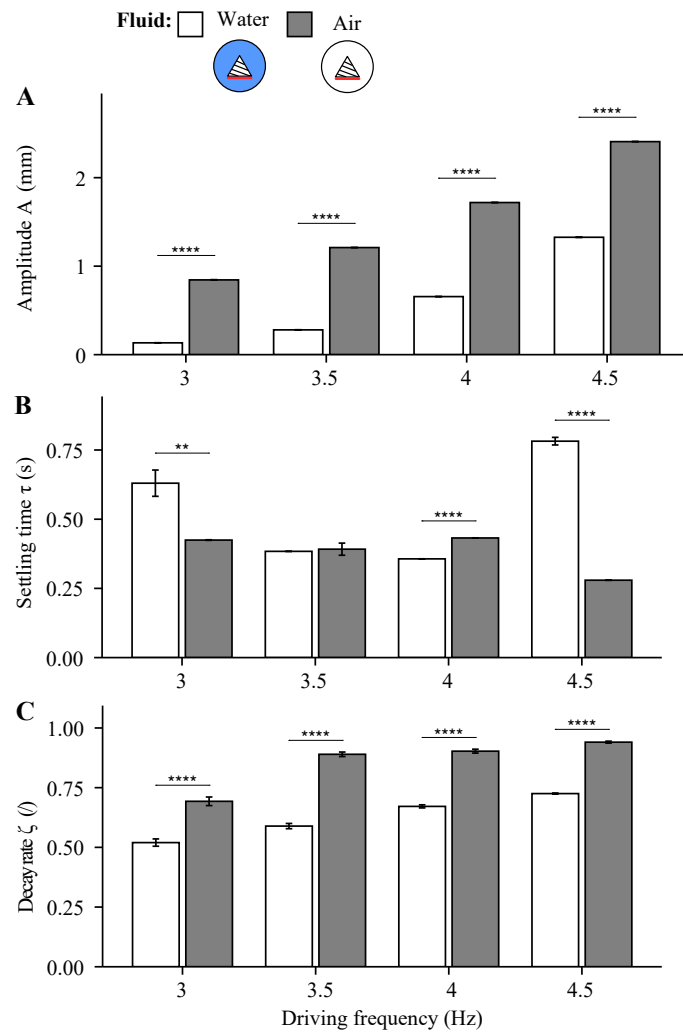
Figure 5.9: Effect of fluid on time and amplitude of the soft tissue oscillations. Evaluation of the water-fluid versus air-fluid effect on the soft tissue oscillations at four different drive frequencies on mean peak-to-peak (A), settling time (B), and decay rate (C). Data are shown for eight trials at 3.0, 3.5, 4.0, and 4.5 Hz for model 2 (water) and model 0 (air). The standard error is shown as an error bar, significant p-values from t-test pairwise comparisons as: "****" for 0; "***" for 0-0.001; "**" for 0.001-0.01; "*" for 0.1-0.05. Error bars are absent if the standard error is smaller than the measurement resolution. The plots are by Dr. Fernanda Bribiesca-Contreras with support by An Mo.

differed between the air-filled model 0 and water-filled model 2, with values ranging from 0.36 s to 0.78 s, except for 3.5 Hz (t-test; p values <0.001). However, we did not find a pattern of changing the soft tissue oscillation settling time from an increase in the drive frequency (see Figure 5.9 B).

The decay rate comparative analysis for the water (2) and air (0) fluids revealed significant differences (t-test; p values $<1 \times 10^{-4}$) and showed an opposite result to what we expected. We revealed that the decay rate of the model oscillation in the water (2) varying from 0.52 to 0.73 was lower than in air-filled model 0, where the decay rate was from 0.69 to 0.94 (see Figure 5.9 C). The non-intuitive

result that the model in air resets on the system with a higher decay rate than in water needs more investigation. Still, for the current step, we can explain this effect by the complexity of the multi-component LSO system formed by hard, soft, and connective tissue, which complimentary affect fluid dynamics. Also, we assume that evaluation of the LSO system requires considering the additional buoyant force, which alters the mass, stiffness, and damping of the system altogether.

5.2.2 Glycogen Body Amplifier

Anatomical and physical features of the high-density glycogen body surrounded by a fluid-filled, overly developed, expanded lumbosacral canal suggest that the glycogen body acts as an amplifier for the putative spinal cord oscillations. We tested our assumption by comparing a neutrally buoyant glycogen body and glycogen bodies of different densities that exceed the spinal cord and cerebrospinal fluid (see Table 5.1). Measurements of the soft tissue model oscillations amplitude (see fig. 5.10 A) and settling time (see fig. 5.10 B) allowed us to gather evidence supporting our assumption that the glycogen body, which exceeds the density of the surrounding cerebrospinal fluid, is involved in fine-tuning the soft tissue oscillations inside the lumbosacral canal. The peak-to-peak amplitude of soft tissue oscillations in the steady phase (see Figure 5.8) increases with a glycogen body density and drive frequency. The statistical analysis revealed that amplitude significantly differs for all four tested drive frequencies between the compared models 1, 2, and 3 of different glycogen body densities (t-test; p values $<1 \times 10^{-4}$). Within the range of drive frequencies from 3 Hz to 4 Hz, the peak-to-peak amplitude directly depends on the glycogen body density. However, the exception was discovered at 4.5 Hz when model 2 with a glycogen body density of $1.5 \, \text{g/cm}^3$, showed a higher amplitude of 1.33 mm than model 3 with a higher glycogen body density of $2.0 \, \text{g/cm}^3$. This effect potentially indicates that the LSO multi-component system is tuned to protect the oscillating soft tissue from potential damage from jerks caused by rapidly increasing vertical acceleration during aggressive locomotion, perturbation, or rapid takeoff (Daley, Channon, et al., 2016; Henry et al., 2005). Some current investigations assume that the LSO anatomical features adapt and correlate with locomotor modality in avians (Kamska, Contreras, et al., 2021; Stanchak, French, et al., 2020), which potentially indicates that the glycogen body density varies depending on locomotion modalities. We can assume birds that experience high vertical acceleration during locomotor movements develop a relatively low-density glycogen body. A settling time by representing how the speed of models' response to external oscillation gave us intuition about the dependency of the LSO model sensitivity on the glycogen body density. The settling time showed no linear relation to the drive frequency for all tested glycogen body densities implemented with the LSO models 1, 2, and 3 (see Figure 5.10 B). The damped oscillation frequency analysis gives some pieces of evidence that the LSO likely acts as a mass-spring system. Despite model 1 of the neutrally buoyant glycogen body ($1.0 \, \text{g/cm}^3$) and model 2 of the glycogen body ($1.5 \, \text{g/cm}^3$) exceeding the spinal cord demonstrates equal damped oscillation frequencies - the model 3
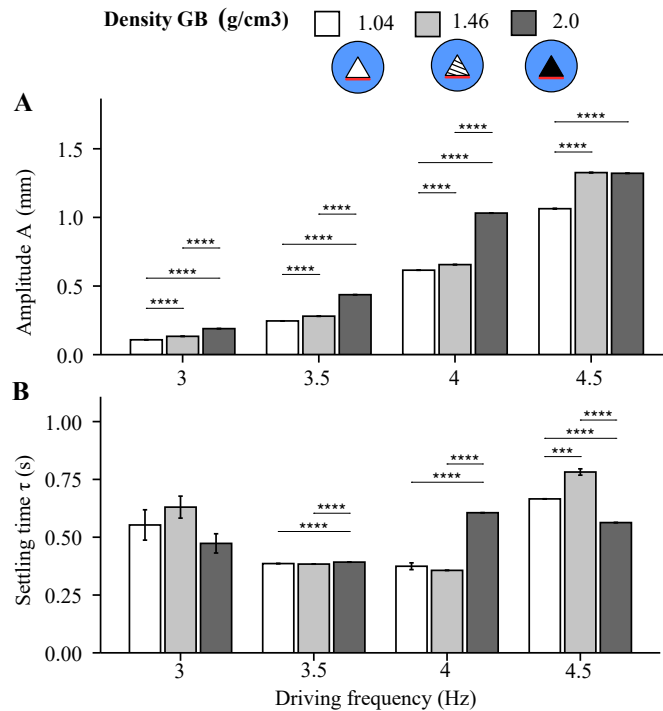
Figure 5.10: Effect of glycogen body density on soft tissue oscillation. Influence of glycogen body density and drive frequency on mean values of peak to peak (A) and settling time (B). Values shown are for models 1, 2, and 3 with the density of 1.0, 1.5, and $2.0\,\text{g/cm}^3$, respectively. Drive frequencies tested were 3.0, 3.5, 4.0 and 4.5 Hz. The standard error is shown as an error bar, significant p-values from t-test pairwise comparisons as: "****" for 0; "***" for 0-0.001; "**" for 0.001-0.01; "*" for 0.1-0.05. Error bars are absent if the standard error is smaller than the measurement resolution. The plots are by Dr. Fernanda Bribiesca-Contreras with support by An Mo.

with a density exceeding model 2 by $0.5\,\text{g/cm}^3$ demonstrates a slight reduction of damped oscillation frequency (see Table 5.4). Summarizing test results, we can assume that glycogen body density can balance a multi-component system between rapid soft tissue response to external acceleration and tissue protection from potentially concomitant deformation.

5.2.3 Canal Morphology Influence on Fluid Dynamics

The spinal canal is a closed volumetric space limited for the CSF circulation through the subarachnoid space by the movable arachnoidal trabeculae surrounding the neural soft tissue inside the spinal canal (Battal et al., 2011; Necker, 2005). However, avian-specific transverse semi-circular grooves and ventral dip of the lumbosacral canal, possibly acting as fluid flow relieves canals, indicate the possibility of laminar and pulsatile flow around the neural soft tissue (Kamska, Daley, et al., 2020; Necker, 2005; Necker et al., 2000; Stanchak, French, et al., 2020). The spinal canal morphology affects the dynamics of the CSF, which determines the strength of the circulating flow affecting the neural soft tissue inside the canal (Kim et al., 2021). In a closed system, the orientation of the
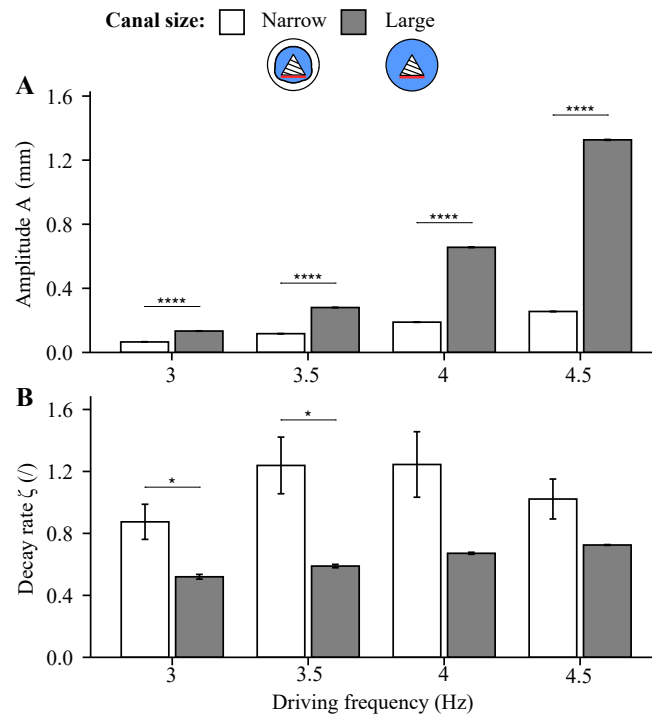
Figure 5.11: Effect of lumbosacral canal size on soft tissue behavior. Evaluation of the canal size affects mean values of peak-to-peak (A) and decay rate (B) under four different drive frequencies. Data are shown for eight trials at 3.0, 3.5, 4.0, and 4.5 Hz for model 7 with a narrow-size and model 2 with a large-size canal. The standard error is shown as an error bar, significant p-values from t-test pairwise comparisons as: "****" for 0; "***" for 0-0.001; "**" for 0.001-0.01; "*" for 0.1-0.05. Error bars are absent if the standard error is smaller than the measurement resolution. Error bars are absent if the standard error is smaller than the measurement resolution. The plots are by Dr. Fernanda Bribiesca-Contreras with support by An Mo.

fluid in interaction with the deformable soft tissue can change relative to the flow and movement of the spinal cord, resulting in a change in the fluid forces acting on the surface of the structure, equivalently the amount of displaced cerebrospinal fluid (Gomes and Lienhart, 2013). Hence, fluid-structure interactions between the CSF with the inner wall of the spinal canal and the neural soft tissue housed inside create a micro-fluid environment in which fluid movements and soft tissue behavior are dependent on each other (Gomes, 2012). With decreasing the CSF space, fluid resistance increases (Battal et al., 2011), slowing the flow and consequently can dampen putative soft tissue oscillations. The comparative analysis confirmed our intuitive expectations by revealing that the peak-to-peak amplitude in the "narrow" spinal canal is smaller, and the damping rate is higher than in the "large" canal (see Figure 5.11). For both size canals, the peak-to-peak oscillations amplitude increase with drive frequency. At the maximum tested drive frequency of 4.5 Hz, the soft tissue amplitude inside the large canal of model 2 was 1.33 mm; for comparison, in the narrow canal of model 7, the highest peak-to-peak amplitude was 0.26 mm (t-test; p values $<1 \times 10^{-4}$) (see Figure 5.11 A). As expected, the decay rate in the narrow canal of model 2 was higher than in the large canal of model 7 (see Figure 5.11 B).

The damping ratio increased linearly inside the large canal, so the maximum decay rate ζ of 0.73 was recorded at 4.5 Hz. In contrast, the maximal decay rate inside the narrow canal of the model (2) does not show a relation with the drive frequency but varies between 0.88 to 1.25. The comparative analysis showed that the difference was only significant at 3.0 Hz and 3.5 Hz (t-test; p values <0.05).

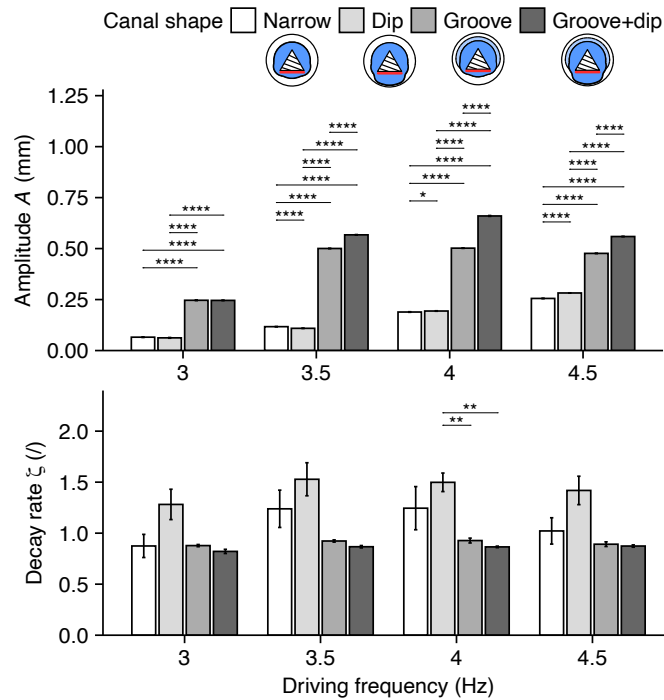To assess the effect of the lumbosacral canal shape on the soft tissue behavior

Figure 5.12: Effect of lumbosacral canal morphology on soft tissue behavior. Evaluation of the canal shape effect conducted under four different drive frequencies on mean values of peak-to-peak (A) and decay rate (B). Data are shown for eight trials at 3.0, 3.5, 4.0, and 4.5 Hz for model 7 with a narrow canal, model 5 with a ventral dip, model 6 with a dorsal groove and model 4 with groove+dip. The standard error is shown as an error bar, significant p-values from t-test pairwise comparisons as: "****" for 0; "***" for 0-0.001; "**" for 0.001-0.01; "*" for 0.1-0.05. Error bars are absent if the standard error is smaller than the measurement resolution. Error bars are missing if the standard error is smaller than the measurement resolution. The plots are by Dr. Fernanda Bribiesca-Contreras with support by An Mo.

under external acceleration, inserts replicating simplified dorsal and ventral canal features in combination and separately were implemented. We assume that a dip on the ventral side and transverse grooves on the dorsal side of the canal act as flow relieves, reducing the resistance to fluid flow by increasing the space (Battal et al., 2011). Model 5 implementing the ventral dip evidences our assumption with higher peak-to-peak oscillation amplitudes than the narrow canal model 7 with a regular shape insert. However, at the maximum tested drive frequency of 4.5 Hz, models 5 and 7 oscillate at similar amplitudes. Higher oscillation amplitudes ranging from 0.25 mm to 0.5 mm were demonstrated by model 4, containing transverse grooves on the dorsal side. Model 6 implementing

a complete set of lumbosacral canal features by combining the simplified grooves and dip resulted in the largest peak-to-peak amplitude ranging from 0.25 mm to 0.66 mm. Based on the results, we could assume that the grooves and dip contribute to the fluid flow-resistant reduction. However, the decay rate analysis evidences that the combination of the canal morphological features affects the CSF dynamics in a more complex way. Model 6, combining both the grooves and the dip resulted in the smallest decay rate among all models tested canal shapes versions. The highest decay rate between 1.28 to 1.53 resulted from model 5 implementing only the dip. It can be assumed that the dip located under the spinal cord, loaded with a high-density glycogen body, influences the CSF dynamics in a certain way, causing the cushion-like damp effect. The statistical analysis showed that the decay rate for the regular narrow canal model 7 and the narrow canal with the ventral dip model 5 showed relatively large standard errors because of the comparatively lower signal quality. The significant difference in the decay rate was revealed only at 4.0 Hz for compared model 5 containing ventral dip to model 4 containing grooves and to model 6 combining grooves and dip (*t*-test; *p* values <0.05). By assessing the results on the simplified LSO models, we couldn't evaluate the whole complexity of the CSF dynamics inside the lumbosacral canal since the insert used for the canal shape modifications covers only the glycogen body location region. Moreover, our models are missing the arachnoidal trabecles affecting the CSF movement by filling the spinal canal space from the lateral edge of the spinal cord to the canal walls (Battal et al., 2011; McCormick and Stein, 1990; Necker, 2005).

5.2.4   Soft Tissue Asymmetrical Position Impact on their Behavior

The digital dissection of the lumbosacral canal of the common quail (described in Chapter 3) and domestic chicken (described in Chapter 4) revealed that the soft tissue proximity relative to the dorsal and ventral spinal canal walls is asymmetrical. The vertical fluid space between the spinal cord and ventral canal wall is larger than the space between the glycogen body and the dorsal canal wall. In addition, we should note that the vertical spaces are distorted by processing both samples with fixative and iodine-based staining chemicals that cause soft tissue shrinkage (Gignac and Kley, 2014; Metscher, 2009b). Most likely *In vivo* measurements of a dorsal vertical distance between the glycogen body and the canal will show even smaller than the ventral vertical fluid space. In contrast to the dorsal vertical space - the space under the spinal cord is less affected by the chemical treatment because it is determined by the level of the horizontal attachment of the denticulate ligaments network supporting the soft tissue. The morphological observation of vertical fluid space asymmetry suggested the resonance suppression effect (Goel, 2005), which might lead to the soft tissue's asymmetric oscillations. Comparing model 8 with the soft tissue shifted toward the dorsal side of the canal with model 7, with the centered soft tissue revealed the opposite result to our expectation (see Figure 5.13). Model 8, which shifted the soft tissue dorsally by 1 mm, did not show a notable asymmetry in the steady-state phase. A maximum asymmetry ratio from model 8 is 0.85
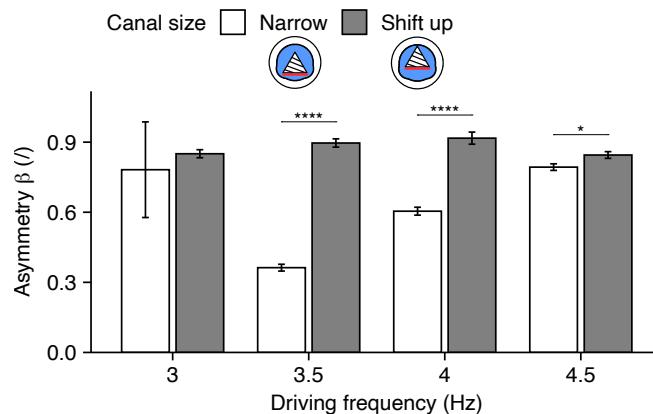
Figure 5.13: Effect of soft tissue position within the spinal canal on their behavior. Evaluation of the soft tissue position influence under four different drive frequencies on mean values of asymmetry ratio. Data are shown for eight trials at 3.0, 3.5, 4.0 and 4.5 Hz for model (7) with the central position for the soft tissues vs. model (8) with shifted-up soft tissue. The standard error is shown as an error bar, significant p-values from t-test pairwise comparisons as: "****" for 0; "***" for 0-0.001; "**" for 0.001-0.01; "*" for 0.1-0.05. Error bars are absent if the standard error is smaller than the measurement resolution. The plot is by Dr. Fernanda Bribiesca-Contreras with support by An Mo.

at a drive frequency of 4.5 Hz. In contrast, the centered soft tissue of model 7 showed the highest asymmetry ratio relative to all tested LSO models, with values between 0.79 to 0.36 Different LSO model configurations with centered soft tissue, including model 9, which contains the denticulate ligaments network, show no notable asymmetrical oscillation (see Table 5.4).

5.2.5   Ligaments Limit Oscillation

We implemented the denticulate ligament network of the horizontal and vertical parts we observed in the chicken sample (see Chapter 4) in model 9 to test our assumption on the ligaments' limiting effect on the soft tissue oscillations. Currently, there are no descriptions of avian denticulate ligaments' mechanical properties in the literature, so we replicated the simplified topology quantitatively following our own haptic experience earned at the classical dissection routine. We should note that modeled ligaments, likewise soft tissue models, are stiffer than biological tissue. The analysis of the soft tissue vertical oscillations at an identical external drive frequency of 4.5 Hz resulted in model 9 with 0.16 mm of maximum peak-to-peak amplitude oscillating over 8x less than model 2 with 1.33 mm of maximal amplitude (see Figure 5.14). Because of technical limitations, our mechanical simulator produces a maximum peak-to-peak amplitude of 10 mm at a 4.5 Hz frequency. We used a manual external drive to simulate the vertical oscillations that a 100-kilogram ostrich produces when its hip oscillates vertically from peak to peak about 100 mm during running at a frequency of 3.0 Hz (N. Smith et al., 2010). Pros of the manual entrainment: increased amplitude of external acceleration, cons we lost fine control of the applied force and

Table 5.4: Simulation results of different LSO model configurations. The simulation aimed to evaluate the dependence of the response of LSO models to external vertical acceleration. The table shows the dependence of a settling time, a peak-to-peak amplitude, a phase shift between the drive signal and model oscillation, an asymmetry of oscillation amplitude, a damped oscillation frequency, and a decay rate on controlled drive frequencies at 3.0, 3.5, 4.0, and 4.5 Hz. Values are mean values ± standard error (SE). SE is not shown if smaller than the rounding digit. Table is by An Mo

Model	Freq. [Hz]	Settling t τ [s]	Amp. A [mm]	Phase shift ϕ [deg]	Asymmetry β [/]	Damped freq. F_d [Hz]	Decay rate ζ [/]
0	3.0	0.43	0.85	10 ± 1	1.03 ± 0.01	12.9 ± 0.1	0.69 ± 0.02
	3.5	0.39 ± 0.02	1.21	3 ± 1	1.10 ± 0.01	13.0	0.89 ± 0.01
	4.0	0.43	1.72	4 ± 1	1.21	12.9	0.90 ± 0.01
	4.5	0.28	2.41	6 ± 1	1.35	12.8	0.94
1	3.0	0.55 ± 0.07	0.11	25 ± 1	1.02 ± 0.03	4.8	0.77 ± 0.03
	3.5	0.39	0.25	28 ± 1	0.99 ± 0.04	4.8	0.69 ± 0.02
	4.0	0.37 ± 0.02	0.62	49 ± 1	1.00 ± 0.02	4.7	0.79
	4.5	0.67	1.06	106 ± 1	1.08	4.7	0.83
2	3.0	0.63 ± 0.05	0.13	20 ± 1	0.68 ± 0.03	4.8	0.52 ± 0.02
	3.5	0.38	0.28	25 ± 1	0.97 ± 0.03	4.8	0.59 ± 0.01
	4.0	0.36	0.66	40 ± 1	1.01 ± 0.01	4.7	0.67 ± 0.01
	4.5	0.78 ± 0.01	1.33	92 ± 1	1.06	4.7	0.73
3	3.0	0.47 ± 0.04	0.19	21 ± 1	0.83 ± 0.01	4.5	0.58 ± 0.02
	3.5	0.39	0.44	24 ± 1	0.89 ± 0.01	4.4	0.66 ± 0.01
	4.0	0.61	1.03	62 ± 1	0.98	4.4	0.72
	4.5	0.56	1.32	120 ± 1	1.02 ± 0.02	4.4	0.74 ± 0.01
4	3.0	0.48	0.25	46 ± 1	1.11 ± 0.06	3.7	0.82 ± 0.02
	3.5	0.72 ± 0.02	0.57	80 ± 1	1.09 ± 0.05	3.6	0.87 ± 0.01
	4.0	0.52	0.66	130 ± 1	1.02 ± 0.03	3.6	0.87 ± 0.01
	4.5	0.36	0.56	154 ± 1	0.99 ± 0.02	3.6	0.87 ± 0.01
5	3.0	0.78 ± 0.16	0.06	152 ± 1	1.58 ± 0.56	4.3 ± 0.3	1.28 ± 0.15
	3.5	0.45	0.11	123 ± 1	1.03 ± 0.29	4.5 ± 0.1	1.53 ± 0.16
	4.0	0.40	0.19	127 ± 1	0.90 ± 0.03	4.3 ± 0.2	1.50 ± 0.09
	4.5	0.42 ± 0.02	0.28	147 ± 1	0.89 ± 0.04	4.4 ± 0.1	1.42 ± 0.14
6	3.0	0.48	0.25	56 ± 1	1.06 ± 0.02	3.5	0.88 ± 0.01
	3.5	0.70 ± 0.02	0.5	103 ± 1	0.86 ± 0.01	3.5	0.92 ± 0.01
	4.0	0.40	0.5	138 ± 1	0.87 ± 0.02	3.5	0.93 ± 0.02
	4.5	0.37	0.48	155 ± 1	0.86	3.5	0.89 ± 0.02
7	3.0	0.88 ± 0.22	0.07	152 ± 1	0.78 ± 0.21	4.4 ± 0.2	0.88 ± 0.11
	3.5	0.48 ± 0.04	0.12	127 ± 1	0.36 ± 0.02	5.0 ± 0.2	1.24 ± 0.18
	4.0	0.42 ± 0.02	0.19	137 ± 1	0.60 ± 0.02	4.6 ± 0.2	1.25 ± 0.21
	4.5	0.37	0.26	154 ± 1	0.79 ± 0.01	4.5 ± 0.2	1.02 ± 0.13
8	3.0	0.47	0.18	46 ± 1	0.85 ± 0.02	3.7	0.82 ± 0.02
	3.5	0.72 ± 0.02	0.47	76 ± 1	0.90 ± 0.02	3.7	0.82 ± 0.01
	4.0	0.52	0.58	129 ± 1	0.92 ± 0.03	3.7	0.84 ± 0.02
	4.5	0.36	0.51	150 ± 1	0.85 ± 0.01	3.7	0.79 ± 0.02
9	4.5		0.16				
	man.		2.13				
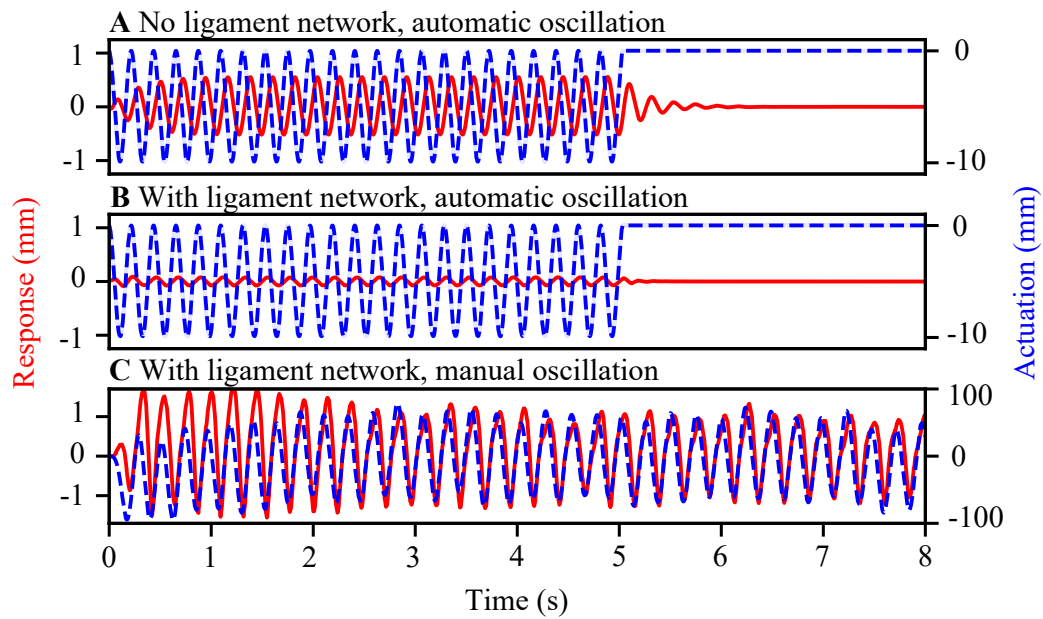
Figure 5.14: Effect of denticulate ligament network on soft tissue mobility.
Evaluation of the denticulate ligament influence by comparison model (2) without
a complete simplified ligaments network to model (9) actuated using automatic and
manual locomotion simulator movement. (A) model (2) without denticulate ligament
network actuated by automatic locomotion simulator. (B) model (9) with denticulate
ligaments network actuated by automatic locomotion simulator. (C) model (9) with
denticulate ligament network actuated by manual locomotion simulator. Plots are
models' oscillation response [mm] (solid red line) to applied external oscillations
representing an actuation signal in [mm] (dashed blue line, y-axis, right side). The
plot is by An Mo.

reproducibility of the experiment. The manual locomotion simulator can be
considered a trade-off between oscillation amplitude and oscillation control.

5.3 Conclusions

The configurable modular design of the LSO biophysical model allowed us to study the individual impact of each tested anatomical feature on the entrained system. The LSO biophysical model, incorporating key morphological and biophysical properties relevant to potential mechanosensitive function, confirmed that lumbosacral soft tissues respond to vertical external oscillations similar to a fluid-filled mass-spring-damper system. We confirmed that CSF filling a narrow space in the spinal canal protects the soft tissues from potential damage during oscillations by limiting their amplitude at a steady-state phase. Our hypothesis that the LSO resembles a spring-damper system is confirmed by the glycogen body acting as the spinal cord oscillation amplifier, whereas the denticulate ligaments suppress the amplitude. An absence of a linear relationship between the soft tissue response and the oscillation frequency value indicates that the CSF dynamics potentially affect the micro-fluid environment of the lumbosacral canal. Additional dorsal transverse grooves and ventral longitudinal dip inside the lumbosacral canal at the glycogen body location also affect fluid flow dynamics by acting as flow relievers that reduce CSF resistance. The results suggest that variations in the morphology of grooves and depressions under CSF dynamics may fine-tune the soft tissue sensitivity to external forces depending on the locomotion modalities. However, to confirm this assumption, we need to study fluid dynamics in the lumbosacral canal and establish a correlation between canal morphology and locomotion modalities. Symmetrical soft tissue oscillations under asymmetrical proximity to the dorsal and ventral sides of the spinal canal also confirm our assumption that the micro-fluid environment inside the lumbosacral canal affects the CSF dynamics.

Bibliography

Abourachid, A., R. Hackert, et al. (2011). "Bird terrestrial locomotion as revealed by 3D kinematics". In: *Zoology* 114.6, pp. 360–368.

Abourachid, A. and E. Höfling (2012). "The legs: a key to bird evolutionary success". In: *Journal of Ornithology* 153.1, pp. 193–198.

Abraira, V. E. and D. D. Ginty (2013). "The sensory neurons of touch". In: *Neuron* 79.4, pp. 618–639.

Agduhr, E. (1922). "Über ein zentrales Sinnesorgan (?) bei den Vertebraten". In: *Zeitschrift für Anatomie und Entwicklungsgeschichte* 66.3, pp. 223–360.

Alexander, R. Mc. N. et al. (1979). "Mechanics of running of the ostrich (Struthio camelus)". In: *Journal of Zoology* 187.2, pp. 169–178.

Angevine, P. D. et al. (2011). "Surgical management of ventral intradural spinal lesions". In: *Journal of Neurosurgery: Spine* 15.1, pp. 28–37.

Azcoitia, I., J. Fernandez-Soriano, and B. Fernandez-Ruiz (1985). "Is the avian glycogen body a secretory organ?" In: *Journal fur Hirnforschung* 26.6, pp. 651–657.

Badawi, H., A. Kenawy, and E. Hasouna (1994). "A comparative morphometric study on the cervical and lumbosacral enlargements in pigeon, duck and chicken". In: *Assiut Veterinary Medical Journal (Egypt)*.

Battal, B. et al. (2011). "Cerebrospinal fluid flow imaging by using phase-contrast MR technique". In: *The British journal of radiology* 84.1004, pp. 758–765.

Baumel, J. J. (1993). "Handbook of avian anatomy: nomina anatomica avium". In: *Publications of the Nuttall Ornithological Club (USA). no. 23.*

— (1985). "Suspensory ligaments of nerves: an adaptation for protection of the avian spinal cord". In: *Anatomia, histologia, embryologia* 14.1, pp. 1–5.

Bekoff, A., P. S. Stein, and V. Hamburger (Apr. 1975). "Coordinated motor output in the hindlimb of the 7-day chick embryo". In: *Proceedings of the National Academy of Sciences* 72.4, pp. 1245–1248.

Bentley, M. T. and T. J. Poole (2009). "Neurovascular anatomy of the embryonic quail hindlimb". In: *The Anatomical Record: Advances in Integrative Anatomy and Evolutionary Biology: Advances in Integrative Anatomy and Evolutionary Biology* 292.10, pp. 1559–1568.

Benzo, C. A., L. D. De Gennaro, and S. B. Stearns (1975). "Glycogen metabolism in the developing chick glycogen body: Functional significance of the direct oxidative pathway". In: *Journal of Experimental Zoology* 193.2, pp. 161–166.

Benzo, C.A. and L.D. De Gennaro (1981). "Glycogen metabolism in the developing accessory lobes of Lachi in the nerve cord of the chick: Metabolic correlations with the avian glycogen body". In: *Journal of Experimental Zoology* 215.1, pp. 47–52.

Benzo, C.A. and L.D. De Gennaro (1983). "An hypothesis of function for the avian glycogen body: A novel role for glycogen in the central nervous system". In: *Medical Hypotheses* 10.1, pp. 69–76.

Besl, P. J. and N. D. McKay (1992). "Method for registration of 3-D shapes". In: *Sensor fusion IV: control paradigms and data structures*. Vol. 1611. International Society for Optics and Photonics, pp. 586–606.

Biederman-Thorson, M. and J. Thorson (1973). "Rotation-compensating reflexes independent of the labyrinth and the eye". In: *Journal of comparative Physiology* 83.2, pp. 103–122.

Bloomfield, I. G., I. H. Johnston, and L. E. Bilston (1998). "Effects of proteins, blood cells and glucose on the viscosity of cerebrospinal fluid". In: *Pediatric neurosurgery* 28.5, pp. 246–251.

Böhm, U. L. et al. (2016). "CSF-contacting neurons regulate locomotion by relaying mechanical stimuli to spinal circuits". In: *Nature communications* 7.1, pp. 1–8.

Bruce, K. D., A. Zsombok, and R. H. Eckel (2017). "Lipid processing in the brain: a key regulator of systemic metabolism". In: *Frontiers in endocrinology* 8, p. 60.

Brusatte, S. L., J. K. O'Connor, and E. D. Jarvis (2015). "The origin and diversification of birds". In: *Current Biology* 25.19, R888–R898.

Buchanan, G., M. Minhua, and P. M. Rea (2014). "A multimedia package for patient understanding and rehabilitation of non-contact anterior cruciate ligament injuries". In: *International Journal of Medical Imaging* 2.3, pp. 44–53.

Bui, H.N. N. and H. CE. Larsson (2021). "Development and evolution of regionalization within the avian axial column". In: *Zoological Journal of the Linnean Society* 191.1, pp. 302–321.

Ceylan, D. et al. (2012). "The denticulate ligament: anatomical properties, functional and clinical significance". In: *Acta Neurochirurgica* 154.7, pp. 1229–1234.

Chan DMD, Flickr (2007). *Ostrich*.

Chen, H. H. et al. (2003). "Development of the monosynaptic stretch reflex circuit". In: *Current opinion in neurobiology* 13.1, pp. 96–102.

Chen, R. et al. (2015). "Anatomic study and clinical significance of the dorsal meningovertebral ligaments of the thoracic dura mater". In: *Spine* 40.10, pp. 692–698.

Christ, B., R. Huang, and J. Wilting (2000). "The development of the avian vertebral column". In: *Anatomy and embryology* 202.3, pp. 179–194.

Churan, J. et al. (2017). "Integration of visual and tactile information in reproduction of traveled distance". In: *Journal of neurophysiology* 118.3, pp. 1650–1663.

Clarke, E. C. (2011). "Spinal Cord Mechanical Properties". In: *Neural Tissue Biomechanics*. Ed. by Lynne E. Bilston. Berlin, Heidelberg: Springer Berlin Heidelberg, pp. 25–40.

Commons, Wikipedia (2009). *Squelette d'oiseau*.

Côté, M-P., L. M. Murray, and M. Knikou (2018). "Spinal control of locomotion: individual neurons, their circuits and functions". In: *Frontiers in physiology* 9, p. 784.

Coutureau, Michel (2014). *Ostrich skeleton*.

Dale, N. et al. (1987). "The morphology and distribution of 'Kolmer–Agduhr cells', a class of cerebrospinal-fluid-contacting neurons revealed in the frog embryo spinal cord by GABA immunocytochemistry". In: *Proceedings of the Royal Society of London. Series B. Biological Sciences* 232.1267. Publisher: Royal Society, pp. 193–203.

Daley, M. A. (2018). "Understanding the agility of running birds: sensorimotor and mechanical factors in avian bipedal locomotion". In: *Integrative and comparative biology* 58.5, pp. 884–893.

Daley, M. A., A. J. Channon, et al. (2016). "Preferred gait and walk–run transition speeds in ostriches measured using GPS-IMU sensors". In: *Journal of Experimental Biology* 219.20, pp. 3301–3308.

Daley, M. A., J. R. Usherwood, et al. (2006). "Running over rough terrain: guinea fowl maintain dynamic stability despite a large unexpected change in substrate height". In: *J Exp Biol* 209.1, pp. 171–187.

De Gennaro, L. D. (1993). "Origin of the avian glycogen body. II. Observations in support of a glial nature in the chick embryo." In: *Growth, Development, and Aging: GDA* 57.4, pp. 275–281.

De Gennaro, L. D. and C. A. Benzo (1976). "Ultrastructural characterization of the accessory lobes of Lachi (Hofmann's nuclei) in the nerve cord of the chick. I. Axoglial synapses". In: *Journal of Experimental Zoology* 198.1, pp. 97–107.

— (1978). "Ultrastructural characterization of the accessory lobes of Lachi (Hofmann's nuclei) in the nerve cord of the chick. II. Scanning and transmission electron microscopy with observations on the glycogen body". In: *Journal of Experimental Zoology* 206.2, pp. 229–239.

De Gennaro, L.D. (1961). "The carbohydrate composition of the glycogen body of the chick embryo as revealed by paper chromatography". In: *The Biological Bulletin* 120.3, pp. 348–352.

— (1982). "The glycogen body". In: *Avian biology* 6, pp. 341–371.

De Gennaro, L.D. and C.A. Benzo (1987). "Development of the glycogen body of the Japanese quail, Coturnix Japonica. I. Light microscopy of early development". In: *Journal of Morphology* 194.2, pp. 209–217.

Di Prisco, G. V., P. Walle, S. Grillner, et al. (1990a). "Synaptic effects of intraspinal stretch receptor neurons mediating movement-related feedback during locomotion". In: *Brain research* 530.1, pp. 161–166.

— (1990b). "Synaptic effects of intraspinal stretch receptor neurons mediating movement-related feedback during locomotion". In: *Brain research* 530.1, pp. 161–166.

Dial, K. P. (2003). "Evolution of avian locomotion: correlates of flight style, locomotor modules, nesting biology, body size, development, and the origin of flapping flight". In: *The Auk* 120.4, pp. 941–952.

Dobrev, I. et al. (2017). "Sound wave propagation on the human skull surface with bone conduction stimulation". In: *Hearing research* 355, pp. 1–13.

Dumont, E. R. (2010). "Bone density and the lightweight skeletons of birds". In: *Proceedings of the Royal Society B: Biological Sciences* 277.1691, pp. 2193–2198.

Dusenbery, D. B. (1992). *Sensory ecologyhow organisms acquire and respond to infromation.* Tech. rep.

Eide, A. L. (1996). "The axonal projections of the Hofmann nuclei in the spinal cord of the late stage chicken embryo". In: *Anatomy and Embryology* 193.6, pp. 543–557.

Eide, A. L. and J. C. Glover (1996). "Development of an Identified Spinal Commissural Interneuron Population in an Amniote: Neurons of the Avian Hofmann Nuclei". In: *The Journal of Neuroscience* 16.18, pp. 5749–5761.

Eklund, A. et al. (2007). "Assessment of cerebrospinal fluid outflow resistance". In: *Medical & biological engineering & computing* 45.8, pp. 719–735.

Eltoum, I. et al. (2001). "Introduction to the theory and practice of fixation of tissues". In: *Journal of Histotechnology* 24.3, pp. 173–190.

Emmert, A. G. F. (1811). "Beobachtungen über einige anatomische Eigenheiten der Vögel". In: *Reil's Arch. Physiol.* 10, pp. 377–392.

Farboodmanesh, S. et al. (2005). "Effect of coating thickness and penetration on shear behavior of coated fabrics". In: *Journal of Elastomers & Plastics* 37.3, pp. 197–227.

Feeney Jr, J. F. and R. L. Watterson (1946). "The development of the vascular pattern within the walls of the central nervous system of the chick embryo". In: *Journal of Morphology* 78.2, pp. 231–303.

Fernández, A., M. Radmilovich, and O. Trujillo-Cenóz (1998). "The marginal nuclei of the spinal cord in turtles: neuron assemblies in which γ-aminobutyric acid and nitric oxide synthase are colocalized". In: *Experimental brain research* 122.1, pp. 128–130.

Fink, A. S., P. M. Hefferan, and R. R. Howell (1975). "Enzymatic and biochemical characterization of the avian glycogen body". In: *Comparative Biochemistry and Physiology Part B: Comparative Biochemistry* 50.4, pp. 525–530.

Gage, S. H. (1917). "Glycogen in the nervous system of vertebrates". In: *Journal of Comparative Neurology* 27.3, pp. 451–465.

Gatesy, S. M. and K. P. Dial (1996). "Locomotor modules and the evolution of avian flight". In: *Evolution* 50.1, pp. 331–340.

Gatesy, S. M. and K. M. Middleton (1997). "Bipedalism, flight, and the evolution of theropod locomotor diversity". In: *Journal of Vertebrate Paleontology* 17.2, pp. 308–329.

Giffin, E. B. (1990). "Gross spinal anatomy and limb use in living and fossil reptiles". In: *Paleobiology*, pp. 448–458.

— (1995). "Functional interpretation of spinal anatomy in living and fossil amniotes". In: *Functional morphology in vertebrate paleontology*, pp. 235–248.

Gignac, P. M. and N. J. Kley (2014). "Iodine-enhanced micro-CT imaging: Methodological refinements for the study of the soft-tissue anatomy of post-embryonic vertebrates". In: *Journal of Experimental Zoology Part B: Molecular and Developmental Evolution* 322.3, pp. 166–176.

Gignac, P. M., N. J. Kley, et al. (2016). "Diffusible iodine-based contrast-enhanced computed tomography (diceCT): an emerging tool for rapid, high-resolution, 3-D imaging of metazoan soft tissues". In: *Journal of Anatomy* 228.6, pp. 889–909.

Giuffre, B. A. and R. Jeanmonod (2020). "Anatomy, sciatic nerve.[Updated 2020 Apr 23]". In: *StatPearls [Internet]. Treasure Island, FL: StatPearls Publishing.*

Goel, R. K. (2005). "Seismic response of linear and non-linear asymmetric systems with non-linear fluid viscous dampers". In: *Earthquake engineering & structural dynamics* 34.7, pp. 825–846.

Gomes, J. P. (2012). *Fluid-Structure Interaction-Induced Oscillation of Flexible Structures in Uniform Flows.* Friedrich-Alexander-Universitaet Erlangen-Nuernberg (Germany).

Gomes, J. P. and H. Lienhart (2013). "Fluid–structure interaction-induced oscillation of flexible structures in laminar and turbulent flows". In: *Journal of fluid mechanics* 715, pp. 537–572.

Grillner, S. (1986). "Interaction between sensory signals and the central networks controlling locomotion in lamprey, dogfish and cat". In: *Neurobiology of vertebrate locomotion*, pp. 505–512.

Grillner, S., A. McClellan, and C. Perret (1981). "Entrainment of the spinal pattern generators for swimming by mechano-sensitive elements in the lamprey spinal cord in vitro". In: *Brain Research* 217.2, pp. 380–386.

Grillner, S., A. McClellan, and K. Sigvardt (1982). "Mechanosensitive neurons in the spinal cord of the lamprey". In: *Brain research* 235.1, pp. 169–173.

Grillner, S., T. Williams, and P-A. Lagerback (1984). "The edge cell, a possible intraspinal mechanoreceptor". In: *Science* 223.4635, pp. 500–503.

Gurtovoy, N.N., B.S. Matveev, and F.Y. Dzershinsky (1992). *Practice in the Zootomy of Vertebrates. Birds, Mammals: Vysshaya Shkola.* Press Moscow.

Haimson, B. et al. (2021). "Spinal lumbar dI2 interneurons contribute to stability of bipedal stepping". In: *Elife* 10, e62001.

Harrison, D. E. et al. (1999). "A review of biomechanics of the central nervous system—Part III: spinal cord stresses from postural loads and their neurologic effects". In: *Journal of manipulative and physiological therapeutics* 22.6, pp. 399–410.

Hauptmann (Richter), J. (2018). "Untersuchung und Charakterisierung von Teilelementen der Modifikation im Lumbosacralbereich von Vögeln". Hochschule Harz.

Haziroglu, R. M. et al. (2001). "Morphology of the spinal cord in the chicken, duck and pigeon". In: *Turkish Journal of Veterinary and Animal Sciences* 25.6, pp. 913–920.

Heers, A. M. and K. P. Dial (2015). "Wings versus legs in the avian bauplan: development and evolution of alternative locomotor strategies". In: *Evolution* 69.2, pp. 305–320.

Henderson, K. W., E. Menelaou, and M. E. Hale (2019). "Sensory neurons in the spinal cord of zebrafish and their local connectivity". In: *Current Opinion in Physiology.* Motor Control Systems 8, pp. 136–140.

Henry, H. T., D. J. Ellerby, and R. L. Marsh (2005). "Performance of guinea fowl Numida meleagris during jumping requires storage and release of elastic energy". In: *Journal of Experimental Biology* 208.17, pp. 3293–3302.

Hepp, J. and A. Badri-Spröwitz (2021). "A Novel Spider-Inspired Rotary-Rolling Diaphragm Actuator with Linear Torque Characteristic and High Mechanical Efficiency". In: *Soft Robotics*.

Higuchi, H. et al. (2004). "Influence of lumbosacral cerebrospinal fluid density, velocity, and volume on extent and duration of plain bupivacaine spinal anesthesia". In: *Anesthesiology: The Journal of the American Society of Anesthesiologists* 100.1, pp. 106–114.

Hitchins, A. D., K. Jinneman, and Y. Chen (1998). "Bacteriological analytical manual". In: *Food and Drug Administration, Washington, DC*.

Hsu, LJ. et al. (2013). "Intraspinal stretch receptor neurons mediate different motor responses along the body in lamprey". In: *Journal of Comparative Neurology* 521.16, pp. 3847–3862.

Hubbard, J. M. et al. (2016). "Intraspinal Sensory Neurons Provide Powerful Inhibition to Motor Circuits Ensuring Postural Control during Locomotion". In: *Current Biology* 26.21, pp. 2841–2853.

Huber, J. F. (1936). "Nerve roots and nuclear groups in the spinal cord of the pigeon". In: *The Journal of Comparative Neurology* 65.1, pp. 43–91.

Hudspeth, A. J. (1989). "How the ear's works work". In: *Nature* 341.6241. Publisher: Nature Publishing Group, pp. 397–404.

Hutchinson, J. R. (2012). "On the inference of function from structure using biomechanical modelling and simulation of extinct organisms". In: *Biology letters* 8.1, pp. 115–118.

Imagawa, T., K. Shogaki, and M. Uehara (2006). "Interaction between glycogen body cell and neuron: examination in co-culture system". In: *Journal of veterinary medical science* 68.10, pp. 1081–1087.

Imhof, G. (1904). "Anatomie und Entwicklungsgeschichte des Lumbalmarkes bei den Vögeln". In: *Archiv für Mikroskopische Anatomie* 65.1, pp. 498–610.

Jadwiszczak, P. (2014). "Synsacra of the Eocene Antarctic penguins: new data on spinal maturation and an insight into their role in the control of walking". In: *Polish Polar Research*, pp. 27–39.

Jalalvand, E. et al. (2016). "Ciliated neurons lining the central canal sense both fluid movement and pH through ASIC3". In: *Nature communications* 7.1, pp. 1–12.

Jeffery, G. H., J. Bassett, and et al. Mendham J. (1989). *Vogel's textbook of quantitative chemical analysis*. New York: Wiley Sons, Inc.

Jerry Ting, Flickr (2013). *Running quail*.

Johanson, C. E. et al. (2008). "Multiplicity of cerebrospinal fluid functions: new challenges in health and disease". In: *Cerebrospinal fluid research* 5.1, pp. 1–32.

Jonmarker, S. et al. (2006). "Tissue shrinkage after fixation with formalin injection of prostatectomy specimens". In: *Virchows Archiv* 449.3, pp. 297–301.

Kaczmarek, M., J. Kubik, and M. Pakula (2002). "Short ultrasonic waves in cancellous bone". In: *Ultrasonics* 40.1-8, pp. 95–100.

Kamska, V., F. B. Contreras, et al. (2021). "Associating functional morphology of the lumbosacral organ and locomotion modalities in avians". In.

Kamska, V., M. A. Daley, and A. Badri-Spröwitz (2020). "3D anatomy of the quail lumbosacral spinal canal—implications for putative mechanosensory function". In: *Integrative Organismal Biology*.

Kaneko, J. J., J. W. Harvey, and M. L. Bruss (2008). *Clinical biochemistry of domestic animals*. Academic press.

Kardon, G. (1998). "Muscle and tendon morphogenesis in the avian hind limb". In: *Development* 125.20, pp. 4019–4032.

Kim, H-J. et al. (2021). "Cerebrospinal fluid dynamics correlate with neurogenic claudication in lumbar spinal stenosis". In: *PloS one* 16.5, e0250742.

Koizumi, J. (1974). "Glycogen in the central nervous system". In: *Progress in histochemistry and cytochemistry* 6.4, pp. III–35.

Kölliker, A. (1902). *Über die oberflächlichen Nervenkerne im Marke der Vögel und Reptilien*. W. Engelmann.

Kolmer, W. (1921). "Das „Sagittalorgan "der Wirbeltiere". In: *Zeitschrift für Anatomie und Entwicklungsgeschichte* 60.3, pp. 652–717.

Lachi, P. (1889). "Alcune particolarita anatomiche del rigonfiamento sacrale nel midollo degli uccelli". In: *Lobi accessori. Att Soc Tosc Sci Nat.* 10, pp. 268–295.

Lance-Jones, C. and L. Landmesser (1981). "Pathway selection by chick lumbosacral motoneurons during normal development". In: *Proceedings of the Royal Society of London. Series B. Biological Sciences* 214.1194, pp. 1–18.

Lee, K. et al. (2001). "Effects of adrenergic agonists on glycogenolysis in primary cultures of glycogen body cells and telencephalon astrocytes of the chick". In: *Poultry science* 80.12, pp. 1736–1742.

Loth, F., M. A. Yardimci, and N. Alperin (2001). "Hydrodynamic modeling of cerebrospinal fluid motion within the spinal cavity". In: *Journal of biomechanical engineering* 123.1, pp. 71–79.

Lui, A. CP., T. Z. Polis, and N. J. Cicutti (1998). "Densities of cerebrospinal fluid and spinal anaesthetic solutions in surgical patients at body temperature". In: *Canadian Journal of Anaesthesia* 45.4, p. 297.

Lyser, K. M. (1973). "The fine structure of the glycogen body of the chicken". In: *Cells Tissues Organs* 85.4, pp. 533–549.

Martin, G. R. (2012). "Through birds' eyes: insights into avian sensory ecology". In: *Journal of Ornithology* 153.1, pp. 23–48.

McClellan, A. D. and K. A. Sigvardt (1988). "Features of entrainment of spinal pattern generators for locomotor activity in the lamprey spinal cord". In: *Journal of Neuroscience* 8.1, pp. 133–145.

McCormick, P. C. and B. M. Stein (1990). "Functional anatomy of the spinal cord and related structures". In: *Neurosurgery Clinics of North America* 1.3, pp. 469–489.

Mellado, J. M. et al. (2011). "MDCT of variations and anomalies of the neural arch and its processes: part 1—pedicles, pars interarticularis, laminae, and spinous process". In: *American Journal of Roentgenology* 197.1, W104–W113.

Metscher, B. D. (2009a). "MicroCT for comparative morphology: simple staining methods allow high-contrast 3D imaging of diverse non-mineralized animal tissues". In: *BMC physiology* 9.1, p. 11.

— (2009b). "MicroCT for developmental biology: A versatile tool for high-contrast 3D imaging at histological resolutions". In: *Developmental dynamics: an official publication of the American Association of Anatomists* 238.3, pp. 632–640.

Milinski, T. and R. Necker (2001). "Histochemical and immunocytochemical investigations of the marginal nuclei in the spinal cord of pigeons (Columba livia)". In: *Brain research bulletin* 56.1, pp. 15–21.

Molnar, J. L. et al. (2012). "Idealized landmark-based geometric reconstructions of poorly preserved fossil material: A case study of an early tetrapod vertebra". In: *Palaeontologia Electronica* 15.1, p. 1.

More, H. L. and J. M. Donelan (2018). "Scaling of sensorimotor delays in terrestrial mammals". In: *Proceedings of the Royal Society B* 285.1885, p. 20180613.

More, H. L., J. R. Hutchinson, et al. (2010). "Scaling of sensorimotor control in terrestrial mammals". In: *Proceedings of the Royal Society B: Biological Sciences* 277.1700, pp. 3563–3568.

More, H. L., S. M. O'Connor, et al. (2013). "Sensorimotor responsiveness and resolution in the giraffe". In: *Journal of Experimental Biology* 216.6, pp. 1003–1011.

Müller-Schweinitzer, E. (2009). "Cryopreservation of vascular tissues". In: *Organogenesis* 5.3, pp. 97–104.

Necker, R. (1997). "Projections of the marginal nuclei in the spinal cord of the pigeon". In: *Journal of Comparative Neurology* 377.1, pp. 95–104.

— (1999). "Specializations in the Lumbosacral Spinal Cord of Birds: Morphological and Behavioural Evidence for a Sense of Equilibrium". In: *European Journal of Morphology* 37.2-3, pp. 211–214.

— (2005). "The structure and development of avian lumbosacral specializations of the vertebral canal and the spinal cord with special reference to a possible function as a sense organ of equilibrium". In: *Anatomy and Embryology* 210.1, pp. 59–74.

— (2006). "Specializations in the lumbosacral vertebral canal and spinal cord of birds: evidence of a function as a sense organ which is involved in the control of walking". In: *Journal of Comparative Physiology A* 192.5, p. 439.

Necker, R., A. Janßen, and T. Beissenhirtz (Apr. 2000). "Behavioral evidence of the role of lumbosacral anatomical specializations in pigeons in maintaining balance during terrestrial locomotion". In: *Journal of Comparative Physiology A* 186.4, pp. 409–412.

Nicolai, T. G. I. (1812). "Über das Rückenmark der Vögel und die Bildung desselben im bebrüteten Ei". In: *Arch. Physiologie* 11, pp. 156–219.

Noguchi, M. et al. (2000). "Assessment of morphometric measurements of prostate carcinoma volume". In: *Cancer: Interdisciplinary International Journal of the American Cancer Society* 89.5, pp. 1056–1064.

Nowacek, J. M. and J. A. Kiernan (2010). "Fixation and tissue processing". In: *Pathology Education Guide: Special Stains and H & E, 2nd edn. Dako, California, North America*, pp. 141–152.

Obrist, D. (2011). "Fluid mechanics of the inner ear". In.

Obrist, D. et al. (2010). "In vitro model of a semicircular canal: design and validation of the model and its use for the study of canalithiasis". In: *Journal of Biomechanics* 43.6, pp. 1208–1214.

Ollé, R. D. (2006). *The glycogen body in neonate birds of the order psittaciformes and its role in neonate mortality*. VVB Laufersweiler.

Orosz, S. E. and G. A. Bradshaw (2007). "Avian neuroanatomy revisited: from clinical principles to avian cognition". In: *Veterinary clinics of North America: Exotic animal practice* 10.3, pp. 775–802.

Orts-Del'Immagine, A. et al. (2020). "Sensory neurons contacting the cerebrospinal fluid require the reissner fiber to detect spinal curvature in vivo". In: *Current Biology* 30.5, pp. 827–839.

Otani, T. (2005). "Quantitative estimation of bone density and bone quality using acoustic parameters of cancellous bone for fast and slow waves". In: *Japanese journal of applied physics* 44.6S, p. 4578.

Otani, T. and A. Hosokawa (1998). "Effects of the structural anisotropy and the porosi˜ on ultrasonic wave propagation bovine cancellous bone". In: *The Journal of the Acoustical Society of America* 9, pp. 2505–2506.

Picton, L. D. et al. (2021). "A spinal organ of proprioception for integrated motor action feedback". In: *Neuron* 109.7, pp. 1188–1201.

Polak, K. et al. (2014). "Biomechanical characteristics of the porcine denticulate ligament in different vertebral levels of the cervical spine—Preliminary results of an experimental study". In: *journal of the mechanical behavior of biomedical materials* 34, pp. 165–170.

Polak-Kraśna, K. et al. (2019). "The denticulate ligament–Tensile characterisation and finite element micro-scale model of the structure stabilising spinal cord". In: *Journal of the mechanical behavior of biomedical materials* 91, pp. 10–17.

Python.org (n.d.). *Welcome to Python.org.*

Ramo, N. L., K. L. Troyer, and C. M. Puttlitz (2018). "Viscoelasticity of spinal cord and meningeal tissues". In: *Acta biomaterialia* 75, pp. 253–262.

Ranger, M. R. B. et al. (2008). "Changing body position alters the location of the spinal cord within the vertebral canal: a magnetic resonance imaging study". In: *British journal of anaesthesia* 101.6, pp. 804–809.

Reese, E. P. and T. W. Reese (1962). "The quail, Coturnix coturnix, as a laboratory animal". In: *Journal of the Experimental Analysis of Behavior* 5.2, pp. 265–270.

Rosenberg, J. and R. Necker (2002). "Ultrastructural characterization of the accessory lobes of Lachi in the lumbosacral spinal cord of the pigeon with special reference to intrinsic mechanoreceptors". In: *Journal of Comparative Neurology* 447.3, pp. 274–285.

Rossitti, S. (1993). "Biomechanics of the pons-cord tract and its enveloping structures: an overview". In: *Acta neurochirurgica* 124.2, pp. 144–152.

Rovainen, C. M. (1979). "Neurobiology of lampreys". In: *Physiological reviews* 59.4, pp. 1007–1077.

Rumble, J. R. (2021). *CRC Handbook of Chemistry and Physics*. Vol. 102. CRC Press/Taylor & Francis.

Ruthensteiner, B. and M. Heß (2008). "Embedding 3D models of biological specimens in PDF publications". In: *Microscopy research and technique* 71.11, pp. 778–786.

Sansone, F. M. (1980). "An ultrastructural study of the craniocaudal continuation of the glycogen body". In: *Journal of Morphology* 163.1, pp. 45–58.

Schroeder, D. M. (1986a). "An ultrastructural study of the marginal nucleus, the intrinsic mechanoreceptor of the snake's spinal cord". In: *Somatosensory research* 4.2, pp. 127–140.

— (1986b). "The marginal nuclei in the spinal cord of reptiles: intraspinal mechanoreceptors". In.

Schroeder, D. M. and M. W. Egar (1990). "Marginal neurons in the urodele spinal cord and the associated denticulate ligaments". In: *Journal of comparative neurology* 301.1, pp. 93–103.

Schroeder, D. M. and R.G. Murray (1987). "Specializations within the lumbosacral spinal cord of the pigeon". In: *Journal of Morphology* 194.1, pp. 41–53.

Schroeder, D. M. and S. C. Richardson (1985a). "Is the intimate relationship between ligaments and marginal specialized cells in the snake's spinal cord indicative of a CNS mechanoreceptor?" In: *Brain research* 328.1, pp. 145–149.

— (1985b). "Is the intimate relationship between ligaments and marginal specialized cells in the snake's spinal cord indicative of a CNS mechanoreceptor?" In: *Brain Research* 328.1, pp. 145–149.

Scott, R. B. and W. J. S. Still (1970). "Properties of liver glycogen isolated in density gradients of sodium lothalamate". In: *Archives of Biochemistry and Biophysics* 139.1, pp. 87–92.

Selva, P., J. Morlier, and Y. Gourinat (2009). "Development of a dynamic virtual reality model of the inner ear sensory system as a learning and demonstrating tool". In: *Modelling and simulation in engineering* 2009.

Shi, B. et al. (2014). "The morphology and clinical significance of the dorsal meningovertebra ligaments in the cervical epidural space". In: *The Spine Journal* 14.11, pp. 2733–2739.

Siegal, T. et al. (1988). "Indomethacin and dexamethasone treatment in experimental neoplastic spinal cord compression: Part 1: Effect on water content and specific gravity". In: *Neurosurgery* 22.2, pp. 328–333.

Sillevis, R. and R. Hogg (2020). "Anatomy and clinical relevance of sub occipital soft tissue connections with the dura mater in the upper cervical spine". In: *PeerJ* 8, e9716.

Simon, M. J. and J. J. Iliff (2016). "Regulation of cerebrospinal fluid (CSF) flow in neurodegenerative, neurovascular and neuroinflammatory disease". In: *Biochimica et Biophysica Acta (BBA)-Molecular Basis of Disease* 1862.3, pp. 442–451.

Smith, H. and S. R. Geiger (1961). "Another hypothesis of function of the glycogen body of birds". In: *Journal of the Elisha Mitchell Scientific Society* 77.2, pp. 289–293.

Smith, N., K. J. Jespers, and A. M. Wilson (2010). "Ontogenetic scaling of locomotor kinetics and kinematics of the ostrich (Struthio camelus)". In: *Journal of Experimental Biology* 213.8, pp. 1347–1355.

Software, Tracker (n.d.). *Tracker Video Analysis and Modeling Tool for Physics Education.*

Stanchak, K. E., C.r French, et al. (2020). "The balance hypothesis for the avian lumbosacral organ and an exploration of its morphological variation". In: *bioRxiv.*

Stanchak, K. E., K. E. Miller, et al. (2022). "Molecular markers of mechanosensation in glycinergic neurons in the avian lumbosacral spinal cord". In: *bioRxiv.*

Sternberg, J. R. et al. (2018). "Pkd2l1 is required for mechanoception in cerebrospinal fluid-contacting neurons and maintenance of spine curvature". In: *Nature communications* 9.1, pp. 1–10.

Stetson, D. S. et al. (1992). "Effects of age, sex, and anthropometric factors on nerve conduction measures". In: *Muscle & Nerve: Official Journal of the American Association of Electrodiagnostic Medicine* 15.10, pp. 1095–1104.

Stewart, S. et al. (2020). "Mechanotransduction in osteogenesis". In: *Bone & Joint Research* 9.1, pp. 1–14.

Streeter, G. L. (1904). "The structure of the spinal cord of the ostrich". In: *American Journal of Anatomy* 3.1, pp. 1–27.

Suazo, I. et al. (2022). "The Lamellar Cells of Vertebrate Meissner and Pacinian Corpuscles: Development, Characterization, and Functions". In: *Frontiers in Neuroscience* 16.

Szepsenwol, J. and J. V. Michalski (1951). "Glycogenolysis in the liver and glycogen body of the chicken after death". In: *American Journal of Physiology-Legacy Content* 165.3, pp. 624–627.

Terni, T. (1924). *Ricerche sulla cosidetta sostanza gelatinosa (corpo glicogenico) del midollo lombo-sacrale degli uccelli...* L. Niccolai.

Thompson, A. et al. (2021). "Efficient empirical determination of maximum permissible error in coordinate metrology". In: *Measurement Science and Technology.*

Thompson, T. L. and R. Amedee (2009). "Vertigo: a review of common peripheral and central vestibular disorders". In: *Ochsner Journal* 9.1, pp. 20–26.

Tunturi, A. R. (1978). "Elasticity of the spinal cord, pia, and denticulate ligament in the dog". In: *Journal of neurosurgery* 48.6, pp. 975–979.

Uehara, M. and T. Ueshima (1982). "Development of the glycogen body through the whole length of the chick spinal cord". In: *The Anatomical Record* 202.4, pp. 511–519.

— (1984). "Distribution of glycogen in the floor plate of the chick spinal cord during development". In: *The Anatomical Record* 209.1, pp. 105–113.

Urbina-Meléndez, D. et al. (2018). "A physical model suggests that hip-localized balance sense in birds improves state estimation in perching: implications for bipedal robots". In: *Frontiers in Robotics and AI* 5, p. 38.

Vickerton, P., J. Jarvis, and N. Jeffery (2013). "Concentration-dependent specimen shrinkage in iodine-enhanced micro CT". In: *Journal of anatomy* 223.2, pp. 185–193.

Vuković, S. and H. Lucić (2005). "Development of the glycogen body in turkey (Meleagris gallopavo) embryo." In: *Veterinarski arhiv* 75.2, pp. 101–110.

Vuković, S., H. Lucić, and S. Ćurković (1999). "Development of accessory lobes in the spinal cord of the turkey (Meleagris gallopavo)." In: *Veterinarski arhiv* 69.3, pp. 167–177.

Watterson, R. L. (1949). "Development of the glycogen body of the chick spinal cord. I. Normal morphogenesis, vasculogenesis and anatomical relationships". In: *Journal of morphology* 85.2, pp. 337–389.

— (1954). "Development of the glycogen body of the chick spinal cord. IV. Effects of mechanical manipulation of the roof plate at the lumbosacral level". In: *Journal of Experimental Zoology* 125.2, pp. 285–330.

Wedel, M. J. (2011). "A monument of inefficiency: The presumed course of the recurrent laryngeal nerve in sauropod dinosaurs". In: *Acta Palaeontologica Polonica* 57.2, pp. 251–256.

Whalen, L. R. et al. (1988). "Functional and structural alterations of the nervous system induced by avian retrovirus RAV-7". In: *Microbial pathogenesis* 4.6, pp. 401–416.

Whitesides, G. M. (2018). "Soft robotics". In: *Angewandte Chemie International Edition* 57.16, pp. 4258–4273.

Wyart, C. et al. (2009). "Optogenetic dissection of a behavioural module in the vertebrate spinal cord". In: *Nature* 461.7262, pp. 407–410.

Yamanaka, Y., N. Kitamura, and I. Shibuya (2008). "Chick spinal accessory lobes contain functional neurons expressing voltagegated sodium channels generating action potentials". In: *Biomedical Research* 29.4, pp. 205–211.

Yamanaka, Y., N. Kitamura, H. Shinohara, et al. (2012). "Analysis of GABA-induced inhibition of spontaneous firing in chick accessory lobe neurons". In: *Journal of Comparative Physiology A* 198.3, pp. 229–237.

— (2013). "Glutamate evokes firing through activation of kainate receptors in chick accessory lobe neurons". In: *Journal of Comparative Physiology A* 199.1, pp. 35–43.

Zeffer, A., L. C. Johansson, and Å. Marmebro (2003). "Functional correlation between habitat use and leg morphology in birds (Aves)". In: *Biological Journal of the Linnean Society* 79.3, pp. 461–484.

Zhang, A. et al. (2005). "Thermal stress study of two different artery cryopreservation methods". In: *CryoLetters* 26.2, pp. 113–120.

Zimmerman, A., L. Bai, and D. D. Ginty (2014). "The gentle touch receptors of mammalian skin". In: *Science* 346.6212, pp. 950–954.